Optical and Vibrational Properties of Doped Carbon Nanomaterials

Dissertation

zur Erlangung des Grades eines

Doktors der Naturwissenschaften

am Fachbereich Physik

der Freien Universität Berlin

vorgelegt von

Benjamin Hatting

Berlin, August 2016

1. Gutachterin: Prof. Dr. Stephanie Reich
2. Gutachter: Prof. Dr. Joachim Heberle

Tag der Einreichung: 25. August 2016
Tag der Disputation: 09. November 2016

Zusammenfassung

Graphen und Kohlenstoffnanoröhren sind zwei Kohlenstoffalloptrope, in denen die Atome in einem hexagonalen Honigwabengitter mit sp^2-hybridisierten Bindungen angeordnet sind, in einer Ebene in Graphen und aufgerollt in eine Röhre in Kohlenstoffnanoröhren. Während Graphen ein einzelnes zweidimensionales Material ist, sind Kohlenstoffnanoröhren eine Klasse von eindimensionalen Materialien, die metallisch oder halbleitend sein können. Um sp^2 Kohlenstoffmaterialien aufzuladen, werden elektrostatische Dotierung[1], elektrochemische Dotierung[2–4] und Alkalimetallaufdampfung[5–7] häufig verwendet. Elektrochemische Dotierung funktioniert durch die Bildung einer Debye Schicht an der Grenzfläche zwischen dem Probenmaterial und einem Elektrolyt. Dabei können viel größere Dotierungslevel erreicht werden als bei der elektrostatischen Dotierung. Alkalimetallaufdampfung erreicht mit elektrochemischer Dotierung vergleichbare Dotierungslevel und wird für die Herstellung von Graphitinterkalationsverbindungen verwendet.

In dieser Arbeit benutze ich Alkalimetallaufdampfung, um hochdotiertes Graphen zu produzieren, das ich dann mit Reflektivität- und Ramanspektroskopie untersuche. Um die Stärke der Dotierung zu bestimmen, messe ich die optische Reflektivität und vergleiche diese mit einem Modell, das ich auf Basis von Änderungen im Brechungsindex aufgrund der Dotierung entwickelt haben. Diese Messungen erlauben es, die Fermienergie in mit Kalium dotierten Graphen zu bestimmen. Ich erhalte einen Wert von 1.3 eV.

Ich präsentiere Ramanspektroskopiemessungen von mit Kalium dotierten Graphen als Funktion der Aufdampfungszeit und beobachte einen breiten und asymmetrischen Peak bei niedrigerer Frequenz als die G Mode in dotiertem Graphen. Ich untersuche diesen Peak mit Hilfe einer Vielzahl von Laserwellenlängen vom ultravioletten bis zum infraroten Spektralbereich und zeige, dass die Peakposition mit steigender Laserenergie monoton ansteigt. Für die Peakbreite und die Asymmetrie beobachte ich Maxima bei einer Laserenergie, die der doppelten Fermienergie entspricht. Ich charakterisiere das Ramansignal von mit Kalium dotierten Graphen außerdem unter Verwendung von linear und zirkular polarisiertem Licht. Hierbei stellt sich heraus, dass der neue asymmetrische Peak A_{1g} und E_{2g} Symmetrie vereint. Auf der Basis dieser Ergebnisse ziehe ich die Schlussfolgerung, dass der asymmetrische Peak in mit Kalium dotierten Graphen nicht eine Weiterführung der G Mode bei sehr hohen Ladungsträgerkonzentrationen darstellt.

Des Weiteren untersuche ich Kohlenstoffnanoröhren mittels elektrochemischer Dotierung in Kombination mit Ramanspektroskopie. Diese Studie wurde durch die Beobachtung von Unterschieden in den Ramanspektren von Nanoröhren in Lösung und abgelegt auf Substraten motiviert. Der Ramanpeak des longitudinalen optischen Phonons in metallischen Nanoröhren ist zu höheren Frequenzen verschoben und zeigt eine schmalere Linienbreite, wenn die Röhren auf einem Substrat abgelegt werden. Ich erkläre diese Beobachtung durch Verschiebungen der Fermienergie.

Ich führe außerdem elektrochemische Ramanmessungen an Energietransferkomplexen durch, die aus Kohlenstoffnanoröhren und einem Farbstoffmolekül mit einer höheren Absorptionsstärke bestehen. Die Energietransferkomplexe haben eine niedrigere Dotierungseffizienz und eine verschobene Spannung des Ladungsneutralitätspunkts. Ich bestimme die Fermienergie der Komplexe in Lösung und ziehe die Schlussfolgerung, dass Ladungstransfer zwischen dem Farbstoff und den Nanoröhren allein nicht die Verringerung der Photolumineszensintensität erklären kann, die in früheren Arbeiten an diesen Komplexen beobachtet wurde.

Abstract

Graphene and single-walled carbon nanotubes are two carbon allotropes featuring a hexagonal lattice with sp^2-hybridized bonds, either in a plane in the case of graphene or rolled up into a tube in single-walled nanotubes. While graphene is a single two-dimensional material, single-walled carbon nanotubes are a set of one-dimensional materials that can be metallic or semiconducting.

Electrostatic gating[1], electrochemical gating[2–4], and exposure to potassium[5,6] and rubidium[7] vapor are commonly used techniques to charge sp^2 carbon materials. Electrochemical gating works through the formation of an electric Debye layer at the interface of the sample material and an electrolyte and yields doping levels far exceeding those in electrostatic gating. Exposure to alkali metal vapor can achieve doping levels comparable to electrochemical gating and has been widely used for the production of graphite intercalation compounds. Superconductivity has been demonstrated with a transition temperature of 11.5 K in CaC_6[8] (one calcium atom per six carbon atoms). Theoretical studies have predicted LiC_6 monolayer graphene to exhibit phonon mediated superconductivity with a critical temperature of 8.1 K[9], while the critical temperature for bulk LiC_6 is only 0.9 K.

In this thesis, firstly, I use exposure to alkali metal vapor to produce highly doped monolayer graphene. To investigate the doping strength obtained using this method, I measure the optical reflectivity and compare it to a model I develop based on changes in the refractive index of graphene upon doping. These measurements allow me to determine the Fermi energy in potassium-doped graphene to be 1.3 eV.

I conduct a Raman spectroscopy study of potassium doping of graphene as a function of doping time, and observe the appearance of a broad and asymmetric peak at a peak position much lower than that of the doped G line. I investigate this peak over a broad range of laser excitation energies and find that the peak position increases monotonously as a function of laser energy. I also characterize the polarization behavior of the Raman signal of potassium-doped graphene in linear and circular polarizations. Here I find that the new asymmetric peak shows A_{1g} and E_{2g} symmetry. I therefore conclude that the asymmetric peak observed in potassium-doped graphene is not the result of a continuation of the behavior of the G mode at very high doping strengths.

Secondly, I study single-walled carbon nanotubes using electrochemical gating in combination with *in-situ* Raman spectroscopy, a study that was initially motivated by the observation of differences in the Raman spectrum of nanotubes in solution and nanotubes deposited onto substrates. The longitudinal optical phonon Raman peak of metallic nanotubes upshifts and the line width narrows when the nanotubes are deposited onto a substrate. I explain these observations as being caused by shifts in the Fermi energy that affect the Kohn anomaly in the longitudinal optical phonon branch in metallic nanotubes. I then use *in-situ* electrochemical Raman measurements to show that I can reproduce the spectra in solution by deliberately shifting the Fermi energy.

I furthermore conduct an electrochemical Raman spectroscopy study of carbon nanotube energy transfer complexes. In these energy transfer complexes, a dye molecule featuring a high absorption strength is brought close to the nanotube. The energy transfer complexes exhibit a lower gating efficiency and a shifted voltage position of the charge neutrality point. I quantify the Fermi energy of complexes in solution and conclude that charge transfer between the dye and the nanotubes cannot explain the photoluminescence quenching observed in previous works for some of these complexes.

Contents

1 | Introduction

Graphene and single-walled carbon nanotubes are two allotropes of carbon in which the atoms are arranged in a honeycomb lattice featuring sp^2-hybridized bonds, either in a plane in the case of graphene or rolled up into a tube in single-walled nanotubes.

Graphene was first isolated in 2004[10] and has since attracted enormous research interest because of its outstanding physical properties. The electronic band structure of graphene near the Fermi energy exhibits a linear conical dispersion around the K and K′ points. Measurements on graphene have revealed the highest mechanical strength of any material[11], unprecedented charge carrier mobilities[12–14], and infrared plasmons[15]. Raman spectroscopy of graphene has been used to establish the layer number[16] and investigate strain[17,18] and doping.

Single-walled carbon nanotubes are a set of one-dimensional materials that can be thought of as rolled-up graphene sheets. In single-walled carbon nanotubes, first discovered in 1993[19], the carbon atoms are arranged in a hexagonal lattice on a cylindrical surface and the diameter of the tube ranges from about 0.5 to 2 nm. As there are many ways of rolling up a graphene sheet, there are many possible carbon nanotube structures, which can have metallic or semiconducting electronic character. Raman spectroscopy is a useful method for the characterization of carbon nanotube samples and gives information such as nanotube diameter, chirality[20], semiconducting or metallic character[21], and defect density[22].

Commonly used techniques for charging sp^2 carbons include electrostatic gating[1] and electrochemical gating[2–4]. The Raman response of graphene has also been monitored under exposure to potassium[5,6] and rubidium[7] vapor, which resulted in the highest doping strengths observed to date.

Of these three techniques, electrostatic gating achieves the lowest charge carrier concentrations. It is typically realized by contacting graphene or nanotubes on a Si/SiO_2 wafer and applying a voltage between the (highly doped) Si and the contacted sample material, so that the SiO_2 layer acts as a parallel plate capacitor. The advantages of electrostatic doping are that it does not require the sample material to be covered in electrolyte as in electrochemical gating or kept in vacuum as for the exposure to alkali metal vapor.

Electrochemical gating works through the formation of an electric Debye layer at the interface of the sample material and an electrolyte. In this configuration the Debye layer can be seen as a parallel plate capacitor with a plate distance of a few nanometers, which is far smaller than for electrostatic gating through

an e.g. 300 nm thick SiO_2 layer. Electrochemical gating thus yields doping levels far exceeding those in electrostatic gating, with the maximum doping level depending on the electrolyte. In the literature, a Fermi energy of 0.8 eV[4,23] has been reported in graphene using a mixture of an ionic liquid and a polymer as the electrolyte.

Exposure to alkali metal vapor requires that the sample be kept under high vacuum conditions, for instance in an evacuated and sealed quartz ampule. It has been widely used for the production of graphite intercalation compounds, where an intercalant species is introduced into the space between the layers of a graphite crystal. Graphite intercalation compounds have been studied for decades[24] and were shown to exhibit modification of the interlayer spacing and charging of the graphite layers. Superconductivity has been demonstrated with a transition temperature of 11.5 K in CaC_6[8](one calcium atom per six carbon atoms). Raman spectroscopy in graphite intercalation compounds can be used to identify the stage number, i.e. how many intercalant atoms there are per carbon atom and how they are arranged in the crystal, as well as strain in the graphene layers[25].

In this thesis, firstly, I use exposure to alkali metal vapor to produce highly doped monolayer graphene, which I then study using reflectivity spectroscopy in chapter 2 and Raman spectroscopy in chapter 3. Secondly, I study single-walled carbon nanotubes using electrochemical gating in combination with *in-situ* Raman spectroscopy in chapter 4. I now give a motivation and introduction for these two parts of the thesis in order.

Superconductivity has not been observed experimentally in graphene. However, theoretical studies have predicted LiC_6 monolayer graphene to exhibit phonon mediated superconductivity with a critical temperature T_c of 8.1 K[9], while the critical temperature for bulk LiC_6 is only 0.9 K. By contrast, the transition temperature in monolayer CaC_6 was predicted to be only 1.4 K, almost an order of magnitude lower than the bulk value.

Alkali metal doping is thus a promising method to modify and tune the physical properties of graphene, and the predictions outlined above illustrate a need for experimental investigations into the vibrational properties of intercalated monolayer graphene. For undoped materials there are pronounced differences in the Raman spectrum of graphene and graphite, but these differences are well understood. The initial measurements on potassium-doped graphene also show changes from the Raman spectrum of bulk KC_8[6]. In this thesis I aim to comprehensively characterize the Raman behavior of monolayer potassium-doped graphene, which will allow a better understanding of the origin of the observed Raman signal and the differences from the bulk.

I begin by investigating the doping strength obtained by evaporating potassium on graphene. To this end I measure the optical reflectivity in the visible range and compare it to a model I develop based on a cut-off in the absorption of doped graphene and corresponding changes in the refractive index. Experiment and theory show good agreement and allow me to extract the Fermi energy in potassium-doped graphene. I obtain a value of 1.3 eV, in agreement with previous angle-resolved photoemission measurements on KC_8[26] and on potassium-doped graphene[27].

I conduct a Raman spectroscopy study of potassium doping of graphene as a function of doping time, and observe the appearance of a broad and asymmetric peak at a peak position much lower than that of the doped G line. I investigate this peak over a broad range of laser excitation energies and find that the peak position increases monotonously as a function of laser energy. By contrast, the peak width and asymmetry both exhibit maxima at a laser energy of twice the Fermi energy. These observations are in disagreement with the behavior of the G mode in less strongly doped graphene.

Investigating the Raman peak in potassium-doped graphene as a function of layer number, I find unexpectedly small changes, in contrast to the Raman spectrum of pristine graphene. I also characterize the polarization behavior of the Raman signal of potassium-doped graphene in linear and circular polarizations. Here I find that the new asymmetric peak shows A_{1g} and E_{2g} symmetry, as opposed to the purely E_{2g} symmetry of the G peak. I therefore conclude that the asymmetric peak observed in potassium-doped graphene is not the result of a continuation of the behavior of the G mode at very high doping strengths, but a completely new peak originating from a different Raman process.

In chapter 4, I first present a study that was initially motivated by the observation of differences in the Raman spectrum of nanotubes in solution and nanotubes deposited onto substrates: The longitudinal optical phonon Raman peak of metallic nanotubes upshifts and the line width narrows when the nanotubes are deposited onto a substrate. The Raman signal of semiconducting tubes remains unchanged. I explain these observations as being caused by shifts in the Fermi energy that affect the Kohn anomaly in the longitudinal optical phonon branch in metallic nanotubes. I then use *in-situ* electrochemical Raman measurements to show that it is possible to reproduce the spectra in solution by deliberately shifting the Fermi energy, and to quantify the Fermi energy shift. I make quantitatively similar observations for several different samples. These results impact the application of Raman spectroscopy to distinguish between metallic and semiconducting tubes by examining the high-energy mode lineshape.

In the the last part of chapter 4, I present an electrochemical Raman spectroscopy study of carbon nanotube energy transfer complexes. Because nanotubes have low absorption strengths and different chiralities require different excitation energies, carbon nanotube energy transfer complexes have recently been created[28–33] to overcome these shortcomings. In these energy transfer complexes, a dye molecule featuring a higher absorption strength is brought close to the nanotube. The energy transfer process unfolds as follows: the dye is excited by an incoming photon, the excitation is then transferred into the nanotube, and finally the nanotube emits a photon in the near infrared. This energy transfer process is very efficient, which means that almost every excitation in the dye is transferred into the nanotube[28,30,32].

I present an *in-situ* electrochemical Raman study on carbon nanotube energy transfer complexes which were produced with three different dye molecules. The electrochemical charging characteristics of the energy transfer complexes is different compared to a reference sample. They exhibit a lower gating efficiency and a shifted voltage position of the charge neutrality point. I quantify the Fermi

energy of complexes in solution and conclude that charge transfer between the dye and the nanotubes cannot explain the photoluminescence quenching observed in previous works for some of these complexes.

2 | Reflectivity of Potassium-doped Graphene

In this chapter I show the results on the reflectivity of potassium-doped graphene. I begin by introducing graphene and its physical properties, in particular its optical properties, and outlining a formalism to calculate the reflectivity of layered systems. I use this formalism to calculate the reflectivity of doped graphene on a silicon substrate and compare the results to measurements on potassium-doped graphene.

2.1 Theoretical Background

2.1.1 Graphene

Graphene is a two-dimensional allotrope of carbon where the atoms are arranged in an sp^2-bonded hexagonal lattice. As a single layer of atomic thickness, it constitutes the building block for graphite (a stack of many graphene layers) and carbon nanotubes (obtained by rolling up a graphene sheet), yet it eclipsed both of those materials in terms of research interest in the past decade[34].

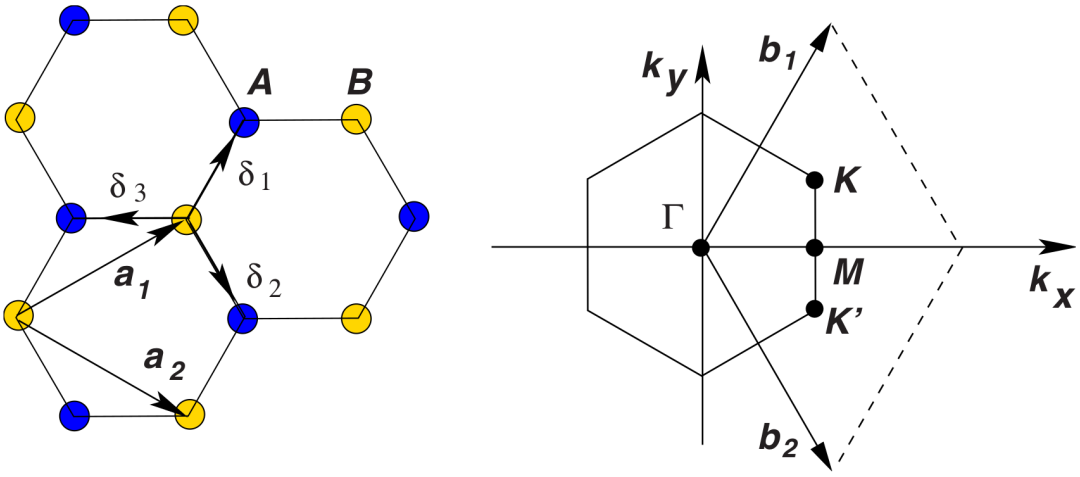

Figure 2.1: Left: Real space structure of graphene. δ_i are the nearest-neighbor vectors and $\mathbf{a}_i$ are the lattice unit vectors. Right: reciprocal space structure of graphene with the reciprocal lattice vectors $\mathbf{b}_i$ and the K and K′ points at the edge of the Brillouin zone. Figure taken from Ref. [35].

In Fig. 2.1, I show the real space structure of graphene, which has two sublattices (labeled A and B in the figure, carbon-carbon distance 1.42 Å), and the Brillouin zone in reciprocal space with the two inequivalent K and K′ points. Graphene's most outstanding property, which gives rise to many of the most interesting physical phenomena observed in the material, is its electronic spectrum within several eV of the Fermi energy. It exhibits a linear dispersion around the K and K′ points, as shown in Fig. 2.2, which means that the electrons behave as massless Dirac Fermions[35].

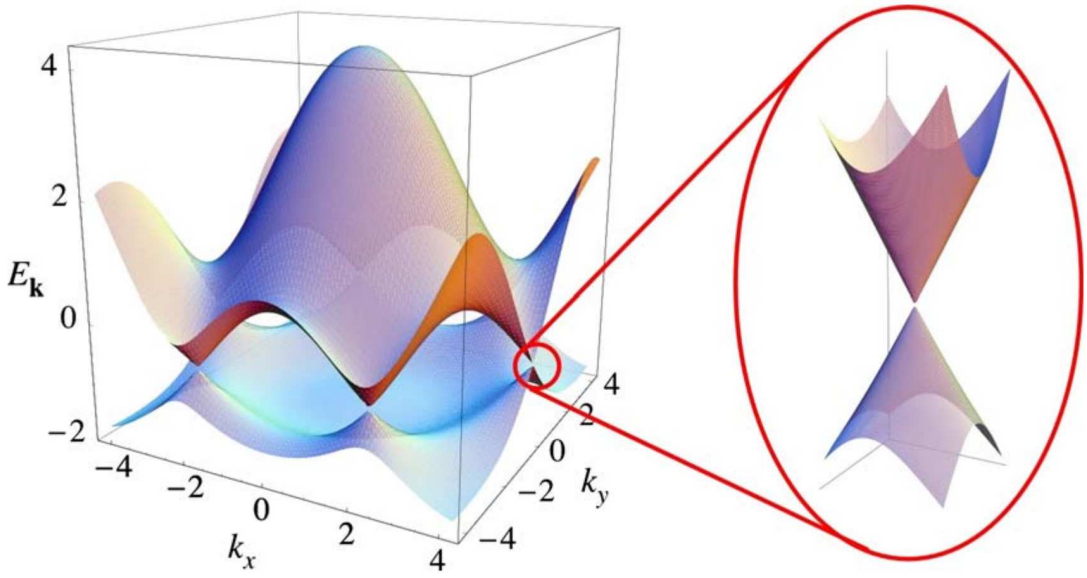

Figure 2.2: Electronic structure of graphene including Dirac cones with linear dispersion. The energy axis is in units of the nearest-neighbor hopping energy t in the tight-binding Hamiltonian ($t = 2.7$ eV). Figure taken from Ref. [35].

A plethora of fascinating physical phenomena were demonstrated in graphene since its discovery. These range from astonishingly high charge carrier mobilities on the order of 100000 $\mathrm{cm^2V^{-1}s^{-1}}$ at room temperature[12–14] to the observation of the quantum Hall effect[36] even at room temperature[37] and the excitation of infrared plasmons[15,38].

The isolation of monolayer graphene was first reported in 2004 by the Geim group in Manchester[10,39,40], who fabricated graphene by mechanical exfoliation of graphite using sticky tape. Mechanically exfoliated graphene has very good quality with few to zero atomic defects, and desirable electronic properties such as high charge carrier mobility. The mechanical exfoliation technique is limited to the production of minuscule quantities, i.e. single flakes with lateral dimensions of hundreds of μm. Several alternative techniques were developed that produce larger quantities of graphene, such as chemical vapor deposition (CVD), epitaxy on SiC, and liquid phase exfoliation. Disappointingly, these techniques have yet to produce graphene with such outstanding electronic qualities as mechanically exfoliated graphene.

2.1.2 Optical Properties of Graphene

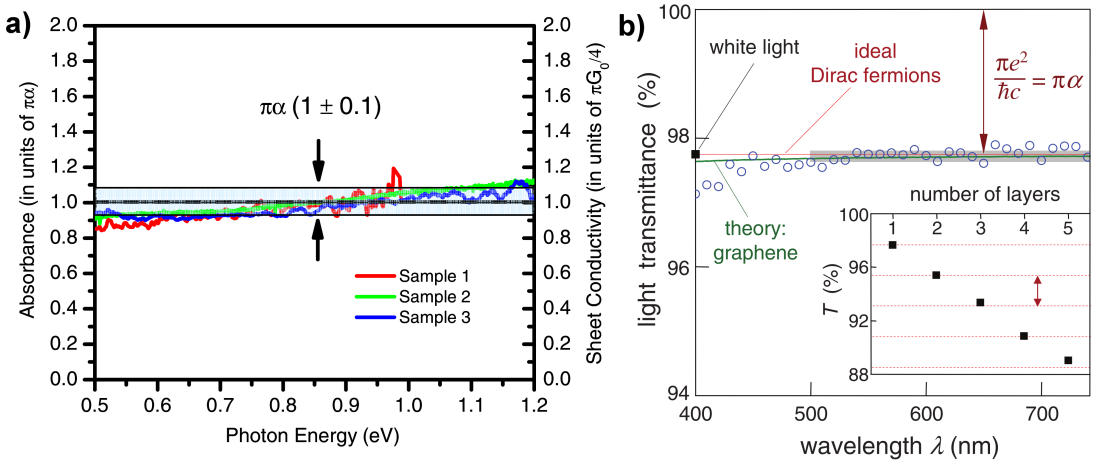

Figure 2.3: Left: Absorbance of single layer graphene in the infrared, showing a value of $\pi\alpha$. Figure taken from Ref. [41]. Right: Transmittance of graphene in the visible, showing a value of $1 - \pi\alpha$. The inset shows that the absorbance increases linearly with layer number. Figure taken from Ref. [42].

Graphene's most well-known optical property is its flat absorbance of $\pi\alpha = 2.3\%$ across a broad spectral range including the infrared and the visible[41,42], where $\alpha = e^2/4\pi\epsilon_0\hbar c$ is the fine structure constant. This property was observed experimentally (Fig. 2.3) and can be calculated using Fermi's Golden Rule and considering graphene's linear electronic bands close to the Fermi energy[42].

As the absorption coefficient a is related to the imaginary part of the refractive index k by

$$a = 4\pi k/\lambda, \tag{2.1}$$

we expect a linear increase of k for increasing wavelengths, which was indeed measured in Ref. [43] for wavelengths above 400 nm. I reproduce their data for the dielectric function and the complex refractive index of graphene in Fig. 2.4. Graphene's absorption in the infrared and visible is caused by electronic inter-

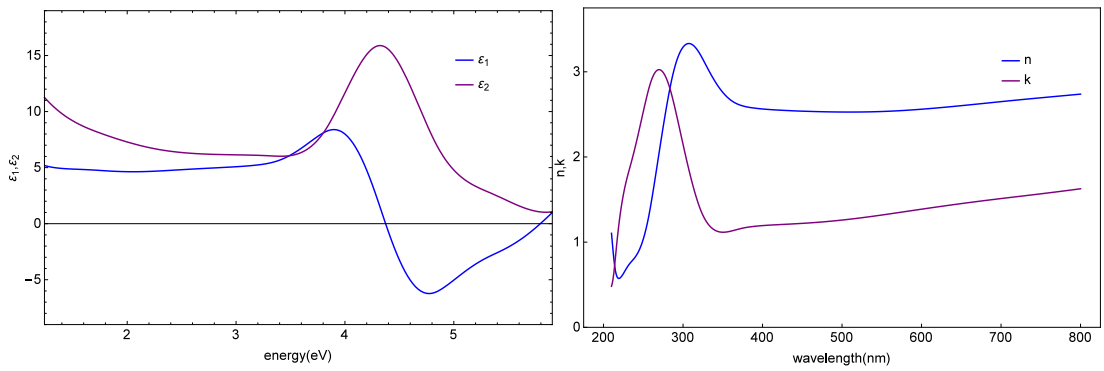

Figure 2.4: Real and imaginary parts of the dielectric function (left) and the refractive index (right) of pristine graphene. Results are reproduced from Ref. [43].

band transitions, which can be blocked by doping. At a given Fermi energy E_F, transitions up to $2E_F$ are blocked and the absorption at energies up to E_F is reduced to zero[4]. This phenomenon affects the reflectivity of potassium-doped graphene and will be discussed in detail later.

2.1.3 Reflectivity of Layered Systems

In the rest of this chapter I am interested in the reflectivity of graphene on a Si/SiO_2 substrate, a system with three layers. The reflectivity of layered systems can be calculated fairly easily using the refractive indices and the thicknesses of the different layers as input data. The calculation will be outlined in this section. For some materials the complex refractive index $\tilde{n} = n + ik$ is not available in the literature, but can be calculated from the dielectric function as follows:

$$\begin{aligned} n &= \sqrt{\frac{1}{2}\left(\sqrt{{\varepsilon_1}^2 + {\varepsilon_2}^2} + \varepsilon_1\right)} \\ k &= \sqrt{\frac{1}{2}\left(\sqrt{{\varepsilon_1}^2 + {\varepsilon_2}^2} - \varepsilon_1\right)}, \end{aligned} \tag{2.2}$$

where ε_1 and ε_2 are the real and imaginary part of the dielectric function. I will only consider light incident perpendicular to the surfaces and interfaces of the layered system in this section. For simplicity, the incoming light will always come from above the layered structure and travel downwards. I first consider an interface between to semi-infinite materials with refractive indices $\tilde{n}_2$ and $\tilde{n}_1$, where the incoming wave travels in the material with refractive index $\tilde{n}_2$. The ratio of the amplitudes of reflected and incoming waves is

$$r = \frac{\tilde{n}_2 - \tilde{n}_1}{\tilde{n}_2 + \tilde{n}_1}. \tag{2.3}$$

I will refer to r as the reflection coefficient of the interface. When light of a wavelength λ passes through a layer of a material with refractive index $\tilde{n}$ and thickness d, it experiences a phase shift of

$$b = 2\pi\tilde{n}\frac{d}{\lambda}. \tag{2.4}$$

I now define a so-called Fresnel coefficient for a layered system consisting of two semi-infinite materials sandwiching a layer of a given thickness. In the actual calculations performed, the top semi-infinite material is always air and the bottom semi-infinite material is silicon. I call the reflection coefficient between the top semi-infinite material and the sandwiched layer r_2, the phase shift of the incident light in the sandwiched layer b and the reflection coefficient between the sandwiched material and the bottom semi-infinite material r_1. The Fresnel coefficient is given by

$$a_1 = \frac{r_2 + r_1 e^{-2ib}}{1 + r_1 r_2 e^{-2ib}}. \tag{2.5}$$

The reflectivity of this stack is $R = |{a_1}^2|$. It is very easy to add another sandwiched

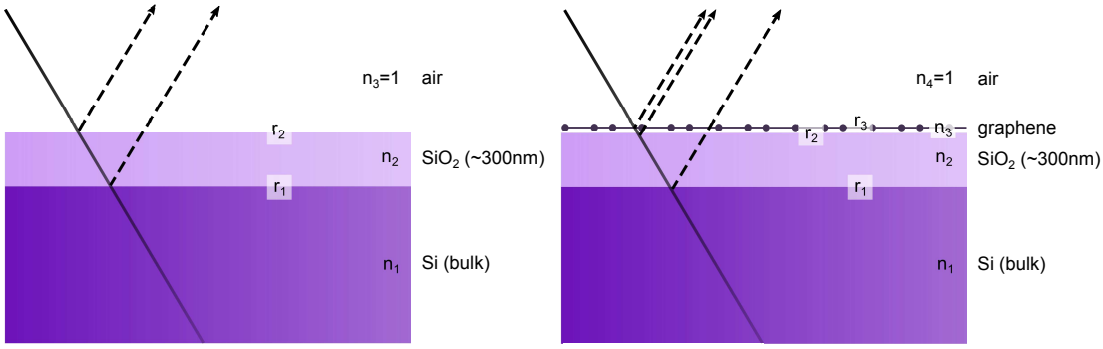

Figure 2.5: Geometry and parameters for a stack of three materials (left: Si, SiO_2, air) and four materials (right: Si,SiO_2, graphene, air).

layer using this formalism. Given materials one through four with refractive indices $\tilde{n}_1 - \tilde{n}_4$, I first calculate, as described above, the Fresnel coefficient a_1 of a stack of a semi-infinite layer of material three, a sandwiched layer of material two, and a bottom semi-infinite layer of material one. To go from this structure to the desired structure with two sandwiched layers, if the reflection coefficient between materials four and three is r_3, and the phase shift in the top sandwiched layer is b_2, Fresnel coefficient of the complete layered structure can be calculated as

$$a_2 = \frac{r_3 + a_1 e^{-2ib_2}}{1 + r_3 a_1 e^{-2ib_2}}. \tag{2.6}$$

The reflectivity of the whole stack is $R = |a_2{}^2|$. Note that the Fresnel coefficient of the stack of the bottom three materials appears in place of the bottom reflection coefficient in the three-material stack.

2.1.4 Reflectivity of Graphene on SiO_2/Si

The optical reflectivity in the visible spectral range of graphene was investigated in detail before[44]. It was shown that reflectivity spectroscopy is a useful tool especially to distinguish between areas with different layer numbers. In this section I will show that my results match those in the literature. To the best of my knowledge, the reflectivity of doped graphene has not been investigated. This section will thus act as an introduction for my results on this topic, which are presented in section 2.3.

Figure 2.6 shows the reflectivity of a monolayer graphene flake on a SiO_2/Si substrate as well the reflectivity of the bare substrate. The reflectivity is lower for the area covered by graphene at energies around 2.1 eV. The contrast spectrum in Ref. [44] is calculated as $(I_{\mathrm{Si}} - I_{\mathrm{graphene}})/I_{\mathrm{Si}}$ and can be understood as a normalized difference spectrum. In this case the lower reflectivity for graphene leads to a peak with positive amplitude in the contrast spectrum. This is indeed seen in Fig. 2.7, which furthermore shows that the contrast increases approximately linearly with layer number, and that the experimental measurements show very good agreement with calculations based on the formalism outlined in the preceding section.

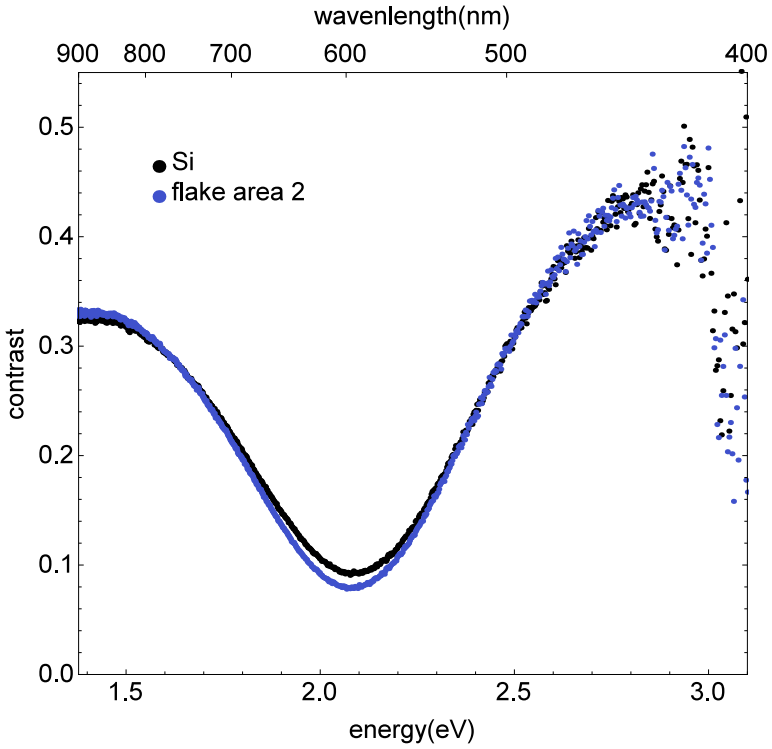

Figure 2.6: Experimental reflectivity of monolayer graphene on Si/SiO_2 (blue) and of the bare substrate (black).

2.1.5 Summary

In summary, I have detailed a formalism for the calculation of the reflectivity of layered systems as well as its application to graphene on Si/SiO_2. This chapter should serve as a broad enough basis for the understanding of the reflectivity spectra of potassium-doped graphene that are reported in this thesis.

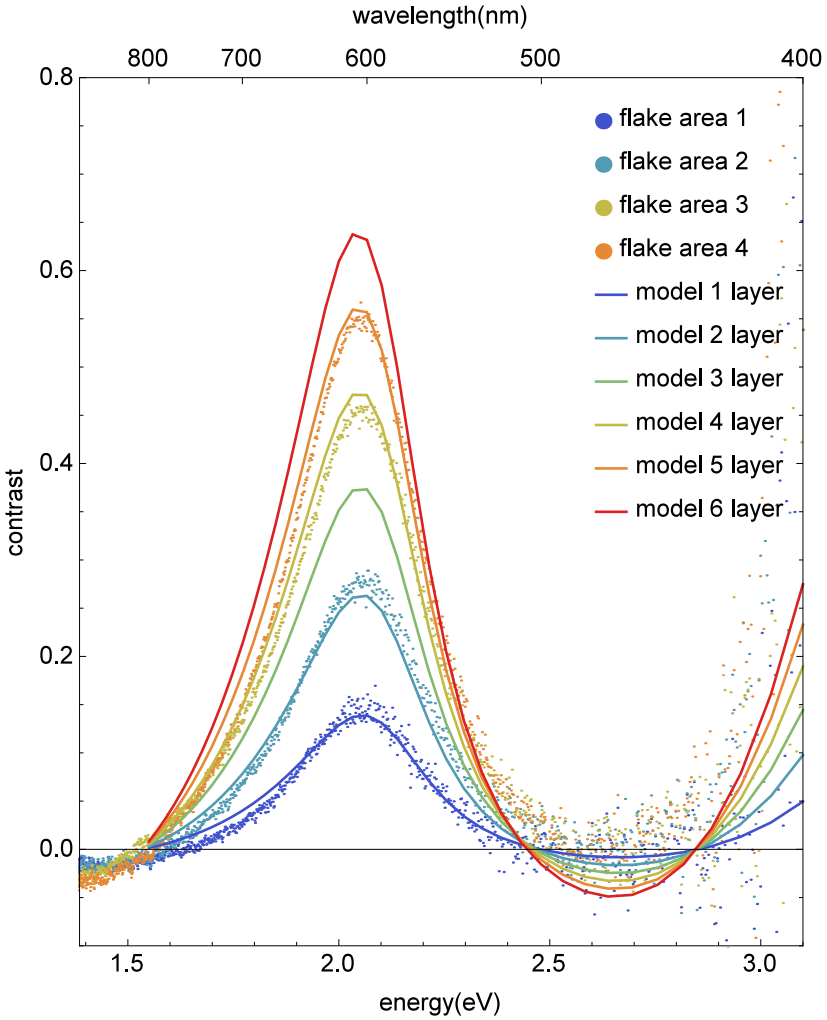

Figure 2.7: Experimental and calculated contrast for graphene on Si/SiO_2 for one to six layers.

2.2 Experimental Methods

2.2.1 Two Zone Vapor Intercalation and Sample Preparation

In order to produce the fully doped graphene samples, pristine graphene and atomic potassium (typically 99.95% purity from Sigma Aldrich) are placed in a glass tube that is closed on one end (5mm thickness) in a glove box. The tube is then evacuated and sealed on the other end, leaving the sample and the potassium in vacuum in the opposing ends of the glass ampoule. To evaporate potassium, the ampoule is enveloped in a heating wire. I then pass a d.c. current (typically 1 A at 12 V) through the wire, monitor the temperature and adjust the current to maintain a temperature of 140° C. The ampoule is kept at this temperature for three days, at which point the graphene is fully doped. The resulting sample is stable on a timescale of months.

2.2.2 Reflectivity Spectrometer

The setup used to measure reflectivity spectra in this thesis consists of a Nikon Eclipse LV100D-U optical microscope with a 50 W halogen lamp as the light source, together with a Horiba iHR320 spectrometer and nitrogen-cooled Symphony II detector. The reflected light is collected by an optical fiber and fed to the spectrometer entrance. A 300 lines/mm grating is used to cover a wide spectral range from 400 to 900 nm.

2.2.3 Summary

Summarizing the description of my experimental methods, I have listed the preparation method for potassium-doped graphene in a sealed evacuated ampoule, as well as an array of optical spectrometers. These will allow us to measure the Raman spectra of the samples over an extremely broad energy range and with polarization control, as well as their reflectivity.

2.3 Results

2.3.1 Modeling the Refractive Index of Doped Graphene

In this section I present my model for the reflectivity of doped graphene. The most important idea behind it can be outlined as follows:

- In doped graphene electronic transitions with energy smaller than twice the Fermi energy are blocked because for negative Fermi energies, the valence band state is not occupied, and for positive Fermi energies, they are forbidden by the Pauli principle.
- The absorption is governed by the imaginary part k of the complex refractive index $\tilde{n} = n + ik$. Thus to model the reflectivity of doped graphene with a Fermi energy of e.g. 0.5 eV, I introduce a cut-off in k with a broadened step function at 1 eV.
- Given this function for k, the real part of the complex refractive index, n, can be calculated by taking the Kramers-Kronig transform of k.
- This gives us complete knowledge of the complex refractive index of doped graphene, which is sufficient to model its reflectivity.

In practice I take the b-spline parameters for ε_2 in Ref.[43], and compute ε_1 by Kramers-Kronig transform as follows:

$$\varepsilon_1(\omega) = 1 + \frac{2}{\pi} P \int_0^\infty \frac{\omega' \varepsilon_2(\omega')}{\omega'^2 - \omega^2} d\omega' = 1 + \frac{2}{\pi} \int_0^\infty \frac{\omega' \varepsilon_2(\omega') - \omega \varepsilon_2(\omega)}{(\omega' + \omega)(\omega' - \omega)} d\omega' \qquad (2.7)$$

From this I can calculate the complex refractive index of pristine graphene according to formula 2.2, as shown in Fig. 2.4. For doped graphene, I introduce a

cut-off in k by multiplying with a broadened step function:

$$k_{\text{doped}}(\omega) = \frac{1}{e^{(\hbar\omega - 2E_F)/\Gamma} + 1}\, k_{\text{pristine}}(\omega), \tag{2.8}$$

where Γ determines the width of the cut-off. From k_{doped}, I can calculate the real part of the refractive index of doped graphene, n_{doped}, again via Kramers-Kronig transform:

$$n_{\text{doped}}(\omega) = 1 + \frac{2}{\pi}\int \frac{\omega' k_{\text{doped}}(\omega') - \omega k_{\text{doped}}(\omega)}{(\omega' + \omega)(\omega' - \omega)} d\omega'. \tag{2.9}$$

In Fig. 2.8 I show the results for n_{doped} and k_{doped} for Fermi energies up to

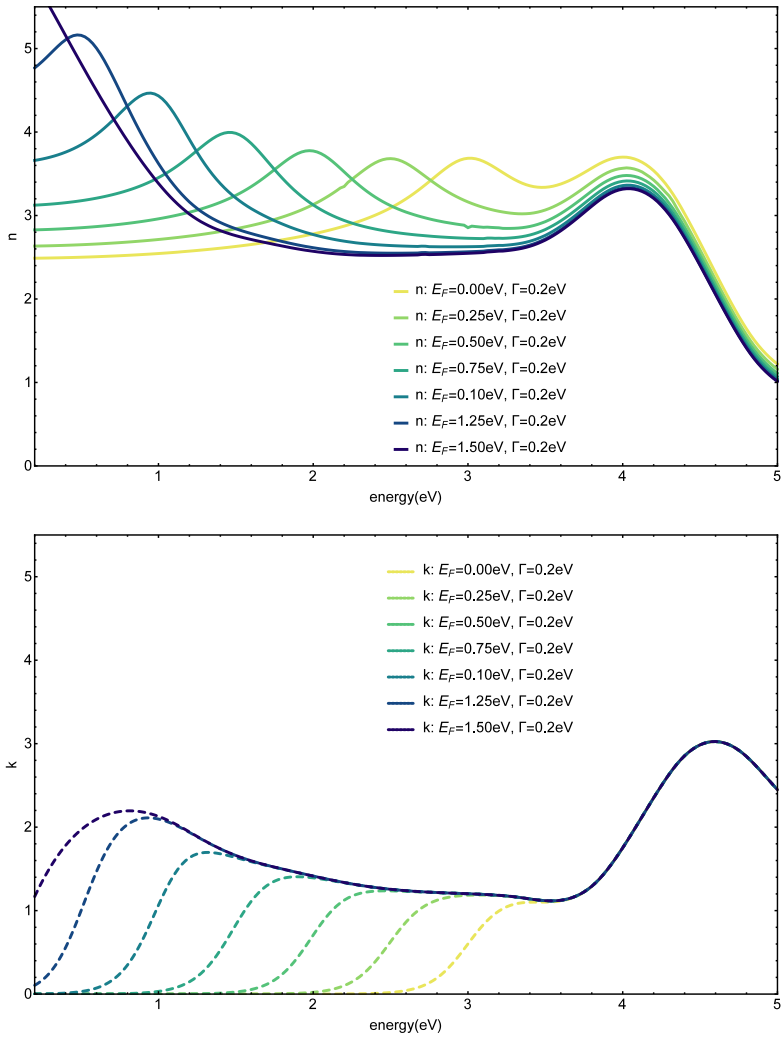

Figure 2.8: Modeled refractive index of graphene for Fermi energies from 0 to 1.5 eV using a width of 0.2 eV for the cutoff in k_{doped}.

1.5 eV. Upon Kramers-Kronig transformation, the cut-off in k leads to a peak in n. I also varied the width of the step function used to introduce the cut-off in k. Here broader widths of the cut-off also lead to broader peaks in n, as can be seen in Fig.2.9. In the following I will use a width of 200 meV, which is close to the value obtained in the infrared transmission spectra of Ref. [4]. Given the

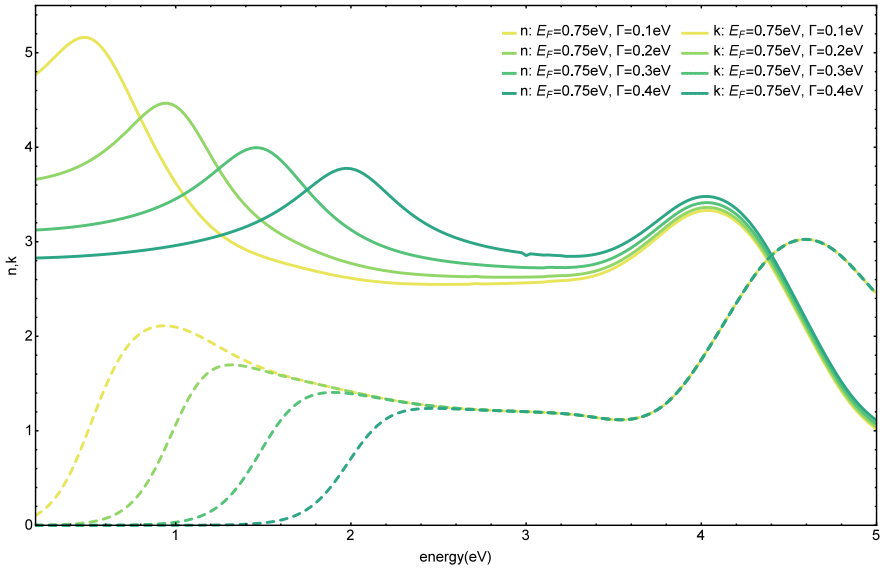

Figure 2.9: Modeled refractive index of graphene for a Fermi energy of 0.75 eV using widths from 0.1 eV to 0.4 eV for the cutoff in k_{doped}.

complex refractive index of doped graphene, along with the refractive indices of Si and SiO_2 and the thickness of the SiO_2 layer in my sample, I can then calculate the reflectivity and the contrast spectrum the same way as described in Sec. 2.1.3. The results of this calculation are shown in Fig. 2.10 for Fermi energies between 0 and 1.5 eV.

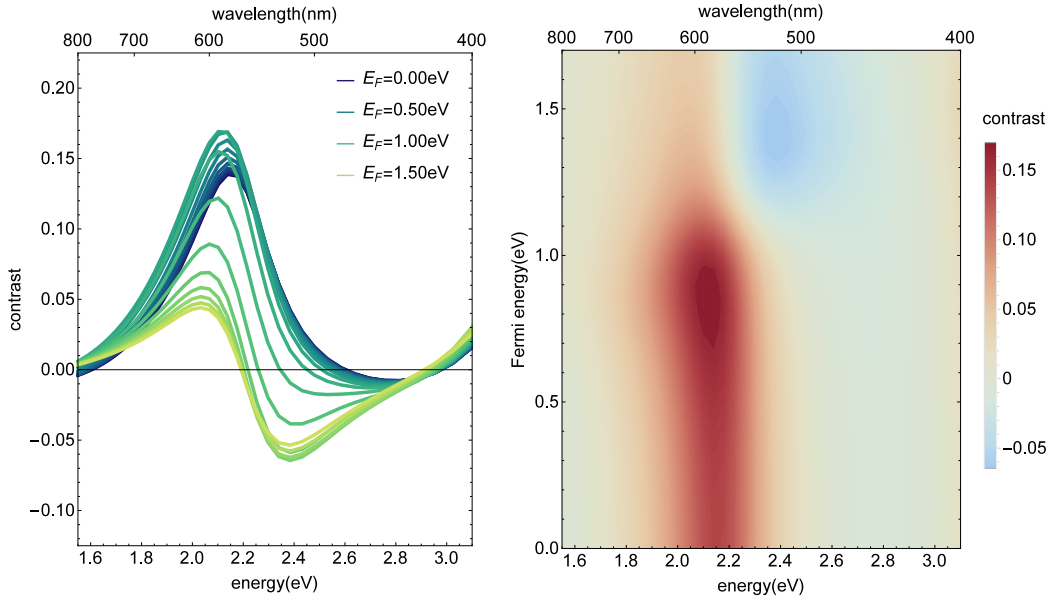

Figure 2.10: Left: Modeled contrast spectrum of graphene for Fermi energies from 0 (dark blue) to 1.5 eV (yellow). Right: Same data as left presented as a contour plot with increasing Fermi energy from bottom to top. Negative contrast is blue, positive contrast is red.

The behavior of the reflectivity of graphene with increasing doping level can be described as follows:

- Initially, the contrast spectrum is largely unchanged up to a Fermi energy of 0.5 eV.
- The peak in the contrast spectrum increases slightly in intensity and downshifts in energy, to 2.12 eV for 0.9 eV Fermi energy.
- The spectrum then starts to exhibit a dip at around 2.4 eV in addition to the peak, starting at Fermi energies of 1.1 eV.
- The zero-crossing in the contrast spectrum shifts to lower energies with increasing Fermi energy, and the intensity ratio of dip to peak approaches unity.
- For Fermi energies larger than 1.5 eV the intensities of dip and peak decline simultaneously, while the zero-crossing stays at a fixed energy of 2.2 eV.

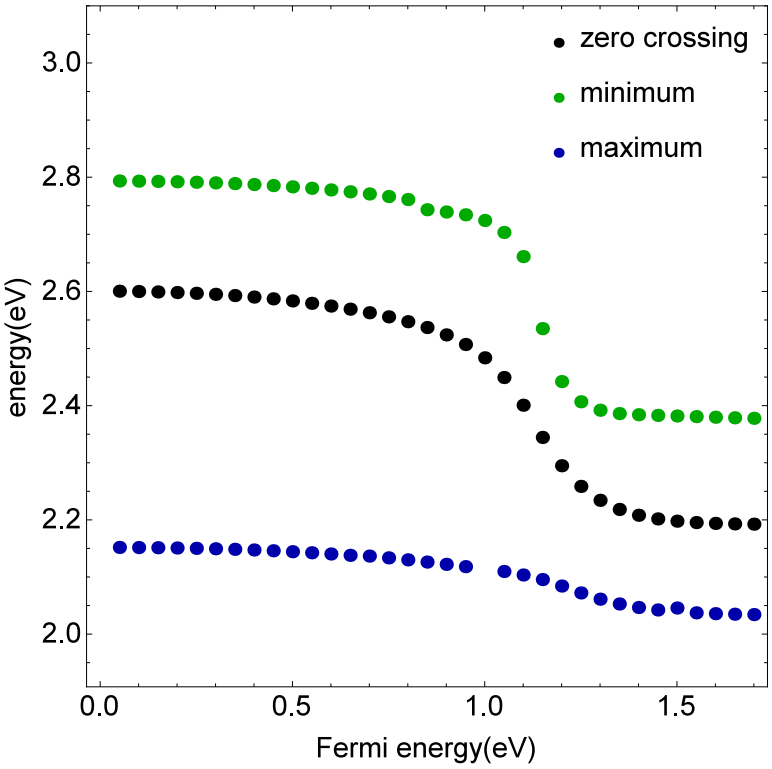

Figure 2.11: Energy at which the maximum contrast (blue), zero contrast (black), and minimum contrast (green) occur in the modeled reflectivity spectra as a function of Fermi energy.

I plot the position of the maximum contrast, the zero crossing, and the minimum contrast in Fig. 2.11. The position of the maximum changes by less than 0.2 eV,much less than that of the zero crossing and the minimum, which change by 0.4 eV.

2.3.2 Reflectivity Spectrum of Potassium-Doped Graphene

The reflectivity spectrum of potassium-doped monolayer graphene on Si/SiO_2 was measured as described in Sec. 2.2. My results are shown in Fig. 2.12, alongside a calculation using the model described above for doped graphene with a Fermi energy of 1.3 eV.

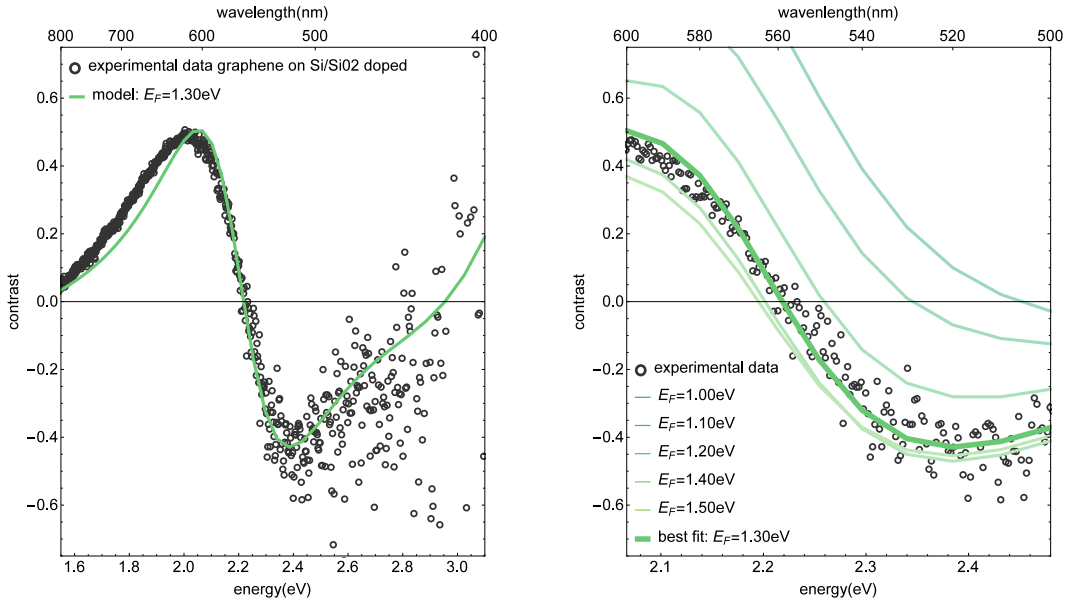

Figure 2.12: Left: Modeled contrast spectrum for a Fermi energy of 1.3 eV compared to experimental data of potassium-doped graphene on Si/SiO_2. Right: Same data as left in the region of the zero crossing, compared to calculations using different Fermi energies.

Clearly, the contrast of doped graphene is markedly different from that of undoped graphene. Instead of a single peak at 2.1 eV, the spectrum exhibits a dip at around 2.4 eV and a peak at around 2 eV. The intensity ratio of dip and peak is slightly smaller than unity. It can be seen from Fig. 2.12 that the calculated contrast spectrum using a Fermi energy of 1.3 eV successfully reproduces many of the characteristics of the experimental spectrum, namely:

- The dip and peak in the spectrum, as well as their intensity ratio of approximately 0.8.
- The position of the zero crossing at 2.2 eV, as well as the slope there.
- The trend to zero contrast for longer wavelengths.

For energies above below 2.3 eV, the experimental spectrum is very noisy because the contrast is normalized by dividing by the reflectivity of Si, which is small in this range. For energies lower than 1.9 eV, while the calculated spectrum exhibits

the same trend of the signal approaching zero contrast, it does not exactly match the experimental spectrum.

The right panel in Fig. 2.12 elucidates how precisely the Fermi energy can be determined from the reflectivity spectrum by comparing the region with the zero crossing in the experimental spectrum to calculations using Fermi energies ranging from 1.0 to 1.5 eV. Clearly the experimental response is in agreement only with the calculation at 1.3 eV, giving a precision of 100 meV. This could arguably be improved by calculating the refractive index of doped graphene for a range of Fermi energies with a step size of less than 100 meV.

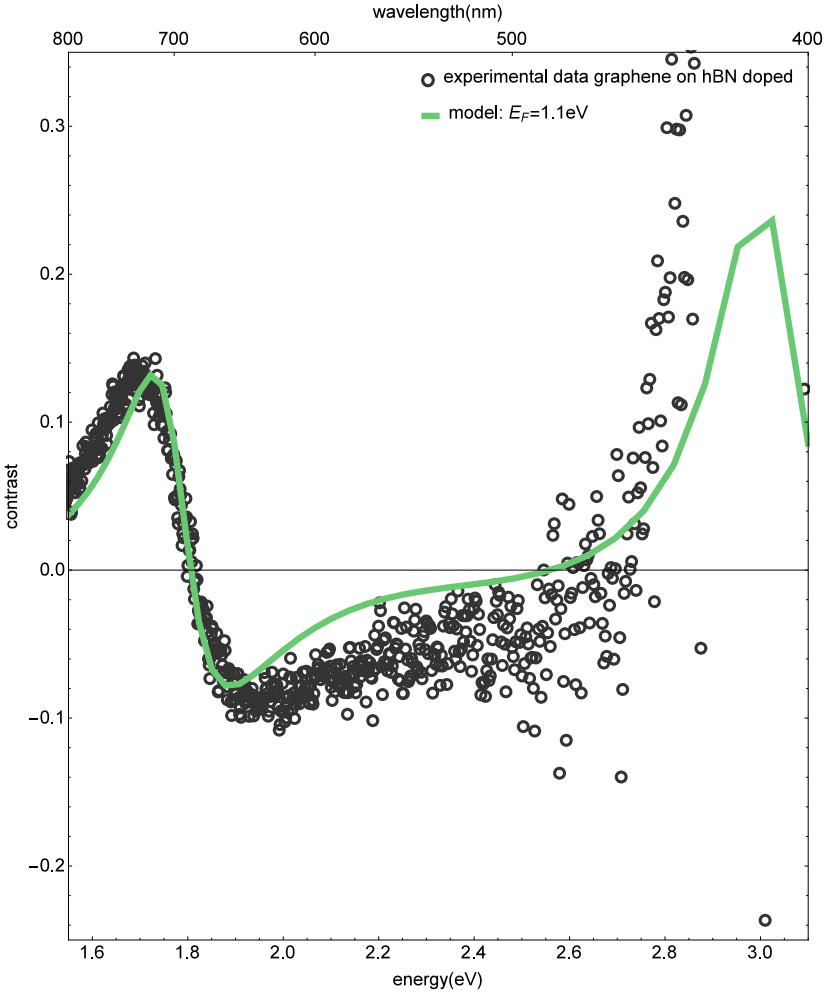

Figure 2.13: Left: Modeled contrast spectrum for a Fermi energy of 1.1 eV compared to experimental data of potassium-doped graphene on hBN.

In addition to the measurement of the reflectivity of potassium-doped graphene on Si/SiO_2, I have also potassium-doped graphene produced using an identical procedure but on hexagonal boron nitride (hBN) on Si/SiO_2. Figure 2.13 shows the resulting reflectivity spectrum. The spectrum resembles that on Si/SiO_2, exhibiting for increasing energies first a peak and then a dip. The most distinctive difference is that the peak, the zero crossing, and the dip are all shifted to higher wavelengths, with e.g. the zero crossing being at 1.8 eV on

hBN instead of at 2.2 eV on Si. I have amended my calculation of the reflectivity spectrum to also include a hBN layer between the graphene and the Si/SiO_2. The resulting spectrum calculated for a Fermi energy of 1.1 eV is shown in Fig 2.13 alongside the experimental data. In analogue to my observations for Si/SiO_2, the calculation reproduces well the dip/peak structure, as well as position of the zero crossing and the slope of the data there.

The Fermi energy values of 1.3 eV on Si/SiO_2 and 1.1 eV on hBN are quite similar to that of 1.35 eV for bulk KC_8 determined from ARPES. This establishes that potassium doping of single layer graphene can achieve higher doping levels than even the most efficient electrochemical gating using a polymer-reinforced electrolyte gel[4], which reached 0.85 eV. Obviously this also means that potassium doping is far superior to any electrostatic doping technique in terms of maximum achievable Fermi energy.

I now turn towards a discussion of the measurements of the reflectivity of doped graphene in combination with the simulations presented here as a novel method for determining the Fermi energy of highly doped graphene. The reflectivity measurements are fast with integration times on the order of seconds, and require only a lamp for excitation and a single grating spectrometer and a CCD for detection. The simulations to which the experimental spectra are compared are more time demanding, but this is mostly due to the calculation of the refractive index of doped graphene, which employs a numerical integration step for the Kramers Kronig transformation. This calculation only has to be performed once, and can then be employed together with the sample parameters (thickness and refractive indices of the substrates) to calculate the reflectivity spectrum in a matter of seconds. From my calculations I extracted the energy position of the contrast zero crossing (shown in Fig. 2.11), which can be used by other researchers to determine the Fermi energy in their sample (provided they also use a SiO_2 thickness of 300 nm).

I can compare my method to the infrared transmission measurements performed in Ref.[4]. These are limited to measuring Fermi energies of below 1 eV. While this range could in principle be extended using visible transmission spectroscopy, all such measurements are only possible on transparent substrates, in contrast to my method. As previously mentioned the Fermi energy in bulk KC_8 has been measured using angle-resolved photo-electron spectroscopy (ARPES). This is obviously a much more demanding technique experimentally which requires synchrotron radiation or tabletop X-Ray sources. Furthermore, the X-Ray beam used in ARPES cannot be focused as tightly as the visible light in my measurements and thus potentially needs larger samples such as CVD graphene, which is of lower electronic quality.

To summarize, my measurement method compares favorably to existing techniques used to measure the Fermi energy in highly doped graphene or graphitic samples. It could furthermore also be expanded to investigate highly doped graphene incorporated in functional heterostructures e.g. with transition metal dichalcogenides.

2.3.3 Reflectivity of Doped Multilayer Graphene

Having discussed the reflectivity of doped monolayer graphene, I now turn to corresponding measurements on bilayer and four- and five-layer graphene, which are found adjacent to the monolayer flake in mysample. The inset of Fig. 2.14 shows an optical micrograph (10x magnification) of the sample after potassium doping. As discussed in the theoretical background section for the reflectivity, for pristine graphene layers the contrast increases approximately linearly with layer number. It is obvious from the micrograph that this no longer holds for doped graphene layers. Instead, it is impossible to differentiate the layers by their reflectivity. This is confirmed by the spectroscopic measurements of the reflectivity, shown in the main panel of Fig. 2.14 for mono-, bi-, four- and five-layer. The contrast is fairly similar for all layer numbers and actually first increases from monolayer to bilayer before then decreasing for four-layer and five-layer.

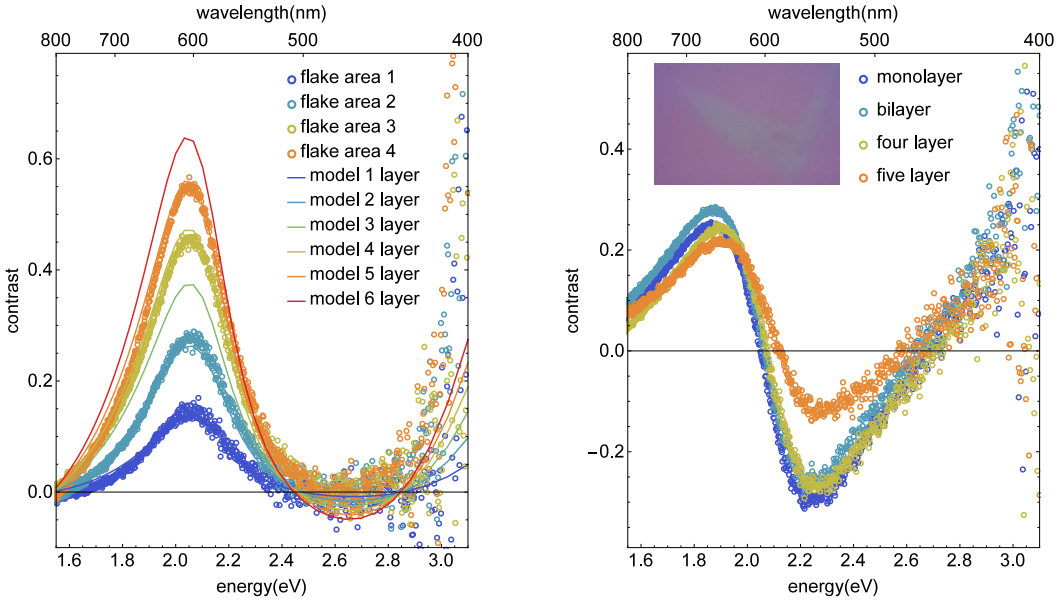

Figure 2.14: Contrast spectra of mono-, bi, four, and five layer graphene before (left) and after (right) potassium doping. The inset shows a micrograph of the sample.

This experimental observation is in disagreement with the predictions from my reflectivity model based on the refractive index of doped graphene. A given Fermi energy in the simulation gives me the refractive index, which I then use to calculate the reflectivity for different layer numbers by considering graphene thicknesses of integer multiples of 0.335 nm in the phase shift $b = 2\pi\tilde{n}\frac{d}{\lambda}$. This results in the contrast spectra shown in Fig. 2.15, which again increase linearly with layer number, just like the experimental and calculated contrast for pristine graphene.

I have tried to rectify this discrepancy between the simulated and experimental contrast for multilayer graphene. I calculate the reflectivity of doped graphene with one to five layers with a layer of potassium on top. The results are shown in Fig. 2.16.

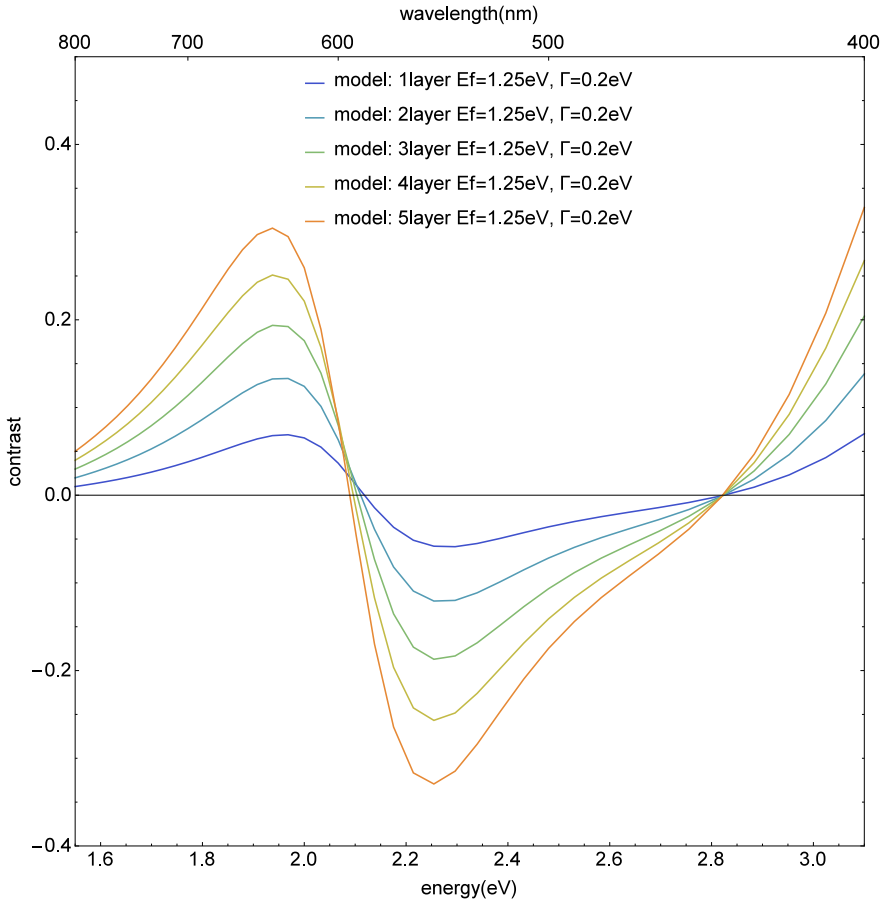

Figure 2.15: Modeled contrast spectra of mono-, bi-, three, four, and five layer graphene with Fermi energy of 1.3 eV. The contrast increases linearly with layer number.

For a 2 nm thick layer of potassium, the spectrum still exhibits intensity approximately linear with layer number, although the contrast is increased below 600 nm and decreased above 600 nm. For larger potassium thickness, such as 15 nm, the contrast is much less dependent on layer number. But it shows a peak followed by a dip, in contrast to my experimental observations. This is because the measured spectrum approaches the reflectivity of potassium and the contrast is then $(I_{\mathrm{Si}} - I_{\mathrm{K}})/I_{\mathrm{Si}}$.

The graphene layer number appears in the phase shift in the Fresnel formalism. There is no way to obtain the same contrast for different layer numbers if all layers share the same refractive index.

The experimentally observed invariance of the contrast with respect to layer number is a theme that will be reprised in the later discussion of the Raman spectra of doped graphene as a function of layer number.

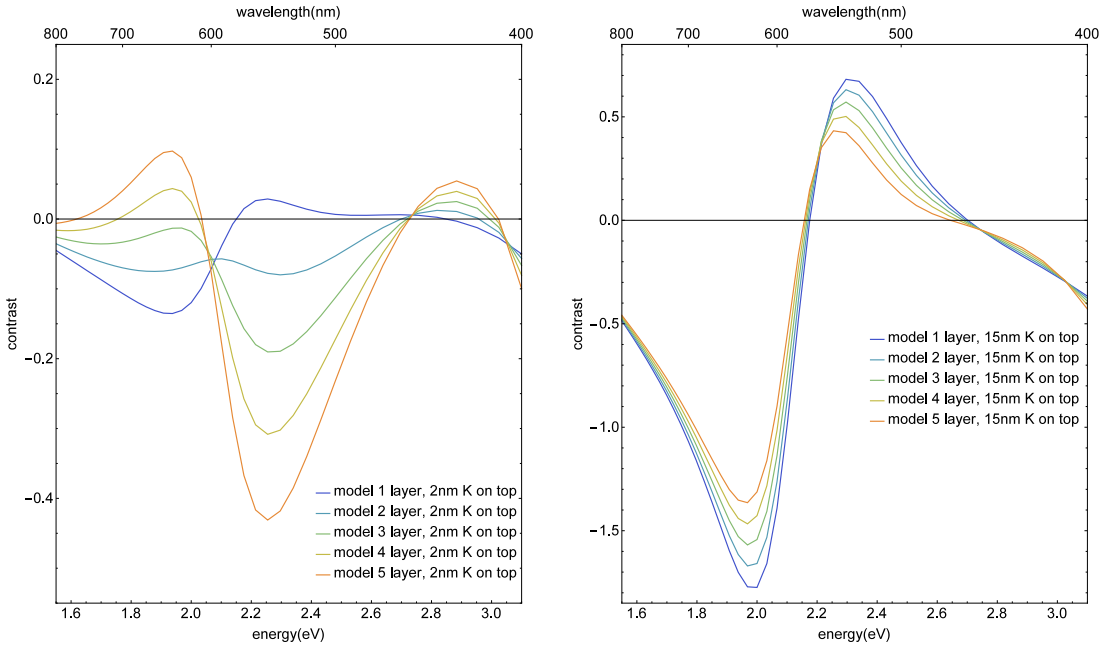

Figure 2.16: Modeled contrast spectra of mono-, bi-, three, four, and five layer graphene with Fermi energy of 1.3 eV and a layer of potassium (2 nm on the left, 15 nm on the right) on top.

2.4 Summary

To sum up, I have introduced a novel formalism to model the refractive index of doped graphene at arbitrary Fermi energies. I have used these results to calculate the reflectivity of doped graphene in my experimental configurations and compared the calculations to experiments for graphene on Si/SiO_2 and hexagonal boron nitride, which show very good agreement. This allows me to determine the Fermi energy in my potassium-doped graphene samples with relatively little experimental effort in comparison to established techniques.

3 | Raman Spectrum of Potassium-doped Graphene

3.1 Theoretical Background

3.1.1 Raman Scattering

The Raman effect refers to the inelastic scattering of light by the system under study. A basic phonon Raman process can be described as follows[45]:

- The incoming photon excites an electron to an excited intermediate state in a vertical transition.
- The electron or the hole it left behind in the valence band are scattered to a second intermediate state under creation or annihilation of a phonon.
- The electron-hole pair recombines radiatively under emission of the outgoing photon.

Raman processes where an excitation (such as a phonon) is created are called Stokes processes, while processes involving annihilation are called Anti-Stokes processes. The Raman process has to satisfy energy and momentum conservation as expressed in the following equations:

$$E_1 = E_2 \pm \hbar\omega \tag{3.1}$$

$$\mathbf{k}_1 = \mathbf{k}_2 \pm \mathbf{q}, \tag{3.2}$$

where E_1 and E_2 refer to the energies of the incoming and outgoing photons, $\hbar\omega$ is the phonon energy, and $\mathbf{k}_1$, $\mathbf{2}_1$, and $\mathbf{q}$ are the wavevectors of the incoming photon, the outgoing photon, and the phonon. The plus and minus signs in the equations refer to Stokes and anti-Stokes scattering, respectively. Since the wavevectors of the photons are very small compared to the size of the Brillouin zone, $\mathbf{q}$ is also limited to very small values, such that only Γ phonons are observable in such a first-order Raman process.

The Raman process described above can take place if the intermediate electronic states mentioned above are virtual states, such as in a Stokes process in a material where the laser energy is less than the band gap. However, the Raman intensity is strongly enhanced if one or both of the intermediate states are

real states. This is reflected in the Raman matrix element $K_{2f,10}$, which can be calculated from third-order perturbation theory[45]:

$$K_{2f,10} = \sum_{a,b} \frac{\langle \omega_2, f, i| H_{\text{el-R},\rho} |0, f, b\rangle \langle 0, f, b| H_{\text{el-ph}} |0, 0, a\rangle \langle 0, 0, a| H_{\text{el-R},\sigma} |\omega_1, 0, i\rangle}{\left(\hbar\omega_1 - E^{\text{el}}_{ia} - i\gamma\right)\left(\hbar\omega_1 - \hbar\omega_{\text{ph}} - E^{\text{el}}_{ib} - i\gamma\right)}. \quad (3.3)$$

Here the sum runs over all intermediate electronic states a, b. $|\omega_1, 0, i\rangle$ is the state with an incoming photon with frequency ω_1, no phonon, and the initial electronic state. f is the final vibrational state, ω_2 is the frequency of the outgoing photon, and ω_{ph} is the phonon frequency. The transitions are mediated by the Hamiltonian for the interaction between electrons and photons of a given polarization $H_{\text{el-R},\rho}$ and the electron-phonon Hamiltonian $H_{\text{el-ph}}$. The terms in the denominator lead to increases in the Raman intensity if the incoming photon energy is in resonance with the energy difference between the initial and first intermediate electronic states or if the outgoing photon energy is in resonance with the energy difference between the initial and the second intermediate electronic states. A divergence is prevented by the $i\gamma$ terms, where γ is the lifetime of the electronic states. The Raman intensity is proportional to $|K_{2f,10}|^2$.

In addition to these first-order Raman processes, second-order processes also play an important role in the Raman spectra of graphene and related materials. These can comprise two-phonon scattering or scattering by a defect in addition to the single phonon scattering. I explain here the latter case.

The defect scattering is assumed to be elastic. It leads to an additional matrix element $\mathcal{M}_{\text{el-def}}$ in the numerator and an additional energy difference term in the denominator of the Raman matrix element, which now reads:

$$K_{2f,10} = \sum_{a,b,c} \frac{\mathcal{M}_{\text{el-R}}\mathcal{M}_{\text{el-def}}\mathcal{M}_{\text{el-ph}}\mathcal{M}_{\text{el-R}}}{\left(\dots\right)\left(\dots\right)\left(\hbar\omega_1 - \hbar\omega_{\text{ph}} - E^{\text{el}}_{ci} - i\gamma\right)} + \text{time order reversed}. \quad (3.4)$$

The $(\dots)$ terms are the terms in the denominator of Eq.3.3. The defect scattering process relaxes the previously mentioned $q = 0$ rule that governs first-order Raman processes, since the electron can scatter with a phonon with finite wavevector q and then be scattered back to its original wavevector in the defect scattering step. This allows phonons away from the Γ point to be probed by Raman scattering. The same is also true for two-phonon scattering.

3.1.2 Raman Spectrum of Graphene

The Raman spectrum of pristine graphene Si/SiO_2 is shown in Fig. 3.1. I will focus in this section on an in-depth discussion of the two most prominent peaks in the spectrum, the G mode at around 1600 cm^{-1} and the 2D mode at around 2700 cm^{-1} [16,46]. To facilitate this discussion I show in Fig. 3.2 the phonon dispersion of graphite as measured by inelastic X-ray scattering[47].

The G mode is a single-phonon Raman mode that arises from out-of-phase in-plane Γ point vibrations of the two carbon atoms in the unit cell of graphene[16,46]. The longitudinal and transversal optical phonon branches of the graphene phonon

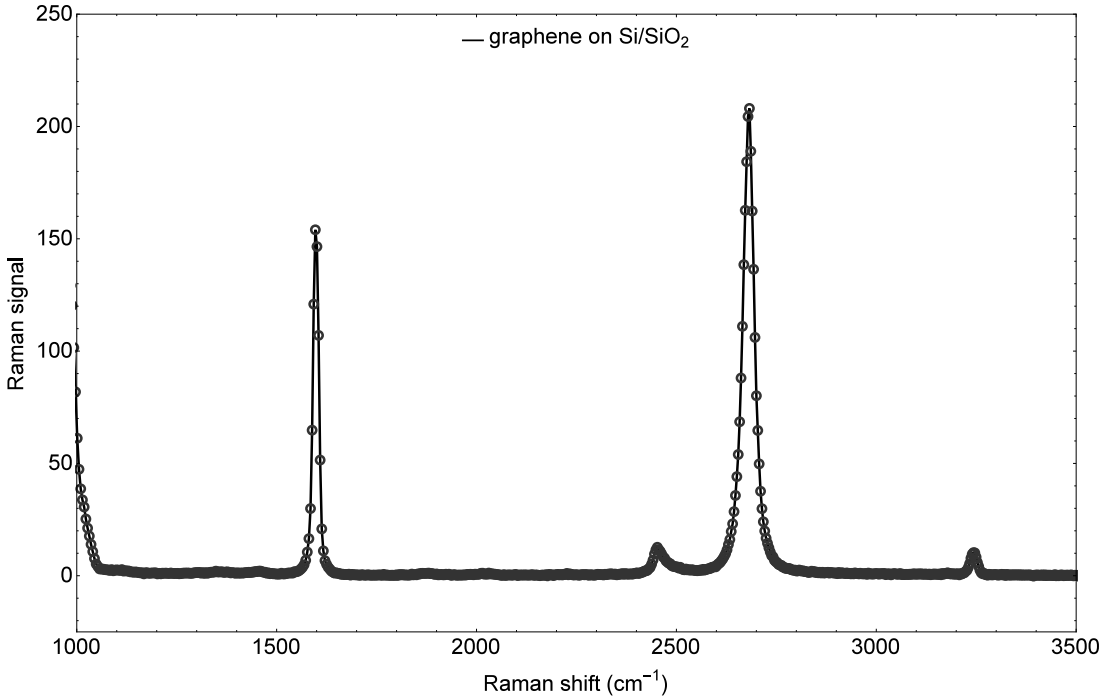

Figure 3.1: Raman spectrum of graphene including the G mode located close to 1600 cm^{-1} and the 2D mode around 2700 cm^{-1}. The origin of these modes is discussed in the text.

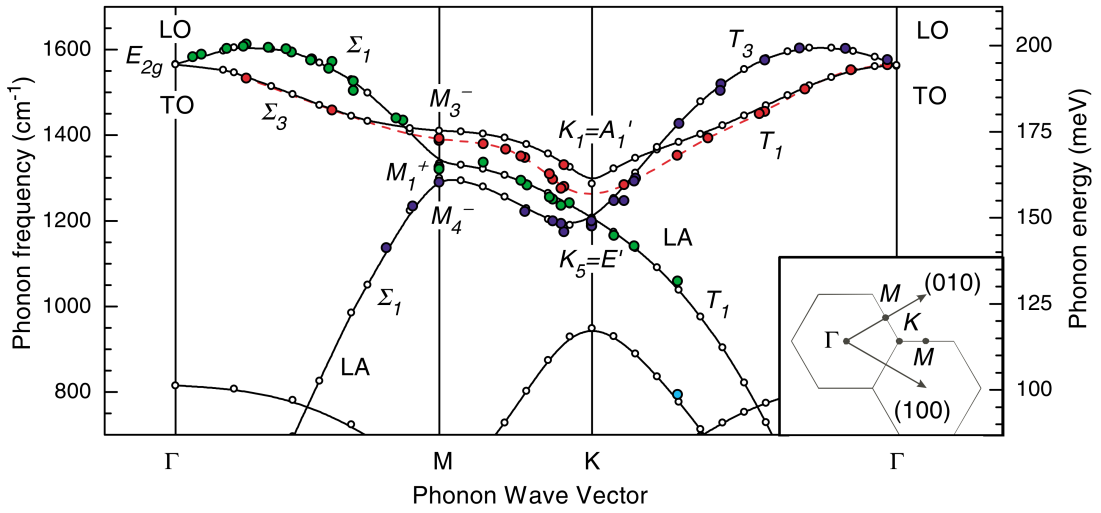

Figure 3.2: Phonon dispersion of graphite. Figure taken from Ref. [47].

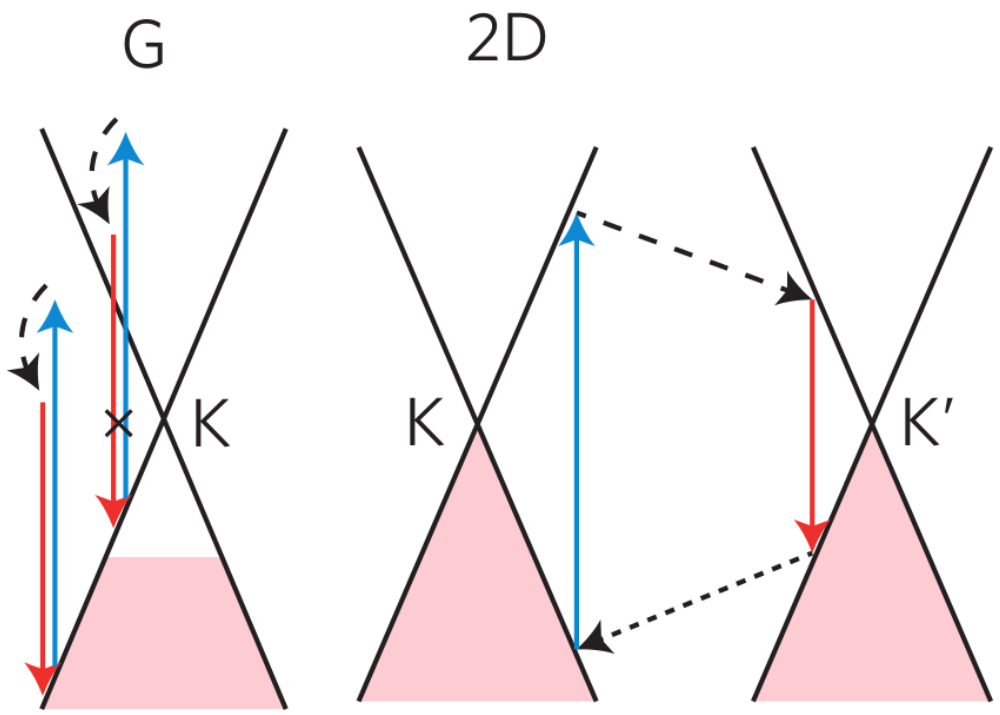

Figure 3.3: Raman scattering pathways for the G mode (left) and the 2D mode (right). Figure taken from Ref. [46].

dispersion are degenerate at the Gamma point and both contribute to the G mode signal[46]. As a first order Raman process involving only one phonon, the G mode peak position is independent of laser energy at 1582 cm^{-1} in undoped graphene. Possible Raman scattering pathways for the G mode are illustrated in the left panel of Fig. 3.3. They unfold as follows: the incoming photon excites an electron to a virtual excited state, the electron relaxes to a lower virtual excited state under emission of a phonon, and the electron relaxes to its initial state under emission of the outgoing photon, whose energy is lower than that of the incoming photon by exactly the phonon energy. All the Raman scattering pathways involve the same Γ point phonon and only vertical electronic transitions, but differ in the initial electronic state. The intensity of the G mode in pristine graphene was shown to be suppressed by a destructive quantum interference effect between this continuum of Raman scattering pathways[4], but the mode is still readily observable experimentally.

The 2D mode originates from a two-phonon Raman process with multiple resonances as shown in the right panel of Fig. 3.3[46,48,49]. Here the incoming photon excites an electron to a real excited state. The electron and hole are then each resonantly scattered into a real electronic state in the other valley (i.e. from the vicinity of K to K′ or vice versa) by a large wavevector phonon, making this a two-phonon process. The electron and hole then recombine under emission of the outgoing photon. All scattering steps are between real electronic states, which

leads to the large intensity of the 2D mode despite its nature as a higher order Raman process than the G mode.

An extraordinary characteristic of the 2D mode is its dispersion with laser energy. A larger laser energy in Fig. 3.3 specifies a resonant transition further from the K point. This in turn leads to a larger phonon wavevector required for the resonant scattering to the other Dirac point, resulting in a larger phonon energy and a shift of the Raman peak in the spectrum.

The G and 2D mode together were used to identify the number of layers in graphene samples[16,46]. Generally a 2D mode that can be fitted with a single Lorentzian component and a stronger intensity than the G mode is accepted as a criterion for single layer graphene.

3.1.3 Kohn Anomaly

A Kohn anomaly occurs when the ability of the conduction electrons in a metal to screen the atomic vibrations changes abruptly and results in a lowering of the phonon energy as well as a discontinuity in the slope of the phonon dispersion[50]. This is possible for phonon wavevectors that connect two points on the Fermi surface. As the Fermi surface of graphene consists of only the K and K′ points, and because K′ = 2K, the only phonon wavevectors that connect points on the Fermi surface are $\boldsymbol{q} = 0$ and $\boldsymbol{q} = \boldsymbol{K}$. The G mode, arising from Γ point phonons, is indeed affected by the Kohn anomaly.

3.1.4 Doping Dependence of the Raman Spectrum

Up to this point I have described the Raman spectrum of pristine graphene. I now discuss what happens at increasing charge carrier concentrations. The G mode frequency was calculated for monolayer graphene in Ref.[51] and is shown here in Fig. 3.4. Upon addition of electrons or holes, first the Kohn anomaly is lifted, resulting in a frequency upshift of about 15 cm^{-1} at about 0.3 eV. This is symmetric for electron and hole doping. At larger charge carrier concentrations, the behavior is dominated by lattice stiffening or weakening due to occupation of anti-bonding orbitals. In contrast to the lifting of the Kohn anomaly this effect has opposite sign for electrons and holes, resulting in a decrease of the phonon frequency for the former and an increase for the latter. In sum, for hole doping the frequency increases monotonically, while for electron doping it increases, reaches a maximum and then decreases.

In addition to the peak position, the linewidth is also affected by doping. At charge neutrality, the phonon can decay into an electron-hole pair excitation between the linear bands crossing at the charge neutrality point. This relaxation channel leads to an increase in the phonon linewidth in pristine graphene. It is blocked by doping when the Fermi energy reaches half the phonon energy, because then the initial of the electron is not occupied for hole doping, or the final state is already occupied for electron doping.

Lastly, doping also affects the intensity of the G mode. The destructive interference that suppresses the G mode intensity at charge neutrality can be blocked

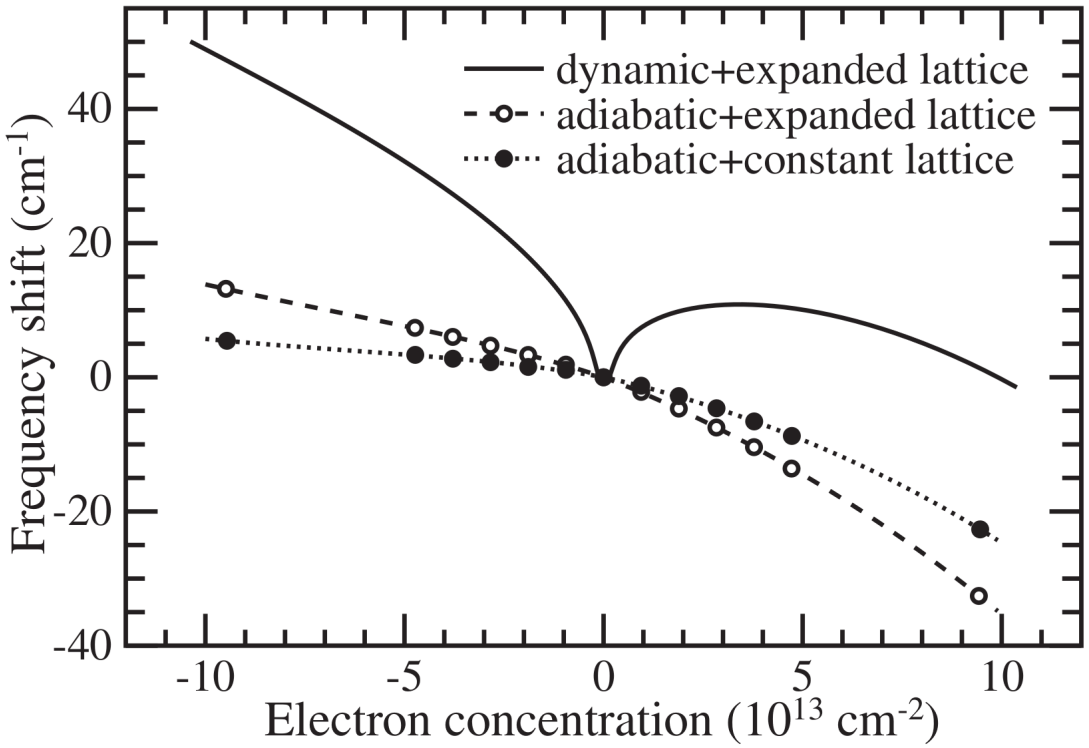

Figure 3.4: G line position as function of charge carrier concentration. 10^{14} charge carriers per square centimeter corresponds to a Fermi energy of about 1 eV. Figure taken from Ref. [51].

by increasing the Fermi energy to half the laser energy[4], resulting in a threefold increase in the intensity. Notice the different Fermi energy scale for this mechanism, which is half the laser energy (e.g. 0.8 eV for 785 nm excitation), compared to that of the Kohn anomaly and the phonon relaxation channel affecting the linewidth. In the latter cases the Fermi energy only has to reach half the phonon energy, about 0.1 eV, to lift he effects.

All of these effects were observed experimentally and studied in detail. In total, the Raman spectrum of graphene was measured for hole doping up to −0.9 eV using electrochemical gating with an electrolyte gel[4]. For electron doping, the G mode was monitored up to a Fermi energy of an estimated 1 eV using rubidium vapor doping, which included the observation of the maximum in the G mode peak position upshift and a subsequent decrease of the peak position.

3.1.5 Fano Peak

A Fano peak occurs in the Raman spectrum if there is a competition between a discrete scattering pathway and a continuum of scattering pathways. One example of this is the competition between a phonon Raman process and a continuum of electronic Raman processes as observed in p-doped Si[52]. The Raman intensity of such a Fano peak with the phonon frequency ω_0, peak broadening Γ and

asymmetry parameter q can be calculated according to[53]

$$I(\omega) = I_0 \cdot \frac{\left(1 + \frac{\omega-\omega_0}{q\Gamma/2}\right)^2}{1 + \left(\frac{\omega-\omega_0}{\Gamma/2}\right)^2}, \tag{3.5}$$

where I_0 is the intensity of the peak. The smaller the value of q, the larger the asymmetry of the peak. For large values of q, the Fano lineshape approaches that of a Lorentzian. Negative q values lead to increased intensity at lower frequencies and positive q values give increased intensity at higher frequencies. Fano peaks were also observed in the Raman response of graphite intercalation compounds, which I will introduce in the next section.

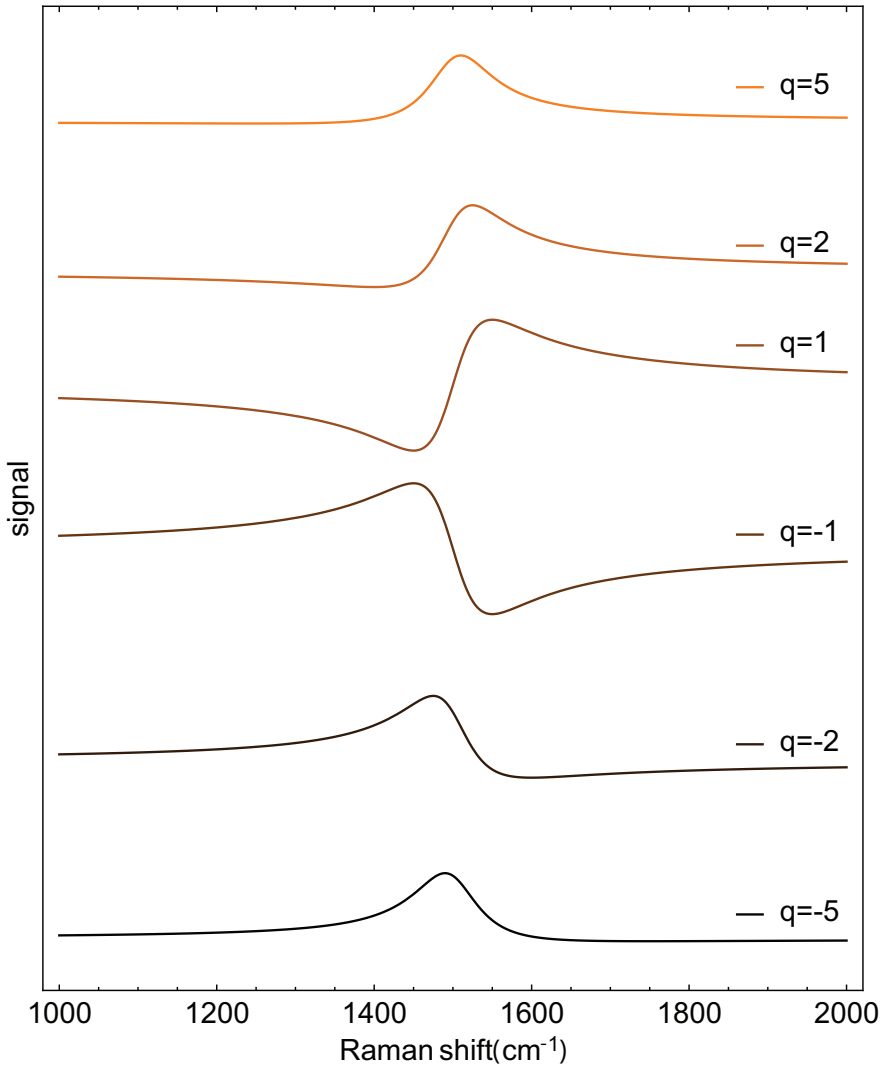

Figure 3.5: Raman lineshapes calculated according to formula 3.5 for asymmetry parameters ranging from −5 to 5, with a width Γ of 50 cm^{-1} and the phonon frequency ω_0 = 1500 cm^{-1}.

3.1.6 Graphite Intercalation Compounds

Graphite intercalation compounds consist of graphite layers with an intercalant atomic or molecular species in between. Common intercalants are the alkali metals Li, K[54–56], and Rb[57] as well as Ca[58,59] and other alkaline earth metals[60]. These produce electron doping of the graphene layers. $FeCl_3$ can be used as an intercalant for hole doping. Graphite intercalation compounds were extensively studied using Raman spectroscopy, and also attracted attention because of superconductivity observed e.g. in CaC_6 with a transition temperature of 11.5 K[8].

Graphite intercalation compounds are commonly labeled by their stoichiometric composition such as KC_8, which contains one potassium atom for every eight carbon atoms, KC_{24}, KC_{36}, KC_{72}, etc. Alternatively the compounds mentioned above are also referred to as stage 1, 2, 3, and 4. Here a lower stage number indicates fewer carbon atoms per potassium atom and higher doping.

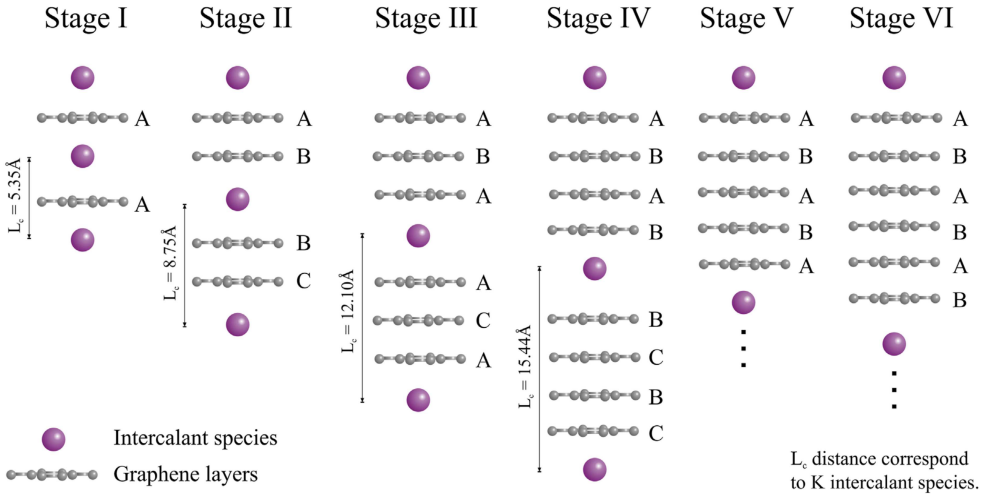

Figure 3.6: Arrangement of potassium atoms between the graphene layers of graphite intercalation compounds from Stages I to VI. Figure taken from Ref. [61].

The stages mentioned above differ not just in the ratio of potassium to carbon atoms. The arrangement of the potassium atoms in the graphite crystal is also markedly different between them, as shown in Fig. 3.6. In stage 1 graphite intercalation compounds, the intercalant is between each graphene sheet. This results in a uniform doping for every graphene sheet. In stage 2 compounds, there are two graphene layers between every intercalant layer. The doping is again uniform, but lower than for stage 1. In stage 3 compounds, there are three graphene layers between every intercalant layer. This results in two outer layers that have strong charge transfer from the intercalant, and one inner layer with much lower doping. Analogously, in stage 4 compounds there are four graphene layers between every intercalant layer, etc.

The stage number and the resulting doping has a critical influence on the Raman behavior of graphite intercalation compounds. I will discuss this using the example of potassium graphite intercalation compounds[25]. For KC_8, the Raman spectrum (shown in the left panel of Fig. 3.7) exhibits a very broad and

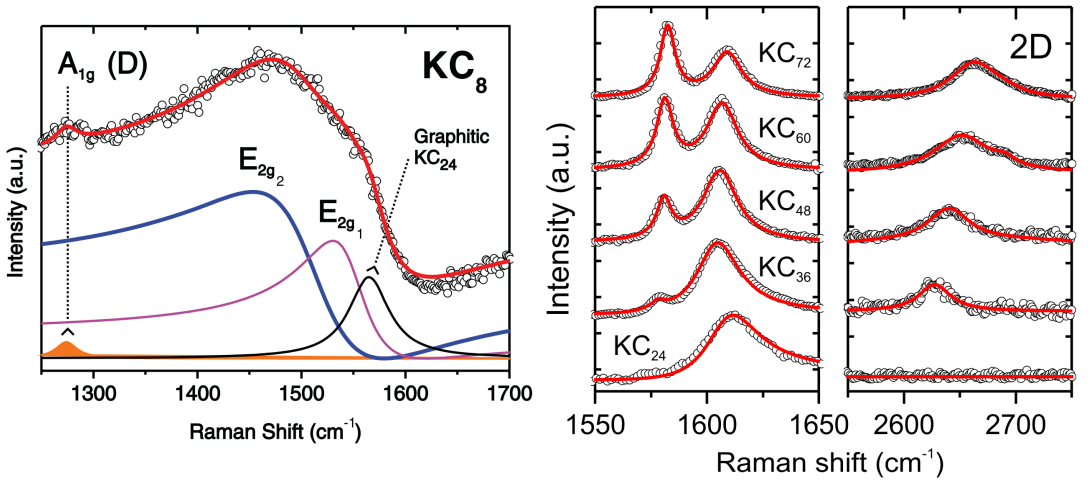

Figure 3.7: Raman response of graphite intercalation compounds from KC_8 to KC_{72} excited with 568 nm. Figure combined from Ref. [61,62].

strongly asymmetric Fano peak at 1510 cm^{-1} [54,56,62] with a width of 125 cm^{-1} and an asymmetry parameter of −1.1 [62]. This Raman peak is attributed to the same phonon as the G mode in pristine graphite, i.e. the Γ point E_{2g} modes of the LO and TO branch. The large downshift, as well as the broadening, are also observed in Rb and Cs [57] intercalation compounds and are thought to be due to non-adiabatic corrections to the phonon frequency arising from electron-phonon interactions [63]. The spectrum in Fig. 3.7 shows an additional E_{2g} component at 1547 cm^{-1} and a peak attributed to residual KC_{24} at 1565 cm^{-1} [62]. The Fermi energy in KC_8 was measured to be 1.35 eV using angle-resolved photoelectron spectroscopy (ARPES) [26].

For KC_{24}, the doping is still the same for every layer, so that there is only G mode peak. However, it is located at 1610 cm^{-1} [25], thus resembling the up-shifted G mode in graphene under doping. For KC_{36} and higher stages, there are two peaks in the G mode region, one from the graphene layers adjacent to the potassium layers and one from the less-doped inner layers. The G mode from the inner layers increases in relative intensity with increasing stage number, as there are more inner layers. The peak from the layers adjacent to the potassium layers decreases in relative intensity and also downshifts in frequency with increasing layer numbers.

The 2D peak is not observable in KC_8 and KC_{24} because the double-resonant Raman process is blocked [25]. From KC_{36} to KC_{72} the 2D mode is present in the spectrum and increases in frequency with increasing stage number.

3.1.7 Expectations for potassium-doped Graphene

As a consequence of the behavior discussed in the preceding sections on the doping dependence of the Raman spectrum of graphene and the Raman spectrum of potassium graphite intercalation compounds, there are two conflicting predictions for the Raman spectrum of potassium-doped graphene:

- A continuation of the behavior of doped graphene, meaning a decrease in the Raman peak position after its maximum at around 1 eV. This could conceivably lead to peak positions of between 1600 cm^{-1} and 1580 cm^{-1}. In this picture there would be no peak broadening or asymmetry at high doping strengths.

- A Raman spectrum similar to that of stage one potassium graphite intercalation compounds, where there is one layer of potassium ions for every graphene layer. If the potassium atoms arrange themselves only on top of the graphene layer, this would lead to an equivalent doping strength as in stage one potassium graphite intercalation compounds. If the potassium atoms additionally penetrate the space between the substrate and the graphene layer, this could lead to even stronger doping strengths. In this picture I would expect a broad and asymmetric peak at much lower peak position than in the other picture, as the peak in stage one potassium graphite intercalation compounds is located at 1510 cm^{-1}.

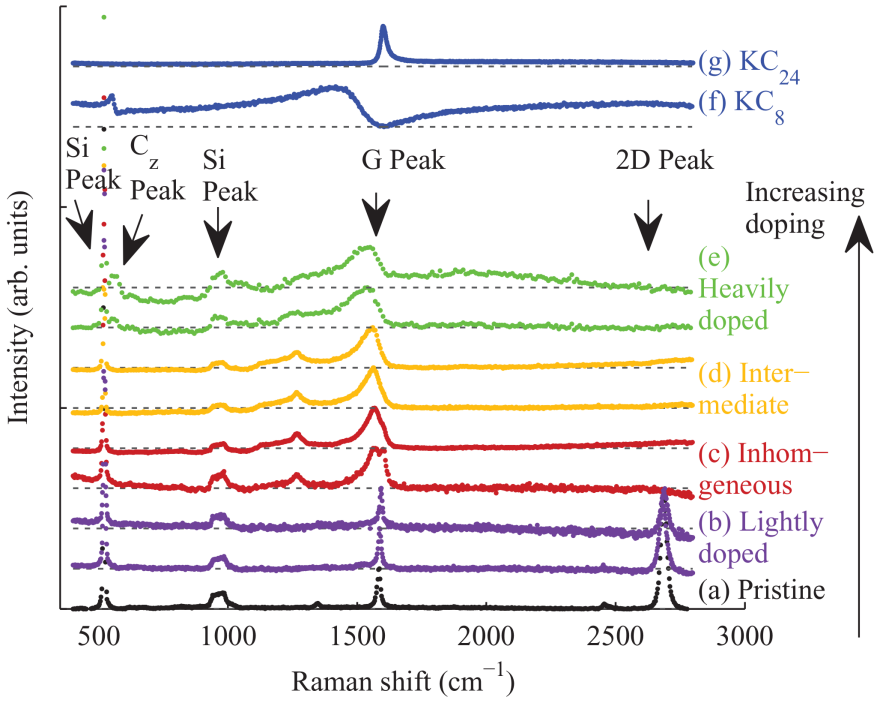

Figure 3.8: Raman spectra of potassium-doped graphene with increasing doping time, KC_8, and KC_{24} measured at 514 nm. The spectrum of heavily doped graphene exhibits a broad and asymmetric peak at lower frequencies than the pristine G mode. Figure taken from Ref. [6].

The Raman spectrum of potassium doped graphene was indeed measured in Ref.[6] and is shown here in Fig.3.8. It exhibits an asymmetric peak, whose position and linewidth vary with intercalation time. However the position is in all cases higher and the linewidth narrower than that in stage one potassium graphite intercalation compounds. It is equally clear that the behavior in Ref.[6] is not a continuation of the doping dependence of graphene, as the peak is much

too broad and asymmetric. Unfortunately the authors of Ref.[6] measure the Raman spectrum only at a single laser wavelength of 514 nm.

3.1.8 Summary

In summary, I have discussed the theoretical background of the Raman spectrum of graphene and its doping dependence, the Raman spectrum of graphite intercalation compounds as well as the first reported Raman measurements of potassium-doped graphene. I also detailed a formalism for calculation of the reflectivity of layered systems as well as its application to graphene on Si/SiO_2. This chapter should serve as a broad enough basis for the understanding of the reflectivity and Raman spectra of potassium-doped graphene that are reported in this thesis.

3.2 Experimental Methods

3.2.1 Raman Spectrometers

To investigate the Raman spectrum of potassium-doped graphene over a wide range of laser energies, a number of different Raman spectrometers were used:

- A Witec alpha300 R spectrometer using 532 nm laser excitation wavelength and a single grating monochromator with a 600 lines/mm grating. This setup uses an edge filter to block Rayleigh-scattered light and offers excellent sensitivity as well as a piezo-motorized stage for the acquisition of Raman maps.

- A Horiba XploRA spectrometer with 638 nm and 785 nm laser lines. This spectrometer shares the characteristics of the Witec spectrometer described above, but also has 1200 and 1800 lines/mm gratings.

- A Dilor XY spectrometer with an argon-krypton laser, offering a discrete set of laser lines from 458 nm to 647 nm. The Dilor uses a triple grating monochromator with 1800 lines/mm gratings. Its sensitivity is much lower than that of the single-grating setups.

- A Horiba T6400 spectrometer. This setup is paired in our lab with a dye laser and titanium sapphire laser, the latter of which can also be frequency-doubled. I have used the frequency-doubled titanium sapphire laser at laser wavelengths of 425 nm and 381 nm. The T64000 can be operated in single or triple grating monochromator mode, but I have measured only with a single 900 lines/mm grating and an edge filter to block Rayleigh-scattered light.

- A Horiba LabRam spectrometer paired with a helium-cadmium laser with 325nm wavelength. This is another single grating setup with an edge filter and a 600 lines/mm grating. The UV laser wavelength necessitates the use of a 40× magnification UV objective that was only used at this wavelength.

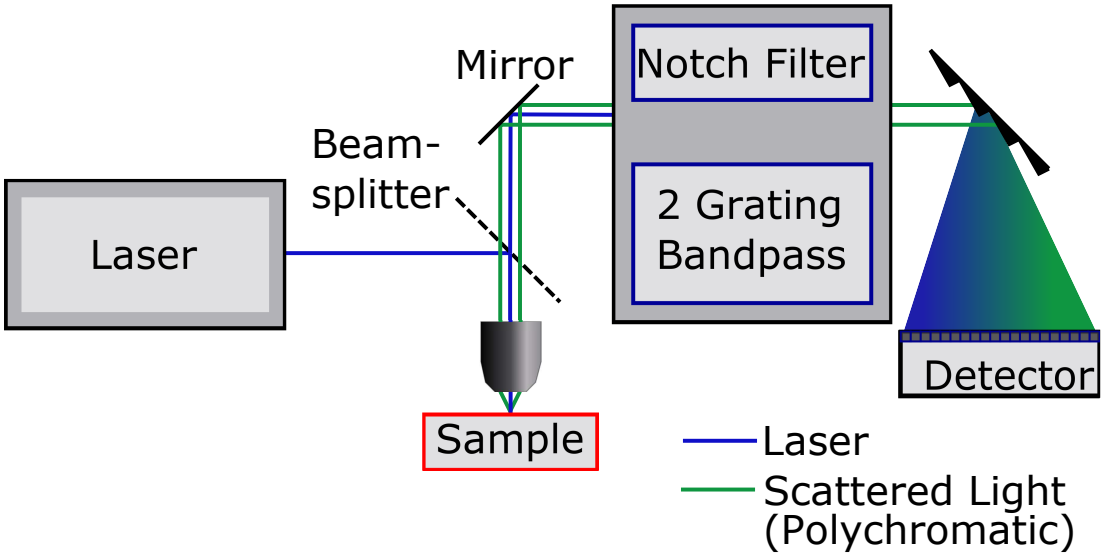

Figure 3.9: Experimental setup for Raman spectroscopy in a backscattering configuration with a notch filter or a double grating monochromator to suppress the Rayleigh-scattered light. Adapted from Ref. [64].

Spectra at all wavelengths in the visible and near-infrared were calibrated in frequency using a neon lamp. In the UV, where there are no neon lines, the Raman peaks of diamond or silicon were used instead. To measure the Raman signal of the doped graphene inside the ampoule, a 50x objective is used. This objective offers the necessary working distance to focus on the sample through the glass wall of the ampoule, as well as a good magnification to locate the graphene flake, and a small enough laser spot size to ensure I am measuring only from the desired area.

3.2.2 Polarization-dependent Raman Measurements

When measuring polarization-dependent Raman spectra at a given wavelength, I want to acquire spectra with linearly polarized light where incoming and outgoing light are polarized along the same axis (linear parallel) and along perpendicular directions (linear perpendicular), as well as with circularly polarized light where the polarization of incoming and outgoing light is rotating in the same direction (circular corotating) and in opposite directions (circular contrarotating). I want to realize these scattering configurations without removing or inserting any elements in the optical path. I employ the linear polarization of our laser, a $\lambda/4$ plate between the beam splitter and the objective lens, and an analyzer with a $\lambda/2$ plate in front of it. The analyzer is placed just in front of the spectrometer entrance and aligned to transmit light of the laser polarization. For linear parallel and perpendicular scattering, I align the $\lambda/4$ plate to 0° with respect to the laser polarization. Turning the $\lambda/2$ plate in front of the analyzer then switches between linear parallel (0°) and linear perpendicular scattering (45°).

For circular corotating and contrarotating scattering configurations, I turn the $\lambda/4$ plate in front of the objective lens to 45°. The light hitting the sample then has

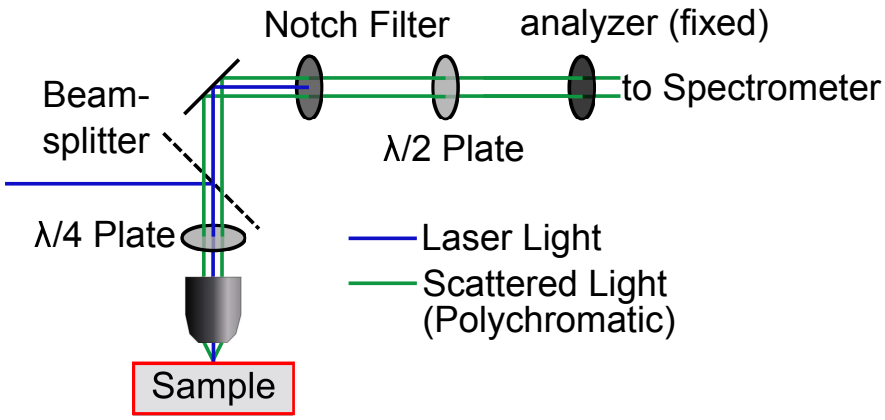

Figure 3.10: Experimental setup for polarization-dependent Raman spectroscopy. The $\lambda/4$ between beam splitter and objective is turned between 0° and 45° for linear and circular polarized incoming light. The $\lambda/2$ plate in front of the fixed analyzer is set to 0° for linear parallel and circular corotating configurations, and 45° for linear perpendicular and circular contrarotating configurations.

Table 3.1: Experimental settings for polarization-dependent Raman scattering. The $\lambda/4$ plate is placed in front of the objective lens. The $\lambda/2$ is placed in front of the analyzer, which I keep fixed.

		$\lambda/4$ plate	$\lambda/2$ plate
linear	parallel	0°	0°
	perpendicular	0°	45°
circular	corotating	45°	0°
	contrarotating	45°	45°

circular polarization. The scattered light can have corotating and contrarotating circular polarization. Upon passing through the $\lambda/4$ plate again on the way to the spectrometer entrance, the corotating component is converted to linearly polarized light with the same polarization as the laser, whereas the contrarotating component is converted to linearly polarized light with polarization perpendicular to that of the laser. I can thus again select between the two components by turning the $\lambda/2$ plate in front of the analyzer between 0° for corotating scattering and 45° for contrarotating scattering.

The beam splitter in the Dilor setup has a polarization-dependent transmission coefficient. To correct for this, I take the spectrum of a 111 face of a silicon crystal in linear parallel and perpendicular scattering configurations. The intensity ratio between perpendicular and parallel scattering (depolarization ratio) should be 2/3. This ratio is not observed in practice, but I find a correction factor by which I multiply the intensities in perpendicular and contrarotating scattering in subsequent experiments.

3.2.3 Summary

Summarizing the description of my experimental methods, I have listed the preparation method for potassium-doped graphene in a sealed evacuated ampoule, as well as an array of optical spectrometers. These will allow me to measure the Raman spectra of the samples over an extremely broad energy range and with polarization control, as well as their reflectivity.

3.3 Results

3.3.1 Evolution of the Raman Spectrum under Potassium Exposure

In this section I present and discuss the evolution of the Raman spectrum of graphene during the first hours of exposure to potassium vapor in a two zone vapor intercalation experiment. The experimental details are as described in Section 2.2.1 and all measurements are with 532 nm laser excitation. The initial Raman spectrum, before I turned on the heating, shows the G and 2D modes as expected for pristine graphene. The G mode peak is located at 1587 cm^{-1}. It can be fitted well with a single Lorentzian peak. The 2D peak is located at 2462 cm^{-1}. It too can be fitted with a single Lorentzian, as is expected for single layer graphene. The intensity ratio between the G and 2D peak is $I_G/I_{2D} = 0.4$.

From the moment the heating is turned on, the graphene is exposed to potassium vapor. The evolution of the Raman spectrum is shown in Fig. 3.11 and can be summarized in three phases:

- The G peak upshifts in position, to about 1600 cm^{-1}. Its full width at half maximum remains constant at 20 cm^{-1}, as does its intensity. The 2D peak downshifts in position and its intensity decreases.

- A new peak arises at lower frequencies than the G mode and increases in intensity. At the same time, a strong background signal also appears. The G mode increases further in frequency, but much more slowly than before, up to a position of 1605 cm^{-1}. The 2D mode disappears completely.

- The G peak then also decreases in intensity until it disappears, leaving only the new peak at lower frequencies. This last phase takes much longer than the other two to complete.

This constitutes the final state Raman spectrum. Further heating no longer leads to any changes in the Raman response. The single peak is downshifted in frequency from the original position of the G peak. It is located at 1560cm^{-1} and has a linewidth of 61cm^{-1}, much larger than the pristine G peak. Furthermore, the peak is asymmetric. It exhibits higher intensity at lower frequencies, corresponding to an asymmetry parameter of about $1/q = -6$.

I summarize the evolution of the G peak position in Fig. 3.12. The evolution of the G peak under exposure to Potassium vapor as shown in this graph

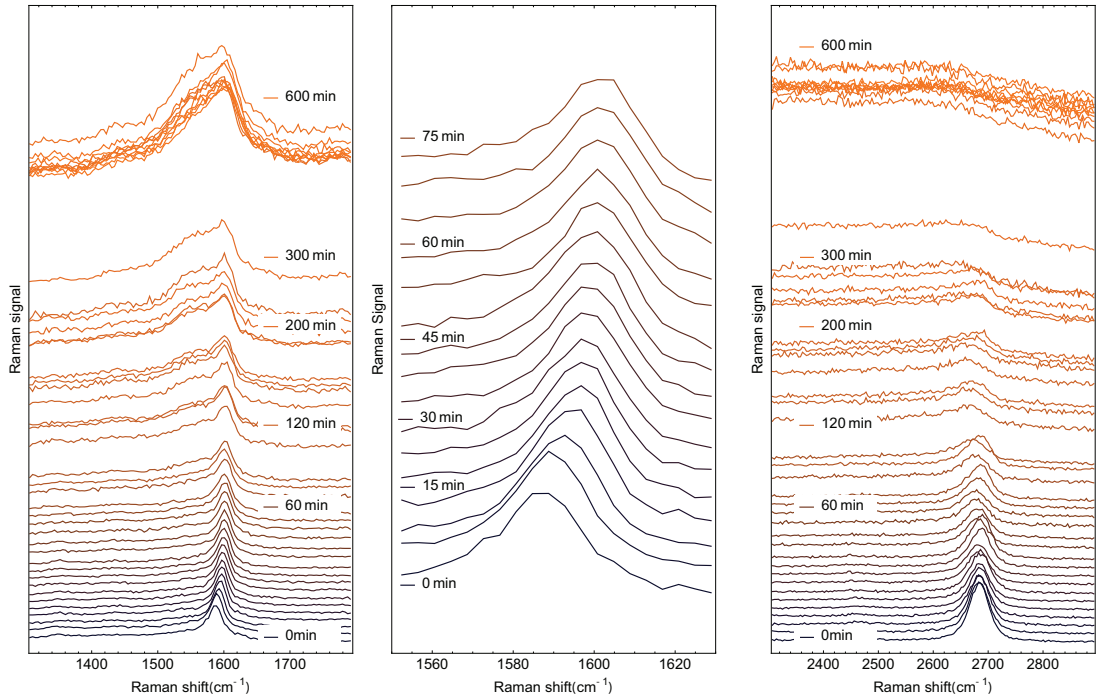

Figure 3.11: Time evolution of the Raman signal of graphene (532 nm excitation) under exposure to potassium vapor. The G mode (left and middle panel) first rapidly increases in frequency (best seen in the middle panel). At later times an additional peak arises in the spectrum. The 2D mode (right) decreases in intensity and disappears completely from the spectrum.

can be compared to Ref. [7]. Whereas their observations are initially in line with my results, they do not see the appearance of the peak at 1560cm^{-1} that arises in strongly doped graphene with potassium, or the disappearance of the G peak. This might be due to their lower intercalation time, or the difference in intercalant species of potassium versus rubidium. I now proceed by comparing the experimental results from electron doping by potassium evaporation to those from hole doping by electrochemical gating, as well as to a theoretical calculation from Ref. [51].

The disappearance of the 2D mode can be explained by considering the Raman process in Fig. 3.3. The transition involving the outgoing photon is blocked when the Fermi energy reaches half of the outgoing photon energy, which is 2eV at a laser wavelength of 532nm(2.33eV). The disappearance of the 2D mode thus indicates a Fermi energy of more than 1eV.

3.3.2 Comparison of Potassium Doping and Electrolyte Gel Gating

Electrochemical gating is a technique for doping graphene that works through the formation of an electric Debye layer at the interface of graphene and an electrolyte. This Debye layer acts a capacitor with a plate distance on the order of a few nanometers, far smaller than for electrostatic gating through an e.g.

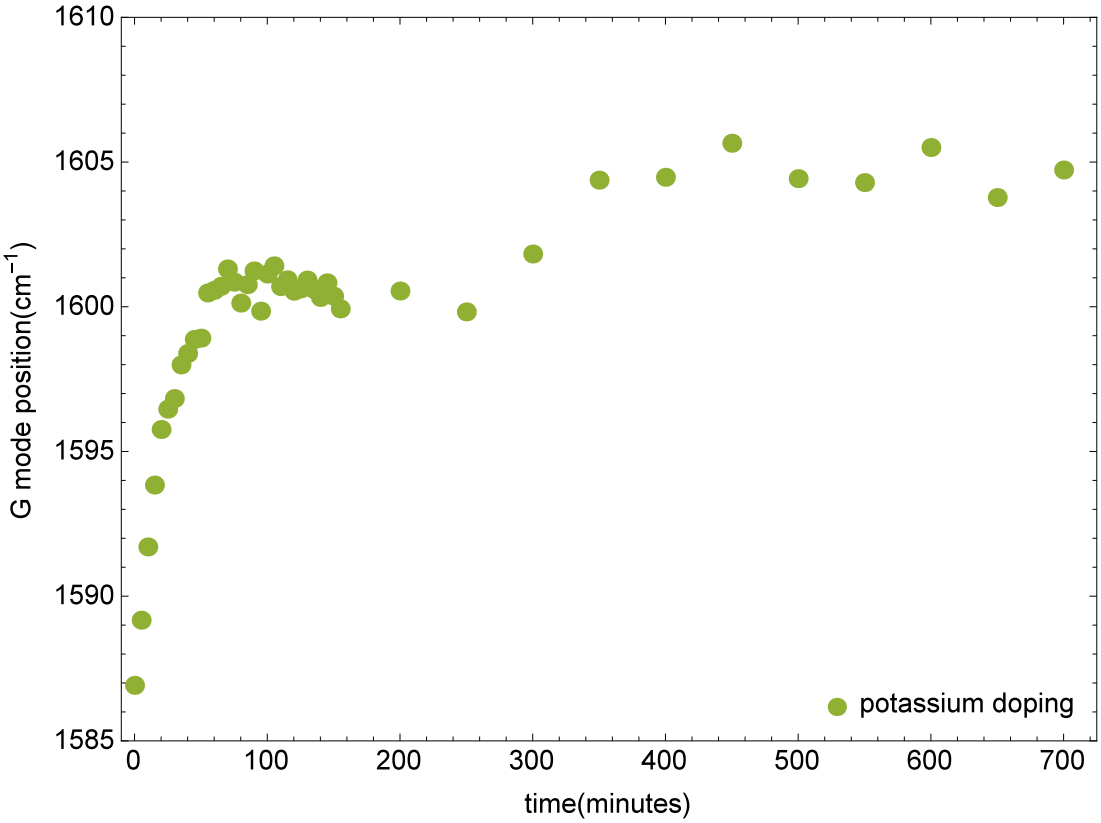

Figure 3.12: G mode peak position of graphene under exposure to potassium vapor. The peak first upshifts rapidly by about 15cm^{-1} and subsequently only increases at a slower rate.

300 nm thick SiO_2 layer. The doping levels achievable in electrochemical gating thus far exceed those in electrostatic gating, with the maximum doping level depending on the electrolyte. Using an electrolyte gel consisting of a mixture of a polymer and an ionic liquid, I am able to achieve doping levels of about 0.8 eV, as also reported in the literature[4,23].

In this section I compare the behavior of electrochemically doped graphene under hole doping as a function of gate voltage to that of potassium-doped graphene (which is electron-doped) as a function of potassium evaporation time. I show the Raman spectra under electrochemical gate voltages ranging from 0 to −2.3 V, acquired with 785 nm excitation, in Fig. 3.13. For the G mode, shown in the left panel, I observe a monotonous increase in the peak frequency. Additionally, there is a strong increase in the peak intensity at high gate voltages, followed by a subsequent decline. There is no indication of the broad and downshifted peak I observe for potassium-doping. Concerning the 2D mode, I see a strong decrease in the peak intensity until it is no longer visible. Up to the disappearance, the peak position remains constant at 2600 cm^{-1}.

I plot the position and peak area of the G mode as a function of gate voltage in Fig. 3.14 and Fig. 3.15. I now want to compare the peak position to theoretical calculations by Lazzeri et al.[51]. For this purpose it is necessary to convert the gate voltage to Fermi energy. To achieve this I make use of the observation of

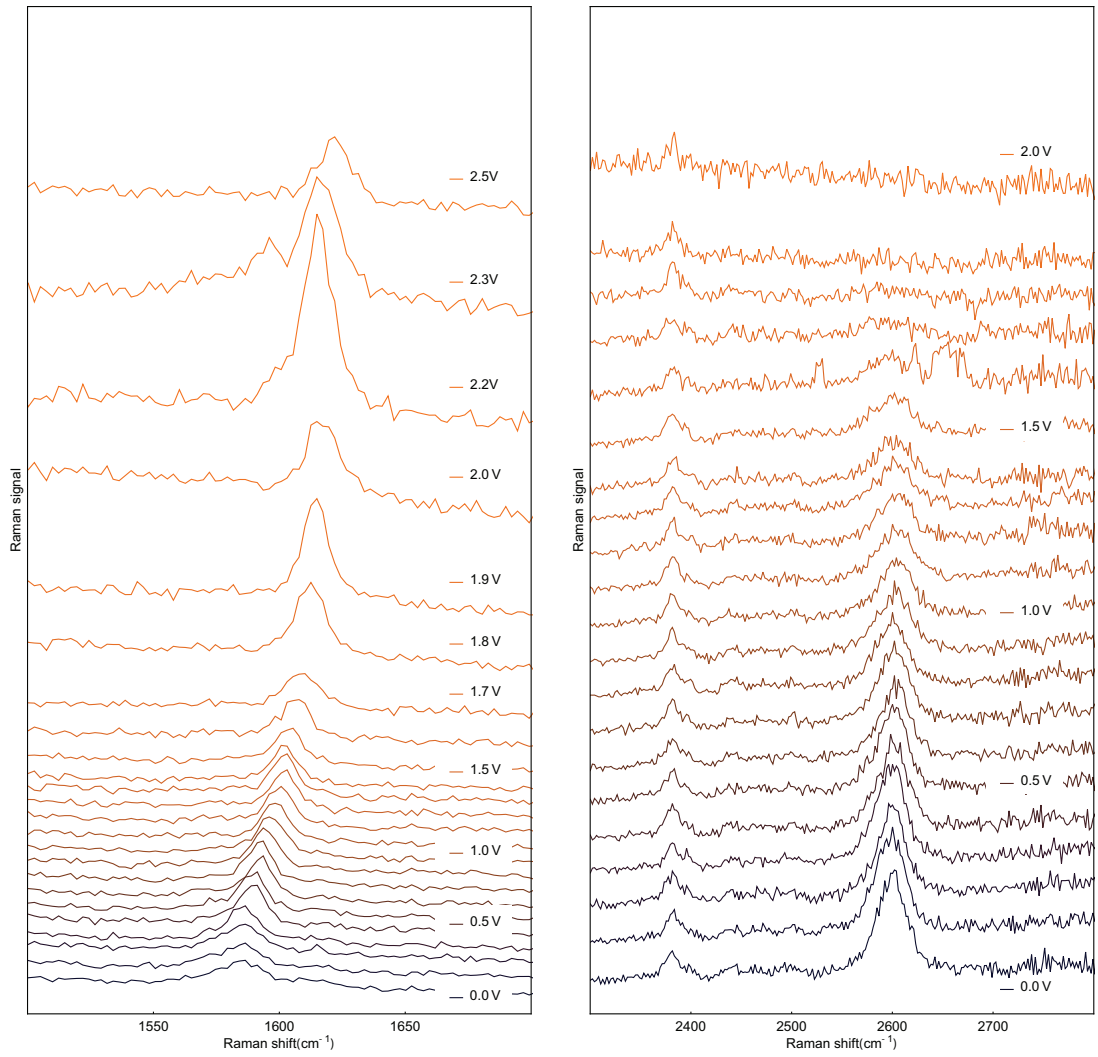

Figure 3.13: G mode Raman spectrum in electrochemically doped monolayer graphene at 785 nm excitation as a function of negative gate voltage, corresponding to hole doping. The G peak upshifts in frequency and increases in intensity at large gate voltages. The 2D peak decreases in intensity and eventually disappears.

the increase in the G peak area at −2.1 V. This increase in the G peak area has been predicted to occur at $2E_F = E_L - \hbar\omega/2$, where E_L and $\hbar\omega$ refer to laser and phonon energies[4]. For my measurement this means that a gate voltage of −2.1 V corresponds to a Fermi energy of

$$\frac{E_L - \hbar\omega/2}{2} = \frac{1.58\ \text{eV} - 0.10\ \text{eV}}{2} = 0.74\ \text{eV}. \tag{3.6}$$

Assuming a linear increase of the Fermi energy with gate voltage $2V_G$, I thus find that $E_F = 0.35\ V_G$ and am able to plot the peak position as function of Fermi energy, or the charge carrier concentration $n = E_F^2/\pi(\hbar v_F)^2$ in Fig. 3.16 (negative charge carrier densities). Also shown in the figure is the theoretical calculation from Ref. [51], with non-adiabatic effects included. I have used the calculation for a static lattice because the graphene is in contact with the a substrate in mymea-

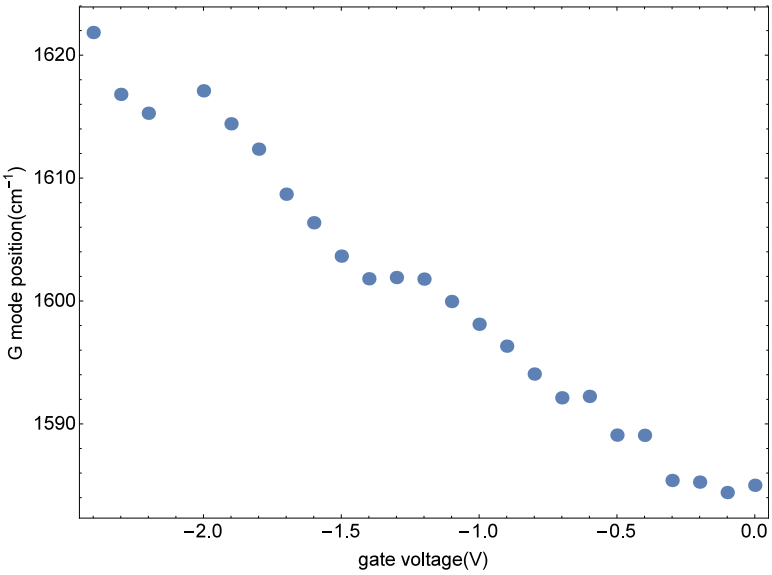

Figure 3.14: Peak position of the G mode in electrochemically doped monolayer graphene as a function of gate voltage. The peak position increases approximately linearly for larger negative gate voltages.

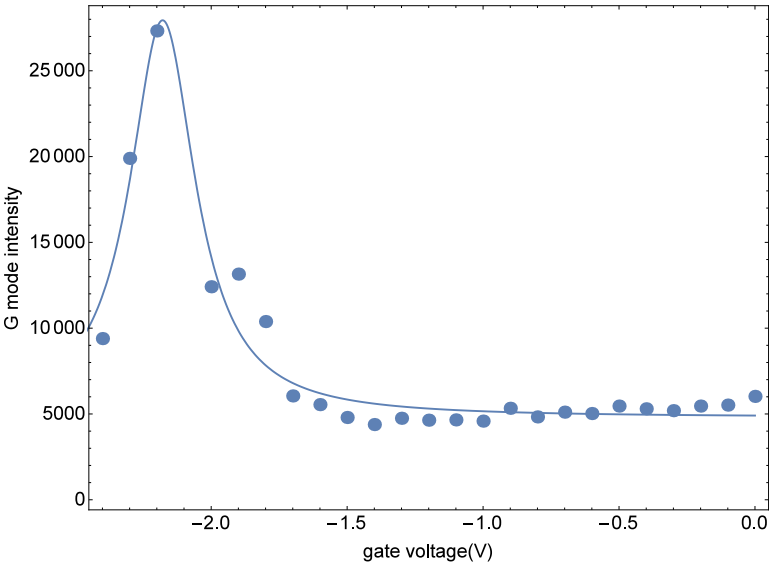

Figure 3.15: Peak area of the G mode in electrochemically doped monolayer graphene as a function of gate voltage. With increasing negative gate voltage, the area first stays constant up to −1.5 V but then exhibits a peak at −2.2 V.

surements. Furthermore I have rescaled the calculation from Ref. [51] to use the electron phonon coupling strength $\langle D_{\Gamma}^2 \rangle_{\mathrm{F}} = 62.8$ eV^2/Å^2 from Ref. [65]. This value, calculated using the GW density functional theory method, is supposed to be more accurate than the value of 45.6 eV^2/Å^2 used in Ref. [51]. I obtain excellent agreement between theory and experiment and observe a maximum G mode shift of 37 cm^{-1} at a charge carrier density of -4.3×10^{13} cm^{-2}, corresponding to a Fermi energy of −0.84 eV.

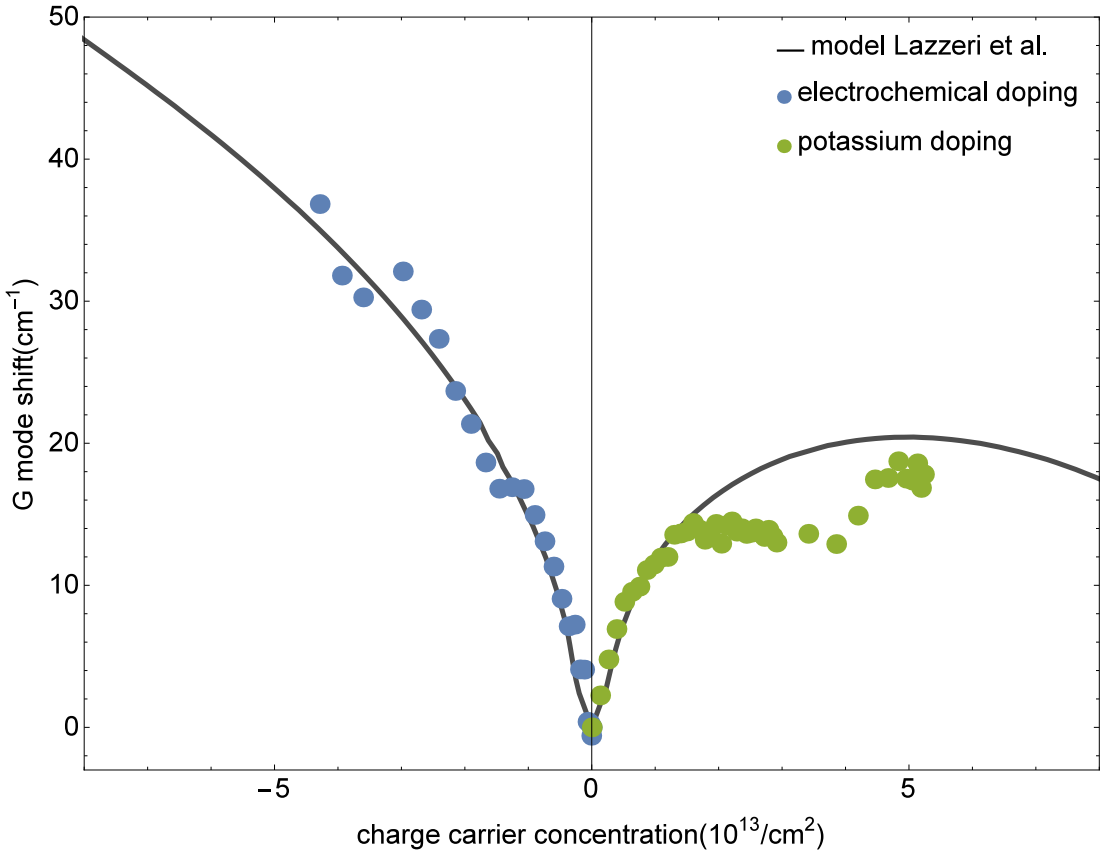

Figure 3.16: Peak position of the G mode under electrochemical gating (negative charge carrier densities) and exposure to potassium vapor (positive charge carrier densities) compared to a calculation from Ref. [51].

Similarly, to compare the peak positions observed under potassium doping to the theoretical calculations, I need to convert the exposure time to charge carrier density. Here I rely on the approach demonstrated by Parret et al. in Ref. [7], who use the following function to model the charge carrier concentration as a function of doping time:

$$n(t) = n_{\mathrm{f}}(1 - e^{-t/t_0}), \tag{3.7}$$

where n_{f} indicates the final charge carrier concentration and t_0 sets the doping timescale. I use this formula to fit my results to the calculation outlined above (non-adiabatic effects included, static lattice, electron phonon coupling from GW) for positive charge carrier densities and obtain values of $n_{\mathrm{f}}) = 5.4\times10^{13}$ cm^{-2} and $t_0 = 200$ minutes. While the data are described well by Eq. 3.7 up to charge carrier

densities of 2×10^{13} cm^{-2}, I then observe a plateau in the G mode frequency before it increases again after 4×10^{13} cm^{-2}. I do not observe a downshift of the G mode at larger charge carrier densities. For longer doping times, the G mode remains constant in frequency but decreases in intensity and eventually disappears, leaving only the lower-frequency Fano peak.

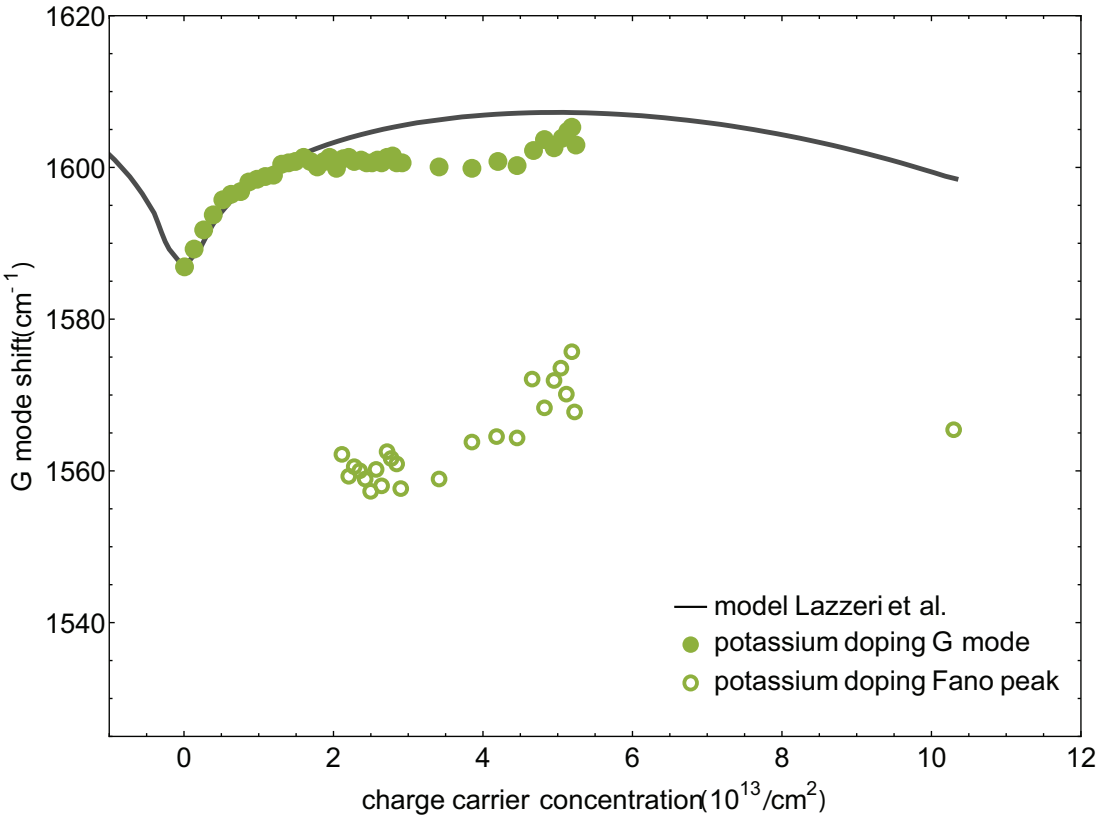

Figure 3.17: Peak position of the G mode and the Fano peak under exposure to potassium vapor (positive charge carrier densities) compared to a calculation from Ref. [51].

To verify my Fermi energy calibration, I perform an analysis of the 2D mode intensity as a function of Fermi energy. I fit the 2D mode in the spectra shown in Fig. 3.11 and again convert the potassium evaporation time to Fermi energy using equation 3.7. I compare my data to that of Ref.[4], where the Fermi energy was determined from infrared transmission measurements, in Fig. 3.18. As can be seen, my data is in agreement, which indicates that my Fermi energy calibration is accurate.

I now use the conversion of doping time to charge carrier density to quantify the behavior of the lower-frequency Fano peak and in particular to investigate if the Fano peak appears at doping strengths that are also achievable by electrochemical gating. For this purpose I plot its peak position alongside that of the G mode in Fig. 3.17. The final data point is observed after several days of potassium doping, after which the G mode is completely absent from the spectrum. The electron concentration for this data point was determined from the reflectivity in Sec. 2.3.2. The first spectrum where the Fano peak is clearly observable is after 100 minutes. After 250 minutes, the peak is roughly similar in amplitude to the

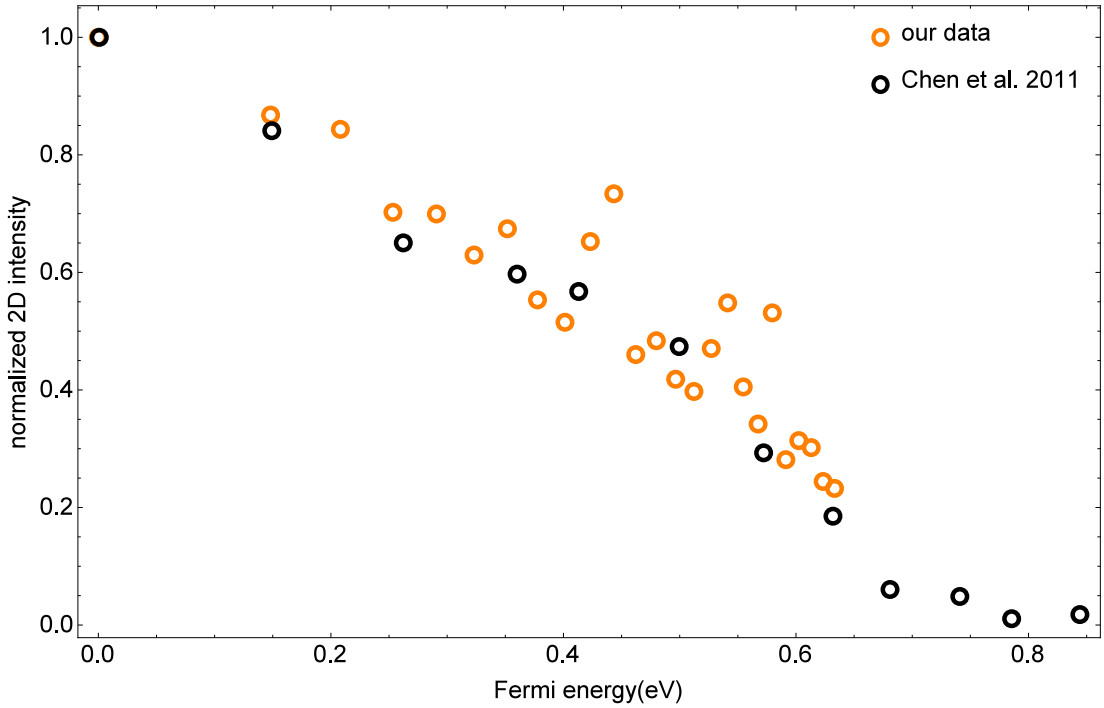

Figure 3.18: Integrated 2D intensity as a function of Fermi energy from my measurements under potassium evaporation (orange) compared to data from Ref. [4].

G mode. This corresponds to a charge carrier density of $3.8{\times}10^{13}$ cm^{-2}, which is lower than the maximum charge density that I obtain using electrochemical gating.

It thus appears that the Fano peak only appears for electron doping but not hole doping. This is supported by the fact that it was also not observed in $FeCl_3$ intercalated few-layer graphene in Ref. [66]. However it is also clear that realizing a high electron concentration is necessary but not sufficient to observe the Fano peak because it was not seen in the rubidium doping experiments in Ref. [7]. I also note that the theoretical calculation of Lazzeri et al.[51], even at the highest electron density when the peak position decreases again, does not come close to giving a frequency value that would be in line with my observation of the Fano peak position. The difference is more than 30 cm^{-1}.

Summarizing the two preceding sections, I have investigated the G mode peak position in doped graphene over an extraordinarily broad doping range encompassing both hole and electron doping. Although I had to resort to different methods for electron and hole doping, the measurements were performed on graphene samples from the same production batch and compared to the same calculation. For hole doping using electrochemical gating, the G mode upshifts continuously with no sign of a saturation and I obtain excellent quantitative agreement with the calculation over the full doping range. For electron doping using potassium evaporation, the G mode increases in position similarly rapidly as for hole doping at low charge carrier concentrations but then slows down, reaches a plateau in frequency, and decreases in intensity. I find decent overall agreement with the calculation in terms of the absolute maximum peak position shift as well as the

Table 3.2: Fit parameters for the Fano peak in potassium-doped monolayer graphene as a function of laser wavelength.

λ(nm)	E_L(eV)	ω_0(cm^{-1})	Γ(cm^{-1})	$1/q$
785	1.58	1539	45	−8.2
638	1.94	1556	47	−5.2
593	2.09	1561	51	−4.9
568	2.18	1563	64	−5.0
532	2.33	1565	61	−5.8
514	2.41	1569	65	−4.4
487	2.55	1566	80	−4.3
425	2.92	1576	81	−2.3
381	3.25	1584	75	−2.7
325	3.82	1604	35	−5.7

weaker upshift at higher charge densities. For hole doping the G mode eventually disappears from the spectrum at long doping times. An investigation of the remaining asymmetric Fano peak will be the focus of the rest of this chapter.

3.3.3 Excitation Energy Dependence of the Raman Spectrum

Having described the time evolution of Raman signal of monolayer graphene under exposure to potassium vapor, I now further characterize the Raman response of the fully doped graphene (Fermi energy of 1.3 eV) by using a broad range of laser excitation wavelengths. The strongest Raman peak between 1500 and 1600 cm^{-1} is fitted with a Fano peak according to:

$$I(\omega) = I_0 \cdot \frac{\left(1 + \frac{\omega-\omega_0}{q\Gamma/2}\right)^2}{1 + \left(\frac{\omega-\omega_0}{\Gamma/2}\right)^2}, \tag{3.8}$$

where ω_0 denotes the peak position (not the spectral position of maximum intensity), Γ is the peak broadening, and q is the asymmetry parameter. In this section I examine all three of these parameters.

Figure 3.19 shows Raman spectra excited with laser wavelengths from 785 nm to 325 nm, corresponding to laser energies ranging from 1.58 eV to 3.82 eV. With increasing laser energy, the peak downshifts in position and becomes broader and more asymmetric up to 425 nm. The peak position then continues to increase. However, the width and asymmetry decrease for 381 nm excitation and, more drastically, at 325 nm. The fit parameters are listed in Table 3.2. As an example, the fitted spectrum acquired at 593 nm is shown in Fig. 3.20.

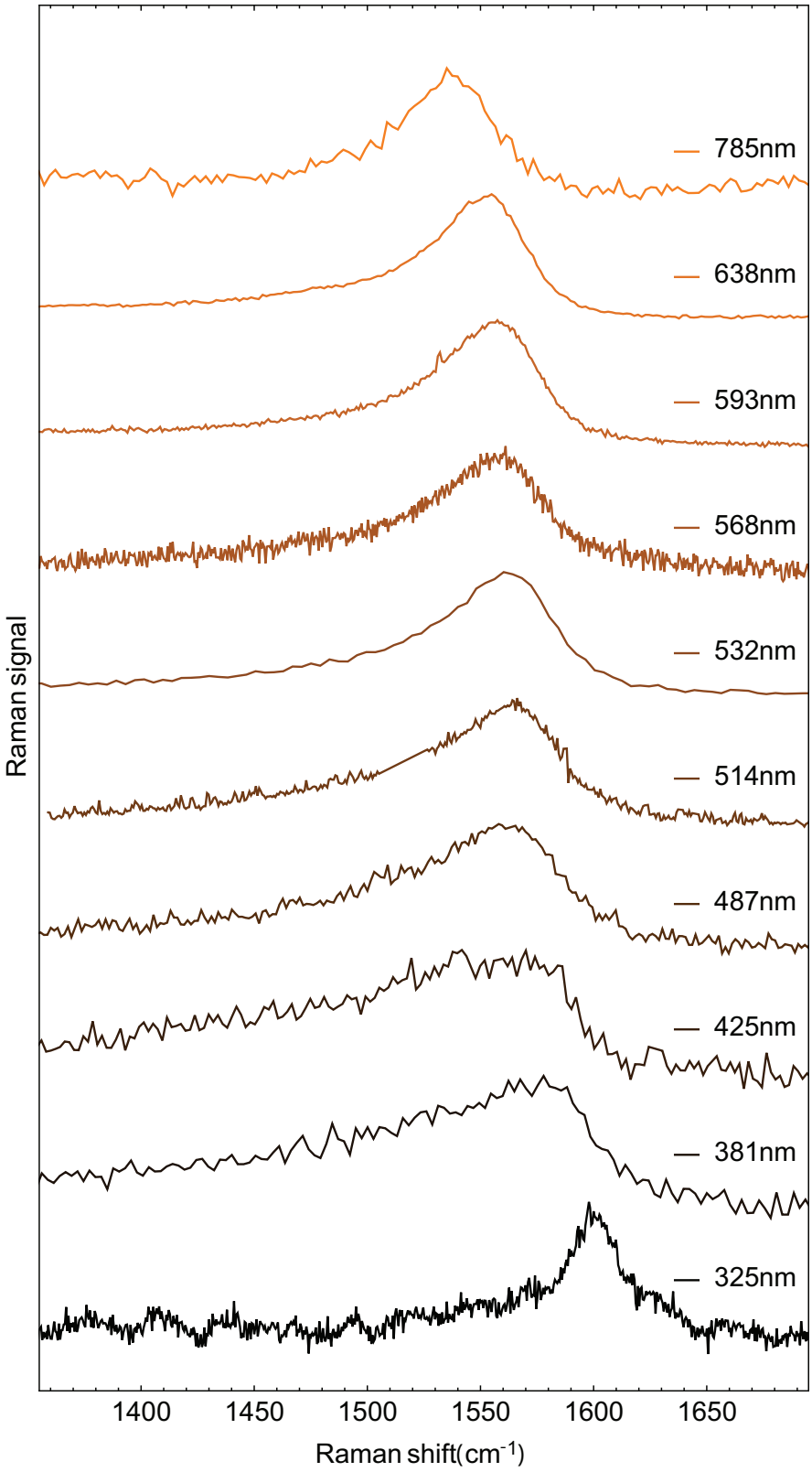

Figure 3.19: Normalized Raman spectra of potassium-doped monolayer graphene as a function of laser wavelength from 785 nm(top) to 325 nm(bottom). With increasing laser energy, the peak upshifts in position. The peak width and asymmetry first increase and then decrease again.

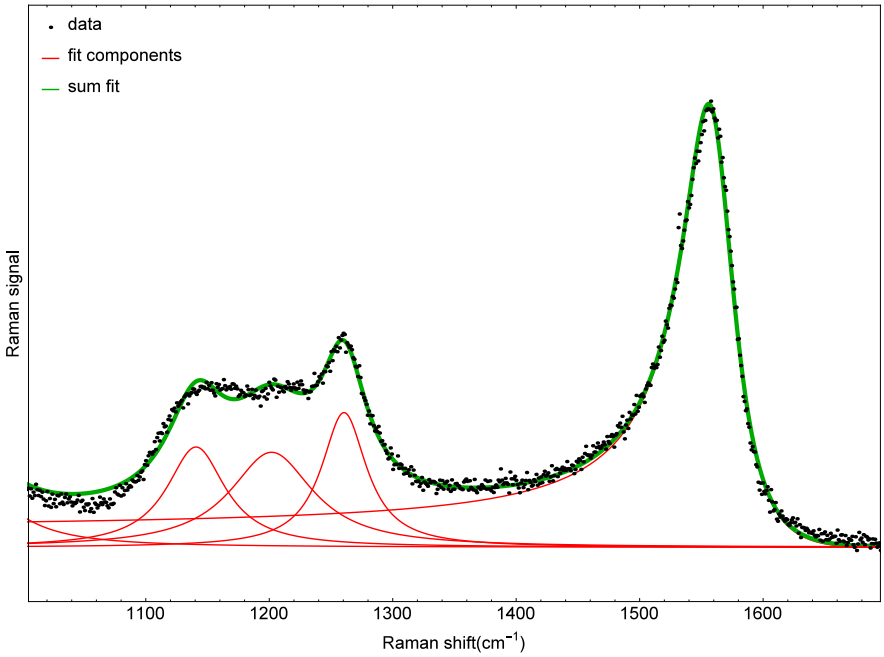

Figure 3.20: The fitted Raman spectrum of potassium-doped graphene at 593 nm. The data is shown as black dots, the fit components are shown in red and their sum is shown in green.

Peak Position

Figure 3.21 plots the Fano peak position as a function of laser energy. The position increases monotonically with increasing laser energy, from 1539.4 cm^{-1} at 1.58 eV to 1604.4 cm^{-1} at 3.82 eV. It is important to note that this peak position is not the spectral position of maximum intensity due to the Fano lineshape. In p-doped Si, the Raman peak around 521 cm^{-1} was also fitted with a Fano peak[52]. While the spectral position of maximum intensity also changes with laser energy in this system, the Fano peak position remains unchanged, in contrast to my observation in highly doped graphene.

From my measurements, I determine a slope of 26 cm^{-1}/eV with a linear fit. This value can be compared to the dispersion of the D and 2D line in pristine graphene and graphite, which are about 50 cm^{-1}/eV and 100 cm^{-1}/eV, respectively. This indicates that the phonon branch contributing to the signal in potassium-doped graphene has a smaller slope in the range of wavevectors probed than the TO branch near the K point in pristine graphene. The strength of the peak dispersion is also affected by the slope of the electronic band structure, meaning that a phonon branch with a slope similar to that of the TO branch near K could produce a dispersion of 26 cm^{-1}/eV if the slope of the electronic band structure were smaller than the Fermi velocity in pristine graphene.

For 425 nm and especially 371 nm, the peak position in potassium-doped graphene is fairly close to that of the G mode in pristine graphene (1583 cm^{-1}). However, the measurement at 325 nm makes it clear that there is no saturation of the peak position at higher excitation energies. The spectrum at 325 nm resembles a spectrum of doped graphene with a lower Fermi energy (before the

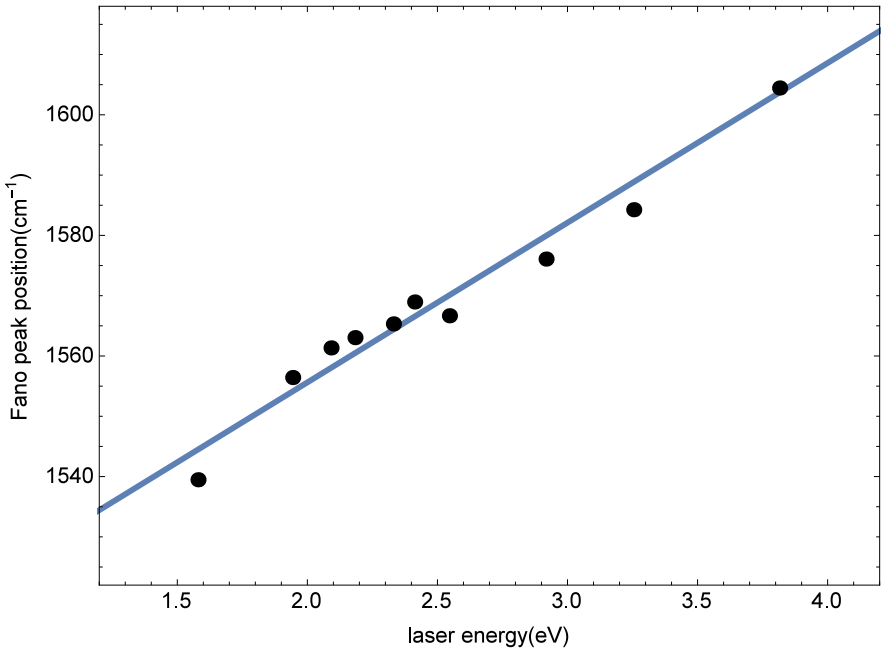

Figure 3.21: Peak position of the Fano peak in potassium-doped monolayer graphene as a function of laser energy. A linear fit of the data yields a slope of 26 cm^{-1}/eV.

peak downshifts below 1600 cm^{-1}), but I have excluded any laser-induces dedoping by measuring the spectrum at 532 nm after the measurement at 325 nm, with identical results as before.

To conclude this subsection I compare and contrast the laser energy dependence of potassium-doped graphene described above to pristine graphene, and also doped graphene with lower Fermi energies. In pristine graphene the G mode is not dispersive with laser energy. For low Fermi energies obtained e.g. through electrostatic gating, this behavior remains unchanged. Also for rubidium-doped graphene, where the G mode upshifts to up to 1607cm^{-1}, the peak position is the same for 488 nm and 514 nm laser excitation[7](although these laser wavelengths are very close). I have also measured the G mode peak position of a potassium-doped graphene sample that was not doped enough to show the lower-frequency Fano peak, shown in Fig. 3.22. At laser wavelengths of 532 nm and 638 nm, the peak positions are identical to within 1 cm^{-1} at 1605 cm^{-1}. For this difference in laser energy of about 0.4 eV, the Fano peak shifts by about 10cm^{-1}.

The dispersion of the Raman peak in potassium-doped graphene at high doping levels is thus in contrast to pristine and moderately doped graphene and indicates that this signal arises from a different Raman process compared to the G mode in pristine graphene.

Peak Width

I show the laser energy dependence of the full with at half maximum in Fig. 3.23. The peak is progressively broadened from 45.8 cm^{-1} at 1.58 eV to 81.2 cm^{-1} at 2.92 eV. However, the peak width decreases again for higher excitation energies. At 3.82 eV, the peak width is only 35.9cm^{-1}.

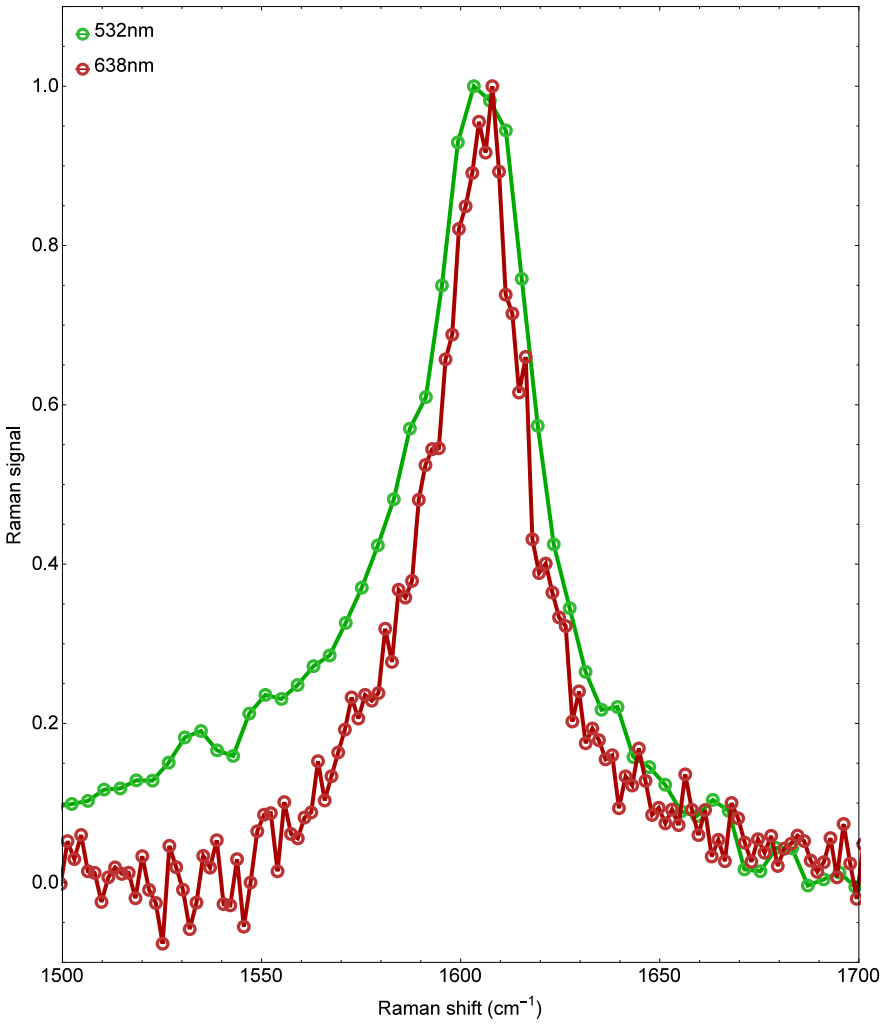

Figure 3.22: G mode Raman signal from a potassium doped graphene sample that was not doped so strongly as to show the Fano peak below the G line. The peak position is identical at 532 nm and 638 nm excitation.

The peak width of the Fano peak in potassium-doped graphene is obviously much larger than that of G mode in pristine graphene and electrostatically or electrochemically doped graphene. On the other hand, it should be noted that even at its maximum at 425 nm and 81.2 cm^{-1}, the peak is not as wide as that of the E_{2g} peak observed in KC_8, which exhibits 125 cm^{-1} width at 568 nm[62].

The maximum width observed in my measurements occurs between laser energies of 2.55 eV and 2.92 eV(487 nm and 425 nm). This energy matches twice the Fermi energy in my sample as determined from reflectivity, $2E_F$ = 2.60 eV.

In Ref. [6], the authors plot the peak width as a function of the peak position for their measurements with increasing doping time and Fermi energies. They observe a linear relation with negative slope, i.e. the larger the peak position the smaller the width[6], but measure only at one laser energy. I have observed that the peak position and width depend strongly on the laser energy, so that one explanation for the findings in Ref. [6] would be that for increasing doping time, the Fermi energy increases relative to the laser energy.

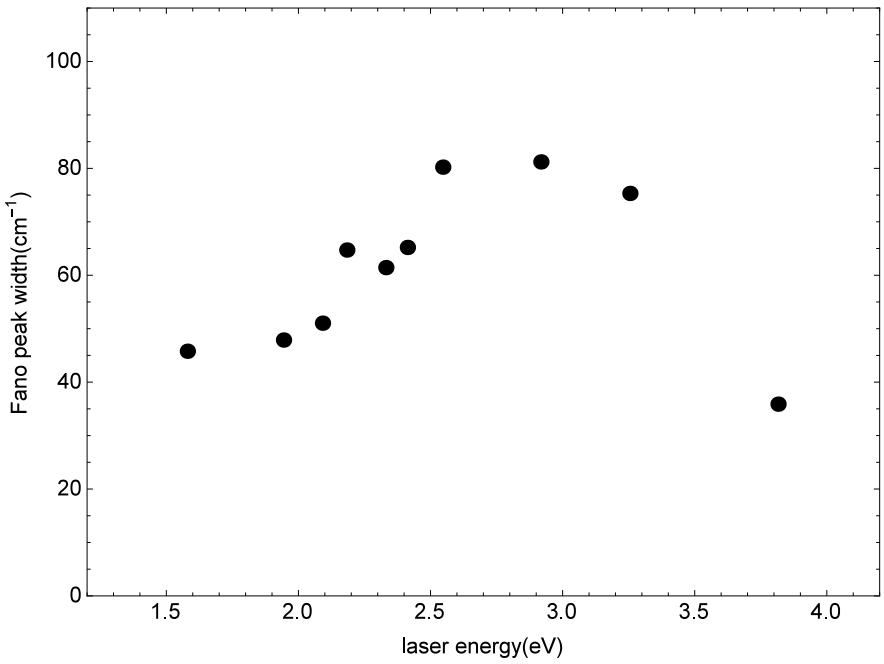

Figure 3.23: Peak width (FWHM) of the Fano peak in potassium-doped monolayer graphene as a function of laser energy. The peak width increases with increasing laser energy up to a maximum of 81.2 cm^{-1} at a laser energy of 2.92 eV and then decreases again.

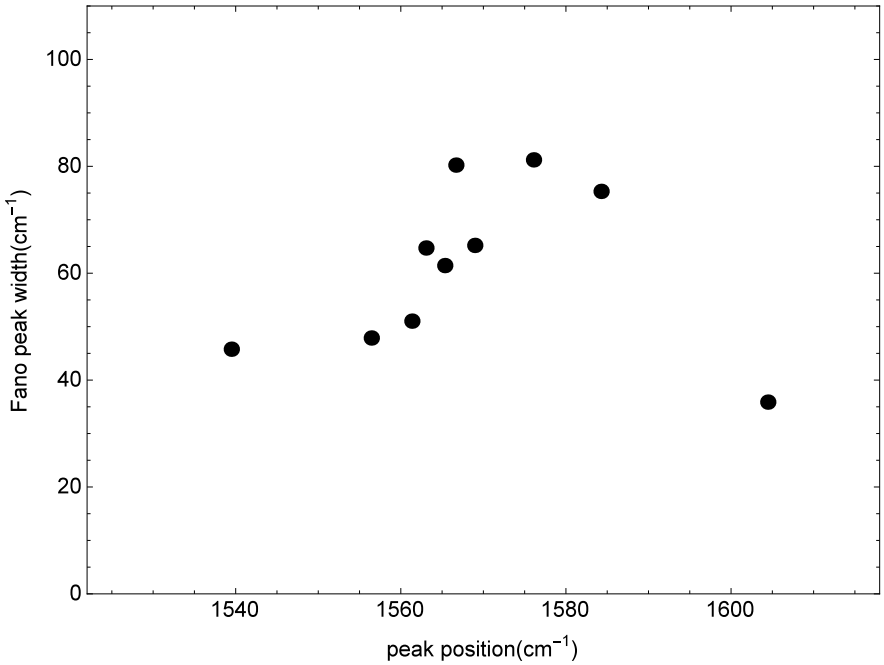

Figure 3.24: Peak width (FWHM) of the Fano peak in potassium-doped monolayer graphene as a function of peak position. The plot resembles Fig. 3.23 because the peak position depends linearly on the laser energy.

I plot the peak width as a function of the peak position in the laser energy dependent measurements in Fig. 3.24. Since the peak position increases linearly with laser energy, the plot resembles Fig. 3.23, and shows first a linear increase of peak width with increasing peak position. This indicates that the movement of the Fermi energy relative to the laser energy does not account for the observations in Ref. [6]. Nevertheless, to find the true maximum peak width for a given Fermi energy, it is necessary to measure the Raman spectrum at a laser energy of twice the Fermi energy, whereas Howard et al. used only a fixed laser energy for all doping times and thus Fermi energies. They consequently report a too small width for all measurements except when twice the Fermi energy happens to match their laser energy. In particular, it is possible that for the most heavily doped data point, where they observe a width of slightly less than 150 cm^{-1}, a value closer to that of KC_8 (which they report as around 190 cm^{-1}) could be observed with the appropriate laser wavelength.

Peak Asymmetry

Lastly, I turn to the asymmetry parameter of the Fano lineshape, which I show in Fig. 3.25. In this definition large values of q indicate a symmetric peak, with $q = \infty$ for a Lorentzian lineshape. I observe an increase in q from −8.25 at 1.58 eV laser energy up to −2.37 for 2.92 eV. Similar to the behavior of the peak width, the asymmetry then also decreases for higher excitation energies, to −5.74 at 3.82 eV.

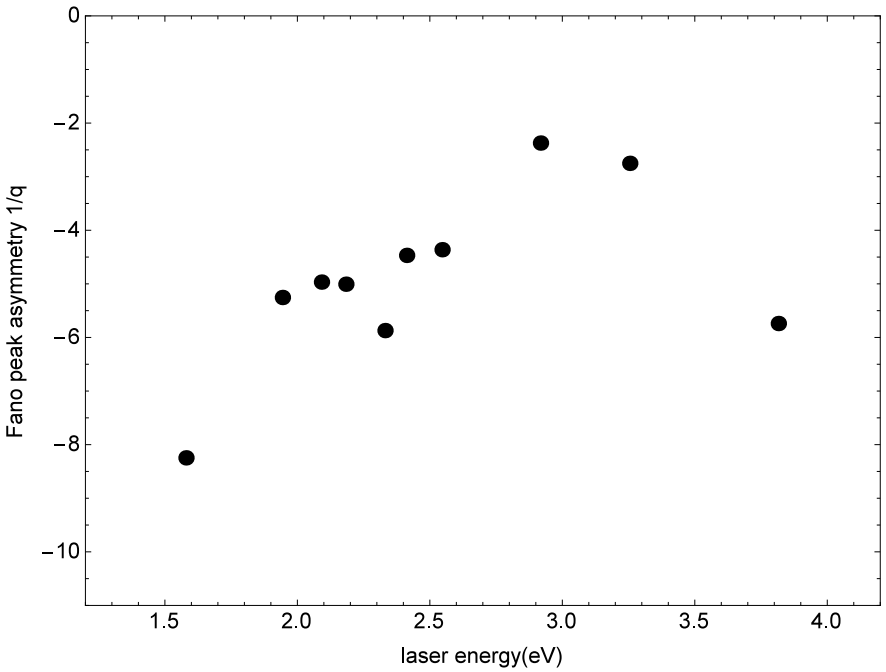

Figure 3.25: Asymmetry parameter $1/q$ of the Fano peak in potassium-doped monolayer graphene as a function of laser energy. The asymmetry first increases with increasing laser energy up to −2.37 at 2.92 eV and then decreases again.

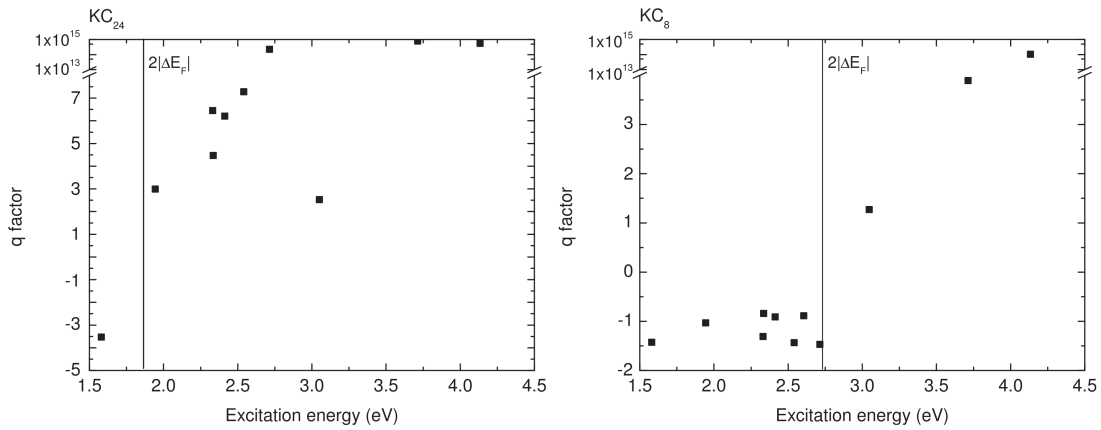

Figure 3.26: Asymmetry parameter 1/q of the Fano peak in KC_{24} and KC_8 as a function of laser energy from Ref. [67]. They observe a zero crossing in the asymmetry parameter.

From formula 3.5 it can be seen that as the asymmetry parameter approaches zero from below, the Fano peak develops a dip at higher wavenumbers in the spectrum. If the asymmetry parameter crosses zero, the peak then exhibits asymmetry in the other direction, with larger intensity at higher wavenumbers. This zero crossing of the asymmetry parameter has been observed experimentally in KC_{24} and KC_8 in Ref. [67], although their spectra's signal to noise ratios leave something to be desired especially for the spectra with q close to zero. They do not show any spectra exhibiting a dip, but a number of spectra with positive values for the asymmetry parameter. They also claim that the zero crossing of the asymmetry parameter occurs at an excitation energy close to twice the Fermi energy (2.1 eV for KC_{24} and 2.7 eV for KC_8). My observations for the asymmetry parameter in potassium-doped monolayer graphene are in contrast to these results for the E_{2g} peaks in KC_{24} and KC_8.

I clearly do not observe a zero crossing in the asymmetry parameter, which instead starts to decrease again at a laser energy of around twice the Fermi energy. This is in turn similar to my observations concerning the peak width.

Additional Peaks

In addition to the Fano peak above 1500 cm^{-1}, the spectrum of potassium-doped graphene also contains three more peaks in the region between 1100 cm^{-1} and 1400 cm^{-1}. They are shown at selected wavelengths in Fig. 3.27. These peaks are about 50 cm^{-1} broad, they overlap and they are much weaker in intensity than the Fano peak. They can consistently be fitted with three components at around 1140 cm^{-1}, 1200 cm^{-1}, and 1260cm^{-1} which do not appear to disperse with laser energy. However, it is clear from Fig. 3.27 that the peaks' intensity depends on the laser energy. Relative to the intensity of the Fano peak, the additional peaks are strongest at 785 nm and then decrease in intensity. At 325 nm they are not observable.

These additional peaks were also observed in Ref. [6], where Raman inac-

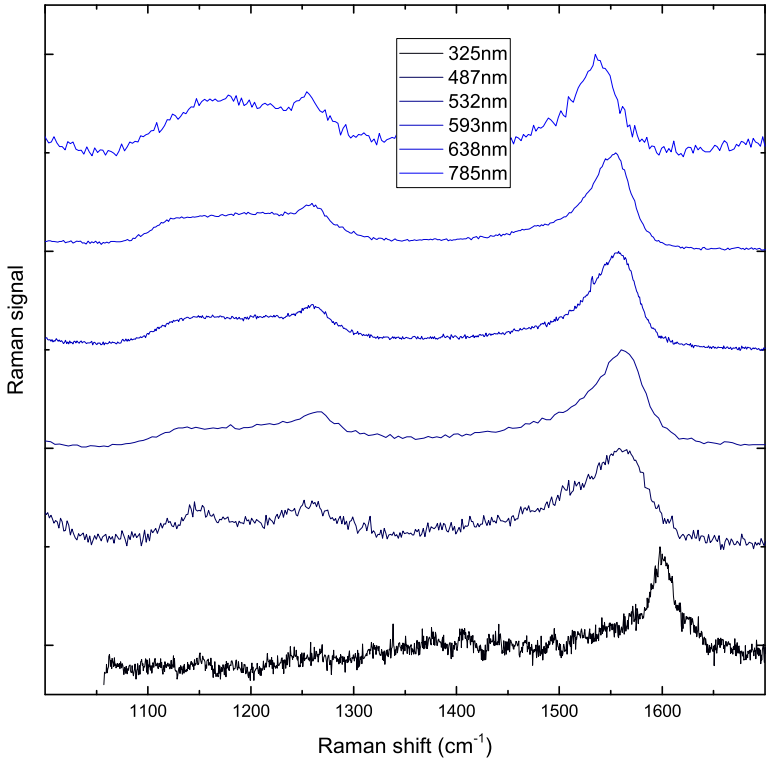

Figure 3.27: Raman spectra of potassium-doped graphene in a broader spectral range, showing additional peaks at lower frequencies than the Fano peak.

tive Γ point phonons that are activated by disorder of the potassium atoms are mentioned as one possible explanation.

3.3.4 Layer Number Dependence of the Raman Spectrum

Having described the behavior of the Raman signal of highly doped monolayer graphene as a function of laser energy in the previous section, I now turn towards a description of the behavior as a function of layer number. In addition to monolayer, my sample has areas of bilayer, four layer, and five layer graphene, as well as areas of thicker graphite (more than 100 layers). In this section I will describe the position, linewidth and asymmetry. Furthermore, I have performed measurements on the multilayer samples with different laser energies, allowing me to discuss the dispersion of the 1560cm^{-1} Raman peak as a function of layer number.

I begin by examining Raman maps of the doped graphene flake with areas of bilayer, four layer and five layer graphene, shown in Fig. 3.28. Spectra were acquired with a step size of 1 μm. In the upper row I show the maps of the pristine sample. The intensity of the G mode and the 2D mode increases with layer number, with that of the G mode in particular being approximately proportional to layer number from one to five layers. The width of the 2D mode also increases with layer number.

The bottom row of Fig. 3.28 shows the integrated intensity, the position, and

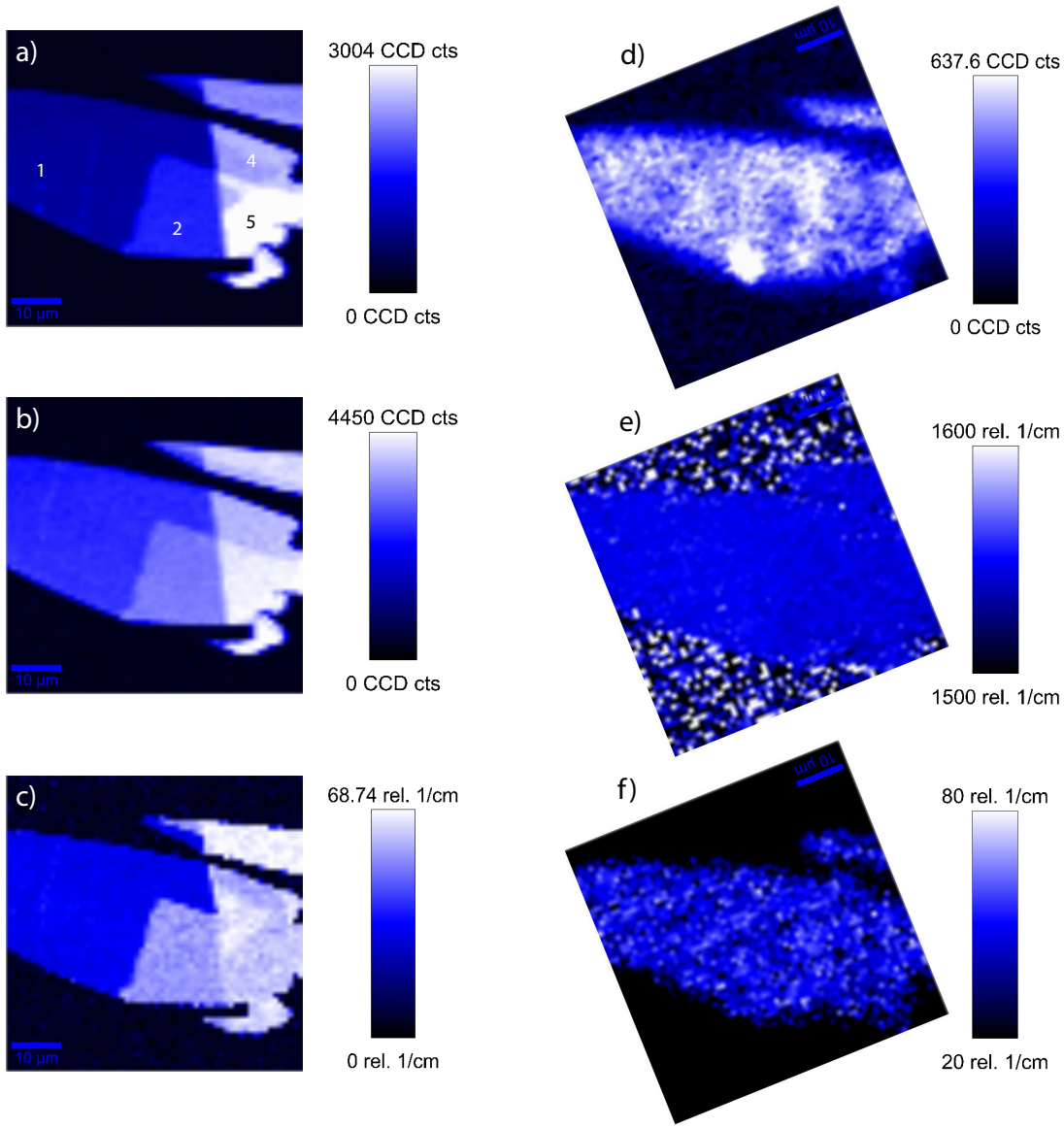

Figure 3.28: Raman mapping of pristine and doped graphene from one to five layers: **a)** Pristine G mode intensity with layer number, **b)** pristine 2D mode intensity, **c)** pristine 2D mode width, **d)** doped intensity, **e)** doped peak position, **f)** doped width.

the width of the Fano peak in potassium-doped graphene. I find that all three parameters are uniform over the entire flake, irrespective of the layer number. The uniform intensity is surprising because all peaks increase in intensity for larger layer numbers in pristine graphene. Furthermore, the properties of the 2D mode in pristine graphene, which is somewhat similar to the Fano peak in potassium-doped graphene in that it shifts in position with laser energy, depend strongly on layer number. This includes the position, width and number of fit components. This is in contrast to the position and width of the Fano peak in potassium-doped graphene.

Figure 3.29 shows the position of the Fano peak in potassium-doped graphene with varying layer number as a function of laser energy. It also includes data

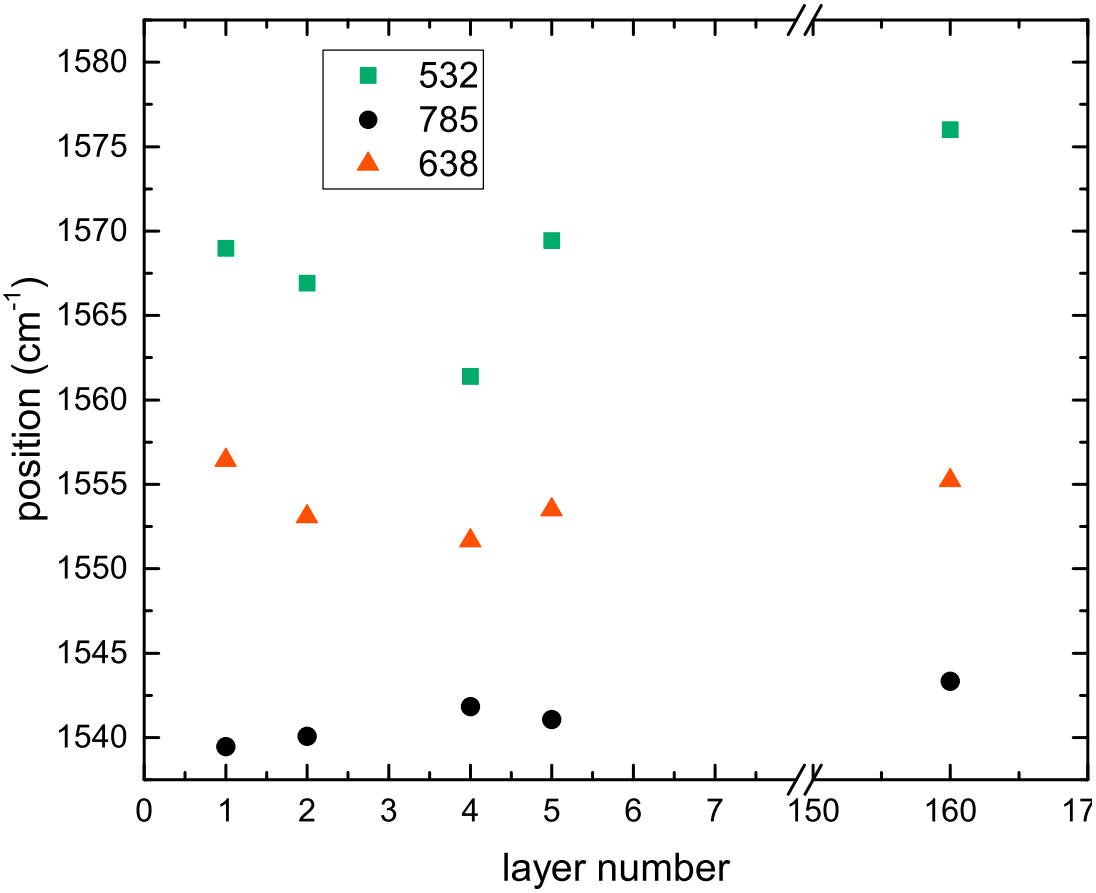

Figure 3.29: Fano peak position as function of layer number for laser wavelengths of 532 nm, 638 nm and 785 nm.

from a 160 layer graphite flake. Its thickness was determined before the intercalation with the help of its reflectivity spectrum. At 2.33 eV(532 nm), the peak position decreases from monolayer(1569 cm^{-1}) to four layer(1561 cm^{-1}) and then increases to 1569 cm^{-1} for the five layer and 1576 cm^{-1} for the 160 layer flake. At 1.58 eV(785 nm), the peak position varies much less with layer number(within only 4 cm^{-1}), and is again highest for the 160 layer flake. From the measurements at three wavelengths, it is obvious that the Fano peak disperses with laser energy in the multilayer samples similarly to the monolayer. Indeed, as shown in Fig. 3.30, the slope of the dispersion is 26 cm^{-1}/eV for monolayer as discussed in Sec 3.3.3 and very similar in four layer graphene, but lies between 35 cm^{-1}/eV and 45 cm^{-1}/eV for bilayer and five layer graphene and the 160 layer flake. While there is no clear trend in the dispersion, the last data point is particularly striking since there have been no reports of a dispersion of the 1510 cm^{-1} Raman peak of bulk KC_8 in the literature.

I now discuss the full width at half maximum of the Raman peak as a function of layers and laser energy. Figure 3.31 shows this data with measurements at 532 nm plotted in green, 638 nm plotted in red, and 785 nm plotted in black. At 532 nm, the peak width increases from 63 cm^{-1} to 83 cm^{-1} from monolayer to 160 layers, with the exception of five layers where it is only 65 cm^{-1}. At

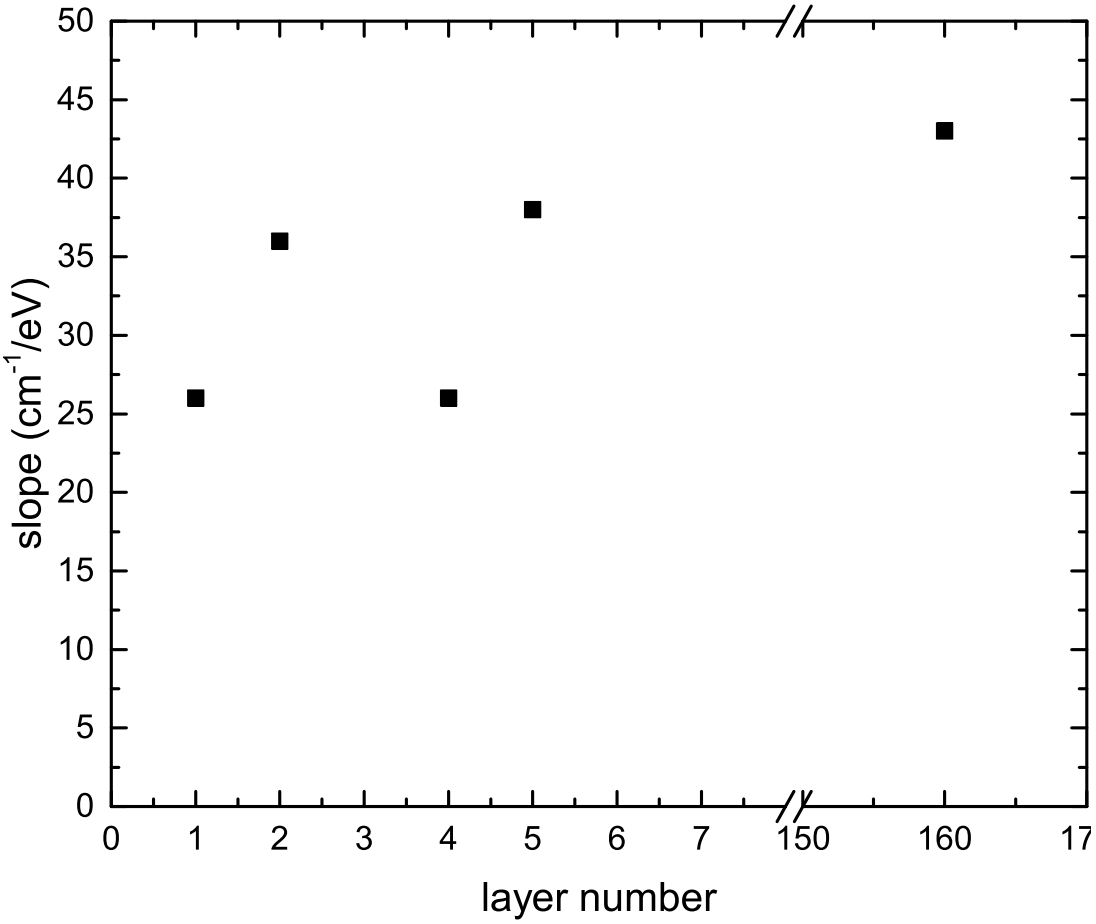

Figure 3.30: The slope of the dispersion of the Fano peak with laser energy as a function of layer number.

638 nm, the peak width increases from 48 cm^{-1} for monolayer to 62 cm^{-1} for the graphitic sample. At 785 nm, the peak width actually decreases from 46 cm^{-1} for monolayer to 37 cm^{-1} for four layers, and then increases again to 49 cm^{-1} for the graphitic sample. It is clear that the full width at half maximum of the highly doped graphene Raman peak is much larger than that of the G line of pristine graphene (around $10 - 15$ cm^{-1}) for all laser energies and layer numbers. Furthermore, it is also smaller than the more than 100 cm^{-1} of bulk KC8 even for the many-layer sample at 532nm.

3.3.5 Long Term Stability of Potassium-doped Graphene

In Fig. 3.32, I show the Raman spectrum of maximally doped graphene at 532 nm laser wavelength obtained right after potassium evaporation and one and three months later. The Raman signal is unchanged, indicating excellent long term stability of the sample in a sealed evacuated ampule.

A possible route towards a sample of highly doped graphene stable in air is hinted at by experiments on a heterostructure of a graphene monolayer sandwiched by two thicker layers of hexagonal boron nitride (hBN). In this sample

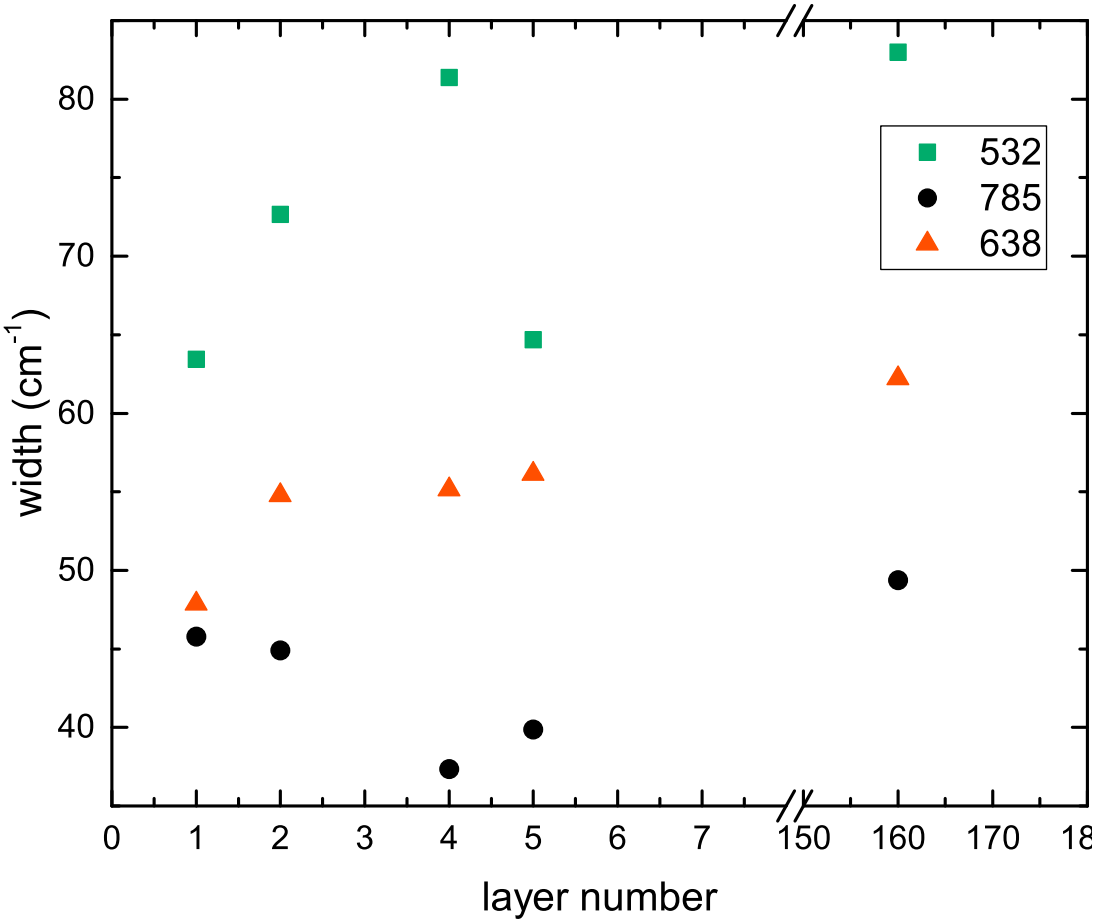

Figure 3.31: Fano peak width as function of layer number for laser wavelengths of 532nm, 638nm and 785nm.

the graphene was also smaller laterally than the hBN layers, so that the graphene is not exposed to the environment. This sample was also placed in a sealed evacuated ampule together with potassium. Upon evaporation of the potassium, the graphene Raman signal remained unchanged from that of pristine graphene, which is a strong indication that the potassium cannot permeate through the hBN neither from the top nor from the sides between the layers. Potassium-doped graphene protected from the environment could be created as follows:

- Preparing potassium doped graphene without hBN on top as in the previous experiments,
- Opening the ampule in a glove box under inert atmosphere,
- Depositing an hBN flake on top of the graphene inside the glove box.

It should be possible to take this sample outside of the glove box into ambient conditions. The potassium would not be able to detach from the graphene because of the top hBN, and also would not oxidize as long as oxygen cannot pass through the hBN. I am unable to prepare a sample like this because there is no micromanipulator for the deposition of the top hBN layer in our glove box.

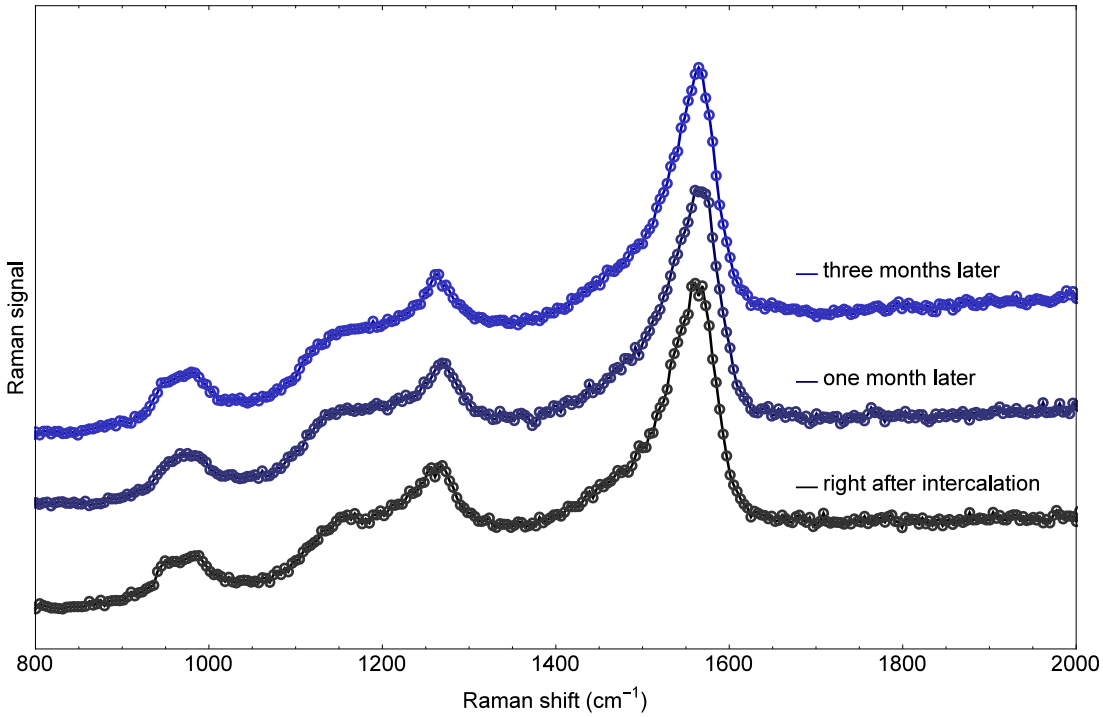

Figure 3.32: The Raman signal of potassium-doped graphene in a sealed evacuated ampoule (532 nm laser wavelength) right after intercalation, one month later, and three months later.

3.3.6 Polarization-dependent Raman Spectra

The polarization dependence of the Raman signal of a given phonon mode is given by its symmetry and the corresponding Raman tensor. In this section I will only consider polarizations in the graphene plane for both incoming and outgoing photons. As has been demonstrated in the literature, the G mode in pristine Graphene, which arises from E_{2g} phonons, is independent of the angle between the polarization of incoming and outgoing light. By contrast, the double-resonant 2D mode exhibits a polarization dependence in the Raman signal. The signal for parallel polarization is three times stronger than for crossed polarization. Both the G and 2D mode intensities are independent of the orientation between the polarization of the incoming laser light and the crystal lattice.

The idea behind the investigation in this section is that if the Raman peak I observe in potassium-doped graphene arises from the same phonons as the G mode in pristine graphene, it should also share the same polarization behavior. By the same logic, a difference in the polarization behavior for the Raman signal of potassium-doped graphene would be a sign that it does not arise from the same phonons as in pristine graphene, and could maybe point towards an explanation and the responsible Raman scattering process. The experimental setup used to measure polarization-dependent Raman spectra is described in Sec. 3.2.2.

I briefly discuss the selection rules for Raman scattering in graphene. The possible Raman tensors for the D_{6h} point group are listed in Table 3.3. My scattering geometry has incoming and outgoing light propagating along the z axis

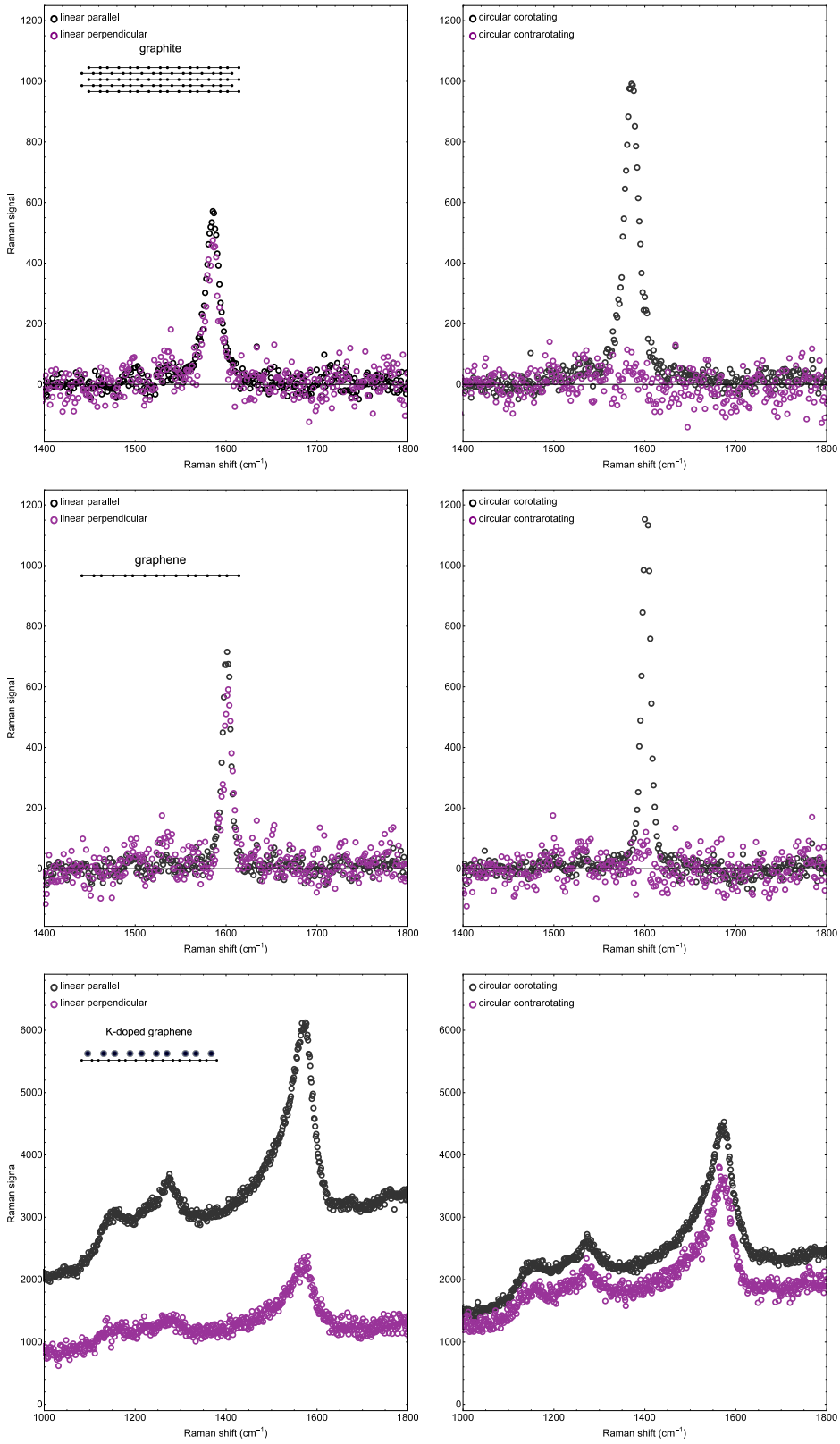

Figure 3.33: Polarization dependence of the G mode of pristine graphite (top), pristine graphene (middle), and potassium-doped graphene (bottom).

Table 3.3: Raman tensors for the D_{6h} point group.

A_{1g}	E_{1g}		E_{2g}	
$\begin{pmatrix} a & 0 & 0 \\ 0 & a & 0 \\ 0 & 0 & b \end{pmatrix}$	$\begin{pmatrix} 0 & 0 & 0 \\ 0 & 0 & c \\ 0 & c & 0 \end{pmatrix}$	$\begin{pmatrix} 0 & 0 & -c \\ 0 & 0 & 0 \\ -c & 0 & 0 \end{pmatrix}$	$\begin{pmatrix} d & 0 & 0 \\ 0 & -d & 0 \\ 0 & 0 & 0 \end{pmatrix}$	$\begin{pmatrix} 0 & -d & 0 \\ -d & 0 & 0 \\ 0 & 0 & 0 \end{pmatrix}$

and polarized in the x-y plane. To calculate the intensity I contract the Raman tensors between $(1,0,0)$ and $(1,0,0)$ for linear parallel scattering, $(0,1,0)$ and $(1,0,0)$ for linear perpendicular scattering, $(1,i,0)/\sqrt{2}$ and $(1,i,0)/\sqrt{2}$ for circular corotating scattering, and $(1,-i,0)/\sqrt{2}$ and $(1,i,0)/\sqrt{2}$ for circular contrarotating scattering. This results in the scattering intensities listed in Table 3.4. To summarize, there is no E_{1g} scattering in this geometry, A_{1g} scattering can be

Table 3.4: Raman intensities for the D_{6h} point group.

	A_{1g}	E_{1g}		E_{2g}	
linear parallel	a^2	0	0	d^2	0
linear perpendicular	0	0	0	0	d^2
circular corotating	0	0	0	d^2	d^2
circular contrarotating	a^2	0	0	0	0

observed in linear parallel and circular contrarotating polarizations, and E_{2g} scattering is allowed in linear parallel, linear perpendicular and circular corotating polarizations. I thus expect the G mode in pristine graphene and graphite to be visible in all polarizations except circular contrarotating. This is indeed observed experimentally as shown in Fig. 3.33. Also as expected, the sums of the two linear polarizations and the two circular polarizations are equal.

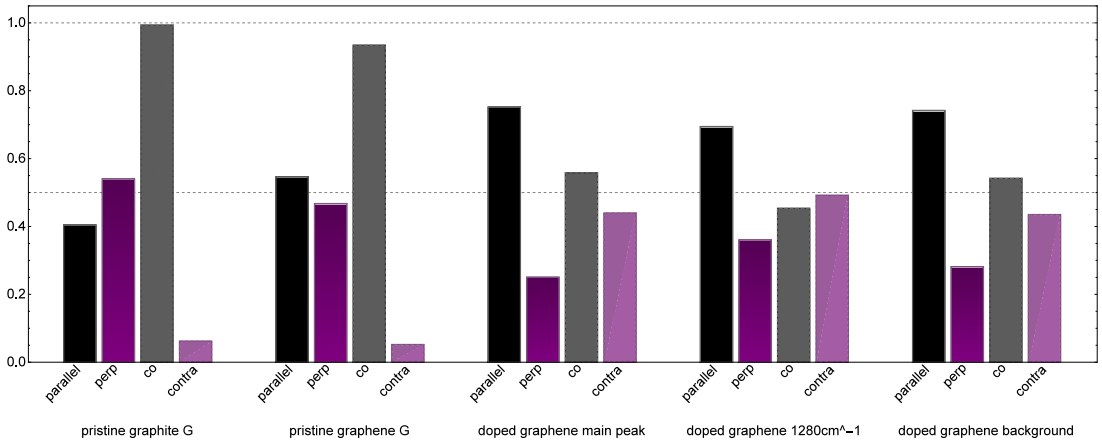

Figure 3.34: Polarization dependence of the Raman signal of potassium doped graphene.

Having verified the functionality and accuracy of the polarization dependent

Raman setup, I then turn towards the Raman signal of maximally doped Graphene (bottom row in Fig. 3.33). The signal of the main Raman peak is only about one third as strong as strong for perpendicular linear polarizations as for parallel ($I_\perp/I_\parallel$ = 0.33). Furthermore, the signal does not disappear in circular contrarotating polarization, but is almost as strong as for circular corotating ($I_{\circlearrowright\circlearrowright}/I_{\circlearrowright\circlearrowleft}$ = 1.27). Again the sum of the intensities in the linear polarizations is the same as that in the circular ones. All intensities are summarized in Fig. 3.34.

The observed polarization dependence of the Raman signal of potassium-doped graphene shows that the scattering arises from both E_{2g} and A_{1g} contributions to the Raman tensor, instead of just E_{2g} in pristine graphene. This fact is shown very clearly in the top row of Fig. 3.36, where I replot the data to isolate the E_{2g} and A_{1g} components. The A_{1g} component is contained in the contrarotating spectrum and can be isolated by subtracting the corotating spectrum from the sum of the linear polarizations, whereas the E_{2g} component is present alone in the corotating spectrum and can also be obtained by subtracting the contrarotating spectrum from the sum of the linear polarizations. The signal in potassium-doped graphene therefore cannot arise from the same phonon as the G mode in graphene. It is inaccurate to refer to the 1560 cm^{-1} peak in potassium-doped graphene as the G peak of highly doped graphene. This finding is also supported by the observed laser energy dependence of the peak position in potassium-doped graphene detailed in Sec. 3.3.3.

I also note that the strongest, asymmetric peak in the spectra of potassium-doped graphene in e.g. circular corotating and circular contrarotating polarizations (only E_{2g} and only A_{1g} scattering, respectively), can be fitted with the same Fano peak with identical width, position and asymmetry. This indicates that the signal originates from one mode with mixed symmetry, rather than one mode of A_{1g} symmetry and one mode of E_{2g} symmetry.

I further analyze the polarization dependence of the weaker peak at around 1280 cm^{-1} and of the background signal between 1800 cm^{-1} and 1850 cm^{-1}(this spectral range was selected because of the absence of distinct peaks there). For the analysis of the background signal I subtracted spectra acquired in each polarization geometry on the silicon wafer just next to the potassium-doped graphene flake. The results can be seen in the last two groups in Fig. 3.34. The polarization behavior of the background signal is the same as that of the main asymmetric peak discussed above. The secondary peak at 1280 cm^{-1} also demonstrates both A_{1g} and E_{2g} scattering. Here I find $I_\perp/I_\parallel$ = 0.52 and $I_{\circlearrowright\circlearrowright}/I_{\circlearrowright\circlearrowleft}$ = 0.92., indicating a slightly stronger A_{1g} contribution compared to the main peak.

In the literature there are references to the Raman peak of KC_8 as having purely E_{2g} symmetry[63], but I was unable to find Raman measurements with circularly polarized light on KC_8. I therefore conduct such measurements for comparison to my results on potassium-doped monolayer graphene. The spectra are shown in Fig. 3.35 (middle row). There is the main peak at 1510 cm^{-1} and an additional peak at 1550 cm^{-1}. The former is present with comparable intensity in linear parallel and perpendicular polarizations. The results for circular polarization are striking and confirm my expectations: The KC_8 peak at 1510 cm^{-1}

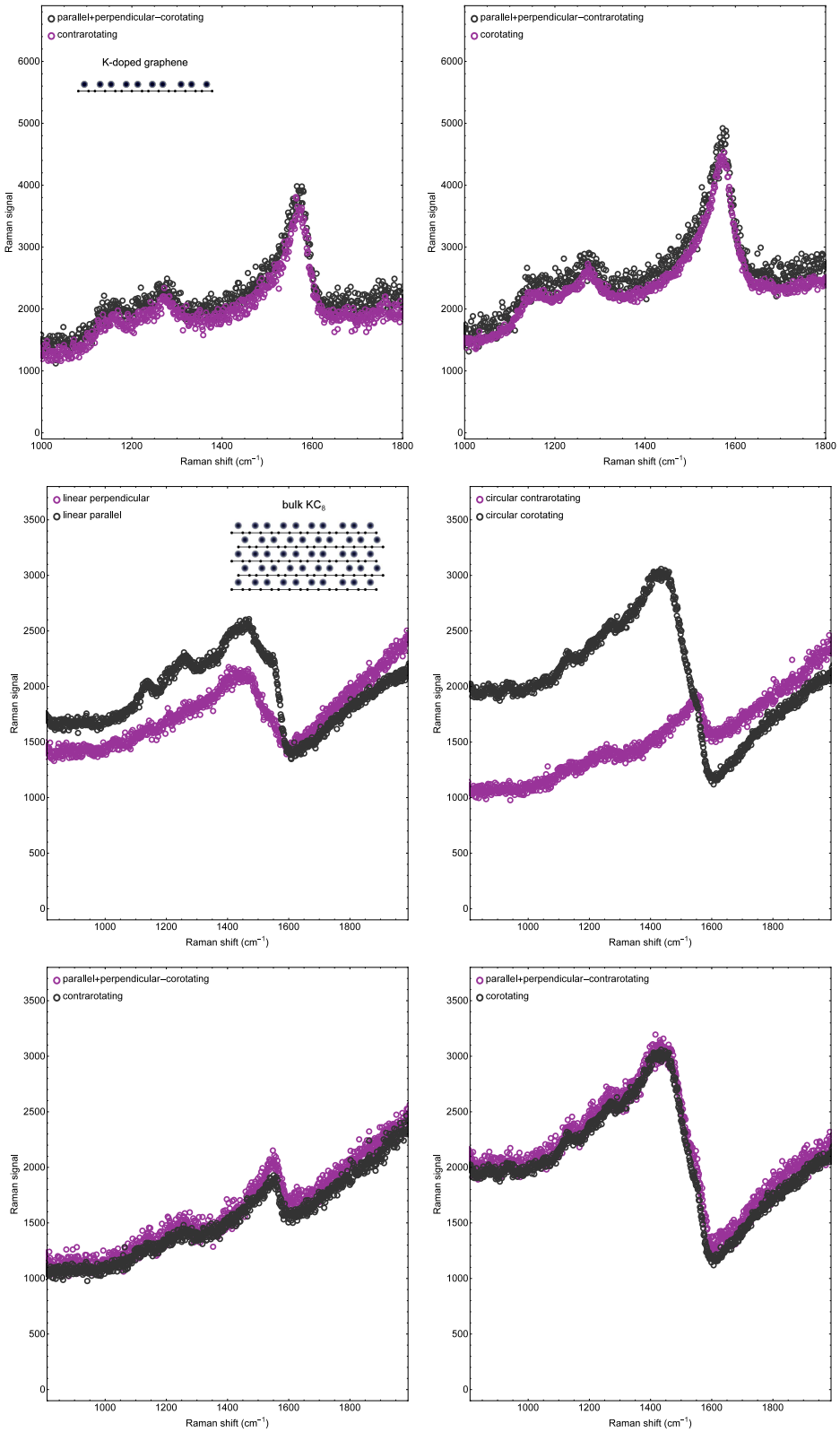

Figure 3.35: Top row: Decomposition of the Raman signal of K-doped graphene into A_{1g} (left) and E_{2g} (right) contributions. Middle row: Polarization dependence of the Raman signal of KC_8 using linearly (left) and circularly (right) polarized light. Bottom row: Decomposition of the Raman signal of KC_8 into A_{1g} (left) and E_{2g} (right) contributions. All spectra acquired at 532 nm

is strong in circular corotating polarization and is completely absent in circular contrarotating polarization.

This reaffirms the contrast to potassium-doped monolayer graphene. The bulk of the KC_8 Raman signal has clear E_{2g} symmetry whereas the signal in potassium-doped monolayer graphene exhibits mixed A_{1g} and E_{2g} symmetry. However, an examination of the second peak in the KC_8 signal, which appears as a shoulder in the linear parallel signal, shows that it exhibits very similar behavior as the peak in potassium-doped monolayer graphene: It is present in roughly equal strength in the A_{1g} symmetry and E_{2g} components (bottom row of Fig. 3.35). Furthermore, this second peak is also dispersive with laser energy: A measurement of KC_8 at 487 nm reveals that the peak has shifted to higher frequencies compared to 532 nm and is more separated in frequency from the E_{2g} component at this lower wavelength. The increasing peak position with increasing laser energy matches the behavior in potassium-doped monolayer graphene. Unfortunately an investigation of the second peak in KC_8 is not possible over a broader wavelength range because KC_8 did not give any Raman intensity outside of the green and blue spectral range.

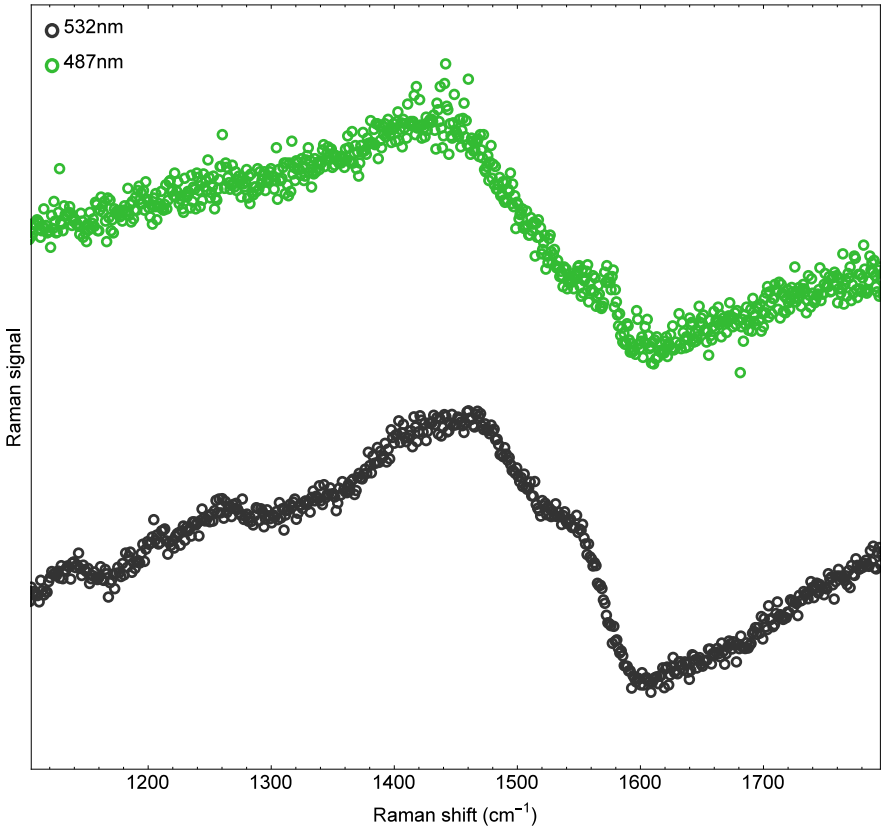

Figure 3.36: Raman signal of KC_8 at 532 nm (black) and 487 nm (green).

The polarization and laser energy dependence of this second peak in KC_8 point to a similar origin for this peak as for the peak in potassium-doped monolayer graphene. One could thus assign these peaks to the outer doped graphene layer in KC_8, which shows the same Raman signal as isolated doped graphene, while the bulk KC_8 gives rise to the broader E_{2g} peak at 1510 cm^{-1}. It is unclear however it

is not possible to observe the second peak in KC_8 over the same broad wavelength range as the peak in potassium-doped monolayer graphene.

3.3.7 Origin and Explanation of the Observed Raman behavior

I have observed several characteristics of the Raman signal of potassium-doped graphene that require an explanation:

The broadened lineshape and the asymmetry of the Raman peak around 1560 cm^{-1} that I have detailed in the previous section, as well as the background signal observed over a broad spectral range, point toward a continuum of electronic scattering channels.

In pristine graphene, the G-mode phonon can decay into low-energy electron hole pairs, leading to an additional relaxation channel and a broader phonon peak. This phenomenon is even more pronounced in metallic nanotubes, were the lower frequency G peak is very broad (around 50 cm^{-1}) and also exhibits an asymmetry that is thought to arise from a competition between the discrete phonon scattering channel and a continuum of electronic scattering channels, leading to a Fano lineshape.

Clearly the broadening of the Raman peak in my spectra is much stronger than in pristine graphene, as is the asymmetry, which is very hard to observe in pristine graphene. This points towards either a larger density of states at the Fermi energy or stronger coupling between the two scattering channels[52].

However, all the peak positions reported in the previous sections are obtained by fitting the spectrum to a Fano peak. Consequently the peak position should be independent of laser energy if the Fano mechanism were the only effect in play[52] for a $q = 0$ phonon peak, but it is clearly not.

The prevalent mechanism to explain a dispersive Raman peak in carbon materials (graphite, graphene, and carbon nanotubes) is a double resonant (or more) $q \neq 0$ Raman process. For these non Γ phonon Raman processes, momentum conservation can be satisfied either by scatting by a defect, as in the D peak, or by multiple phonon scattering, as in the 2D peak.

To determine if there are a large enough number of defects in my doped samples to enable a single-phonon Raman scattering signal of the strength that I observe, a first instinct might be to examine the D peak intensity. This peak is absent in my undoped graphene. It is doubtful that the additional peaks below the Fano peak contain the D peak because they do not disperse with laser energy. However, the D peak might be absent not just because there are few defects, but also because it is blocked because of the Fermi energy shift, as is the 2D peak.

A convincing explanation of the observed behavior of the Raman signal of highly doped graphene will require knowledge of the electronic band structure and the phonon dispersion of this system. As can be seen from the band structure of CaC_6 and LiC_8 in Ref. [63], it is not sufficient to simply consider a rigid-band shift of the Fermi energy, as is done to explain the lifting of the Kohn anomaly and the blocking of the additional phonon relaxation channel at Fermi energies on the scale of few 100s of meV.

The band structure of KC_8 and a doped graphene layer with the same Fermi energy has been calculated in Ref. [68]. It shows bands close to the Fermi energy. A next step is then to find electronic excitations that are similar in energy to the observed phonon peak, which would explain the background signal as well as the broadening and asymmetry.

However, to fully explain the frequency dispersion, a suitable phonon branch where either the phonon energy or twice the phonon energy in case of a two-phonon process matches the Raman peak position has to be found. A simple inspection of the phonon dispersion of graphite in Ref. [47] shows that LO branch between Γ and M or between Γ and K contains frequencies that I observed experimentally. However, the calculation of the phonon frequency in KC_8 in Ref. [63], which was only accurate after consideration of non-adiabatic effects, indicates that it is not sufficient to examine the phonon dispersion of pristine graphite to explain the laser energy dependence of the Fano peak I observe in potassium-doped graphene. A conclusive explanation will furthermore rely on a calculation of the Raman signal including the matrix elements for electron-photon and electron-phonon coupling.

3.4 Summary

To conclude this chapter, I have presented a comprehensive Raman study of potassium-doped graphene. I monitored the behavior during the potassium intercalation up to the maximally doped state. I then proceed to characterize the final state Raman spectrum as a function of laser energy, where I observe changes in position, linewidth and asymmetry that are in contrast to the behavior of pristine and less strongly doped graphene. I investigated different graphene layer numbers, where the differences were weaker than expected. To determine the symmetry of the phonon mode that gives rise to the Raman signal, I conduct polarization-resolved Raman spectroscopy and again find strong disagreement with the behavior in pristine graphene.

4 | Electrochemical Raman Spectroscopy of Single-walled Carbon Nanotubes

4.1 Theoretical Background

4.1.1 Geometric structure

Carbon nanotubes are a class of one-dimensional materials that can be visualized as rolled-up graphene sheets. One distinguishes between single-walled[19] and multi-walled[69] tubes, but we will deal exclusively with the former type in this thesis. In single-walled carbon nanotubes, the carbon atoms are arranged in a hexagonal lattice on a cylindrical surface and the diameter of the tube ranges from about 0.5 to 2 nm. As there are many ways of rolling up a graphene sheet, there are many possible carbon nanotube structures. They are defined by their chiral vector, a graphene lattice vector which turns into the tube circumference when the sheet is rolled up. The chiral vector can be expressed as a sum of multiples of the graphene lattice basis vectors $\mathbf{a}_1$ and $\mathbf{a}_2$ as[70,71]

$$\mathbf{c} = n_1\mathbf{a}_1 + n_2\mathbf{a}_2. \tag{4.1}$$

The linear coefficients n_1 and n_2 in this equation are called chiral indices and define the tube structure. From the chiral indices we can calculate the tube diameter d and the chiral angle θ, the angle between the chiral vector and the zig-zag direction in the graphene lattice, as follows:[70]

$$d = \frac{|\mathbf{c}|}{\pi} = \frac{a_0}{\pi}\sqrt{n_1^2 + n_1 n_2 + n_2^2}, \tag{4.2}$$

where $a_0 = |\mathbf{a}_1| = |\mathbf{a}_2| = 2.461$Å is the length of the graphene lattice basis vectors, and

$$\theta = \arccos\left(\frac{\mathbf{a}_1 \cdot \mathbf{c}}{|\mathbf{a}_1| \cdot |\mathbf{c}|}\right) = \arccos\left(\frac{n_1 + n_2/2}{\sqrt{n_1^2 + n_1 n_2 + n_2^2}}\right). \tag{4.3}$$

One distinguishes between achiral and chiral tubes, where the former have $\theta = 0$ or 30° and are called zig-zag and armchair tubes, and the latter have chiral angles somewhere between 0 and 30°[70]. A nanotube's periodicity along its axis is determined by the shortest graphene lattice vector perpendicular to the nanotube

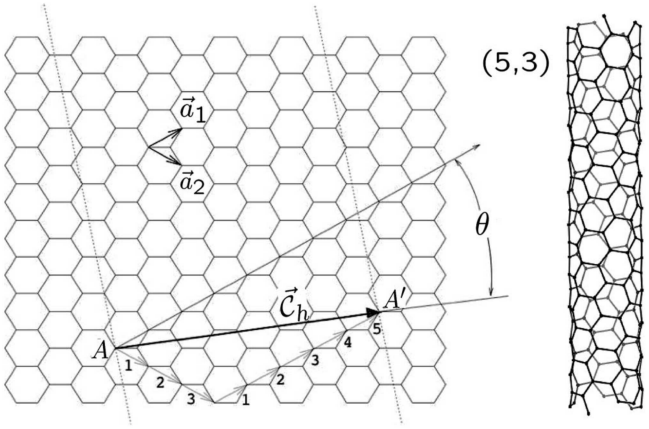

Figure 4.1: The chiral vector **c** and the chiral angle θ of a (5,3) nanotube (left) and its atomic structure (right). Figure taken from Ref.[71].

chiral vector. This vector is called the tube's translational period and can be calculated from the chiral indices:[70]

$$\mathbf{a} = -\frac{n_1 + 2n_2}{nR}\mathbf{a}_1 + \frac{2n_1 + n_2}{nR}\mathbf{a}_2, \tag{4.4}$$

where n is the chiral indices' greatest common divisor and R is 3 if the difference between the chiral indices $n_1 - n_2$ is divisible by 3 and 1 if not. The nanotube unit cell is given by the rectangle formed by the chiral vector and the translational period. It contains $n_{\text{hex}} = 2\left(n_1^2 + n_1 n_2 + n_2^2\right)/nR$ graphene unit cells and twice as many carbon atoms. The unit cell is much larger for chiral tubes than for achiral ones[70].

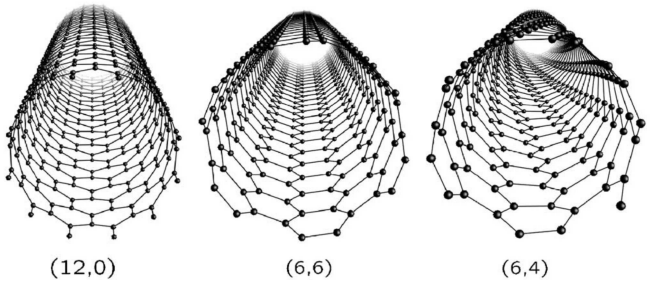

Figure 4.2: Atomic structure of a (12,0) zigzag tube, a (6,6) armchair tube, and a chiral (6,4) tube. Figure taken from Ref.[71].

4.1.2 Brillouin Zone

The electronic properties of carbon nanotubes are closely related to those of graphene. Specifically, the rolling-up of the graphene sheet imposes a quantization of the wavevector along the circumference of the nanotube. An approximation of the nanotube band structure can be obtained by evaluating the graphene band structure at the wavevectors allowed in the nanotube.

Mathematically, the quantization condition reads

$$\mathbf{k} \cdot \mathbf{c} = 2\pi m. \tag{4.5}$$

Here m is an integer that is referred to as the quasi-angular momentum quantum number and defines the wavevector perpendicular to the tube axis according to $k_{\perp,m} = 2m/d$. m can take values from $-n_{hex}/2 + 1$ to $n_{hex}/2$. The electronic wavefunction of a state with quasi-angular momentum m has $2m$ nodes along the nanotube's circumference. The wavevector along the nanotube axis is continuous (for an infinitely long tube) and the first Brillouin zone contains $k_z = \left(-\frac{\pi}{a}, \frac{\pi}{a}\right]$. The nanotube Brillouin zone thus consists of n_{hex} lines that are parallel to the k_z axis and separated by a distance of $2/d$. In armchair tubes, k_z is along the Γ-K direction in graphene, in zig-zag tubes it is parallel to Γ-M and in chiral tubes the direction is in between.

4.1.3 Electronic Structure

As a useful approximation to investigate the electronic structure of carbon nanotubes in dependence of their chirality, we can evaluate the graphene band structure along the lines of allowed wavevectors in the nanotube. This approach is referred to as zone-folding and takes into account the quantization of the wavevector but neglects the tube curvature[70]. Since in the graphene band structure valence and conduction band meet only at the K points, the zone-folding approximation yields a simple condition to determine if a tube chirality is metallic or not: if the wavevectors allowed in the nanotube include the K point, the tube is metallic, otherwise it is semiconducting. Mathematically the condition for metallic character is that $n_1 - n_2$ has to be a multiple of three[70,72].

The wavevector line in metallic nanotubes that includes the K point leads to linear one-dimensional bands with the same slope as the Dirac cone in graphene. All other lines lead to sets of valence and conduction bands that have extrema where the line is closest to the K point. We can use the zone-folding approach to investigate the dependence of the transition energies between these band extrema on the tube chirality. This dependence is best visualized in the so-called Kataura plot, which plots the transition energies as a function of tube diameter. At increasing energies, there are two groups of transitions in semiconducting tubes (referred to as S_{11} and S_{22}) followed by one group of transitions in metallic tubes (M_{11}). Within a group, the transition energy decreases with increasing diameter following $1/d$. There are further systematic variations that are explained for instance in Ref. [70].

4.1.4 Vibrational Properties

Similarly to the electronic properties in the preceding section, the vibrational properties of carbon nanotubes can also be derived from the graphene phonon dispersion by evaluating it at the wavevectors allowed in the nanotube. As the graphene phonon dispersion contains three optical and three acoustic phonon branches and there are n_{hex} lines of allowed wavevectors in the nanotube, the

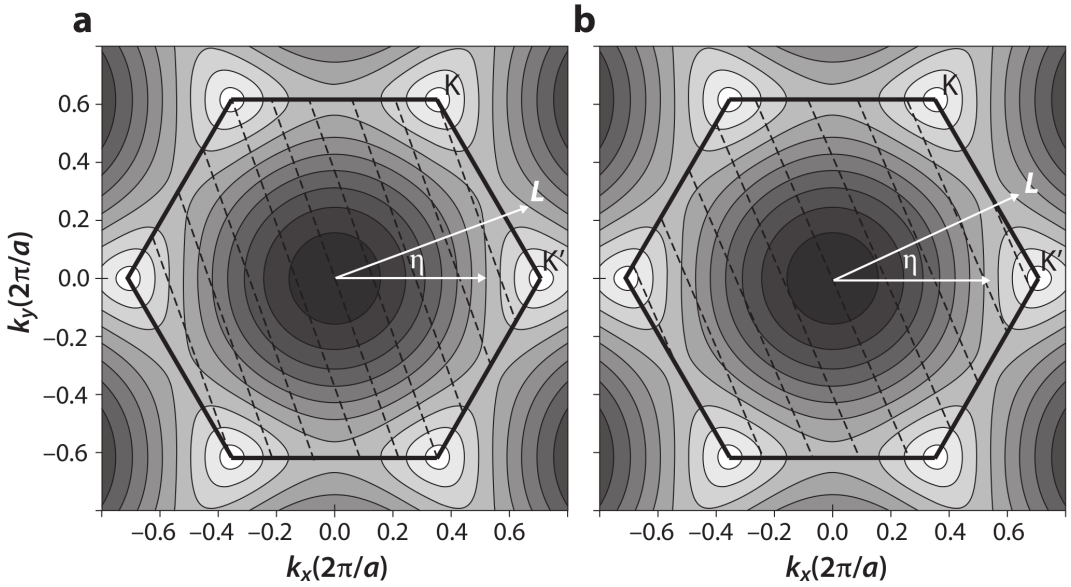

Figure 4.3: Reciprocal space structure of metallic and semiconducting carbon nanotubes. The hexagon is the graphene Brillouin zone and the background shows a contour plot of the graphene valence band with white corresponding to the lowest energy. The dashed lines are the lines of allowed wavevectors in the nanotube. They include the K point in the metallic tube on the left and do not include the K point in the semiconducting tube on the right. The nanotube chiral vector and chiral angle are called L and η in this figure. Figure taken from Ref. [73].

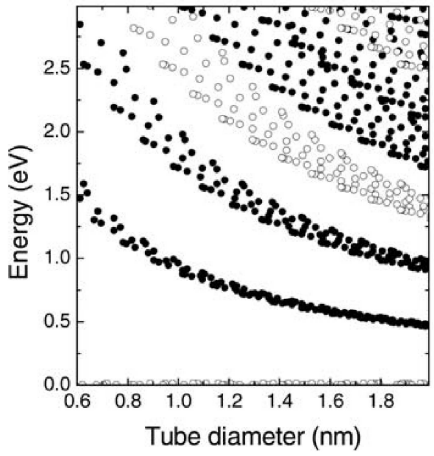

Figure 4.4: Carbon nanotube transitition energies for metallic (open symbols) and semiconducting (closed symbols) tubes. There are two groups of semiconducting transitions before the first group of metallic transitions. The energies were calculated from third-nearest neighbor tight-binding. Figure taken from Ref. [45].

nanotube phonon band structure contains $6n_{\text{hex}}$ bands in total. The phonon modes at Γ ($k_z = 0$) in the nanotube for wavevector lines with $m \neq 0$ can be said to be folded onto Γ by the wavevector quantization. In principle these additional Γ point modes could be observable in Raman scattering, but in practice the number of observable modes is strongly reduced by selection rules and the so-called antenna effect. The latter refers to the screening of electric fields perpendicular to the tube axis, which suppresses Raman processes with photons of these polarizations. The selection rules impose that the quasi-angular momentum m has to be conserved in the Raman process. As m is not changed upon absorption or emission of a photon with polarization along the tube axis, the phonon scattering step in the Raman process is also limited to $m_{ph} = 0$ [70].

In first order Raman processes, we can thus observe the $m_{ph} = 0$ phonon branches with q also 0. There are three such modes in every nanotube chirality: the radial breathing mode (RBM) and the longitudinal and transversal tangential modes. All three have A_1 symmetry in chiral nanotubes and A_{1g} symmetry in achiral nanotubes.

In analogy to the electronic properties, the detailed properties of the Raman-active phonon modes also depend on the nanotube chirality. For the radial breathing mode, which appears between about 100 and 400 cm^{-1}, the frequency is inversely proportional to the tube diameter [74]. In the following chapters we will focus on the longitudinal and transversal tangential modes, also called high-energy modes. These have more pronounced variations with tube chirality, in particular their properties are different in metallic and semiconducting tubes.

In metallic tubes, the longitudinal optical (LO) branch at Γ is affected by a Kohn anomaly [75]. This leads to a downshift of the phonon frequency at charge neutrality, which can be lifted by changing the Fermi energy. There is also peak broadening because the phonon can decay into electronic excitations across the Fermi energy in the linear metallic bands. We have also mentioned these phenomena and explained their origins in the section on the Raman spectrum of graphene, but their magnitude is greater in metallic nanotubes. As a result, the LO mode in metallic tubes appears around 1560 cm^{-1} with a width of greater than 50 cm^{-1}, which further depend on the diameter. By contrast, in metallic carbon nanotubes the transversal optical branch is not affected by the Kohn anomaly. It thus appears as a much narrower peak (FWHM of around 10 cm^{-1}) at frequencies around 1590 cm^{-1} [21,75].

In semiconducting nanotubes, there is no Kohn anomaly due to the absence of the linear metallic bands, so the LO mode appears as a narrow peak at 1592 cm^{-1}. The TO mode is downshifted because the bonds along the circumference are weakened due to the tube curvature and appears as a narrow peak around 1560 cm^{-1} [21,75]. Example spectra of the high-energy modes for semiconducting and metallic tubes are shown in Fig. 4.5.

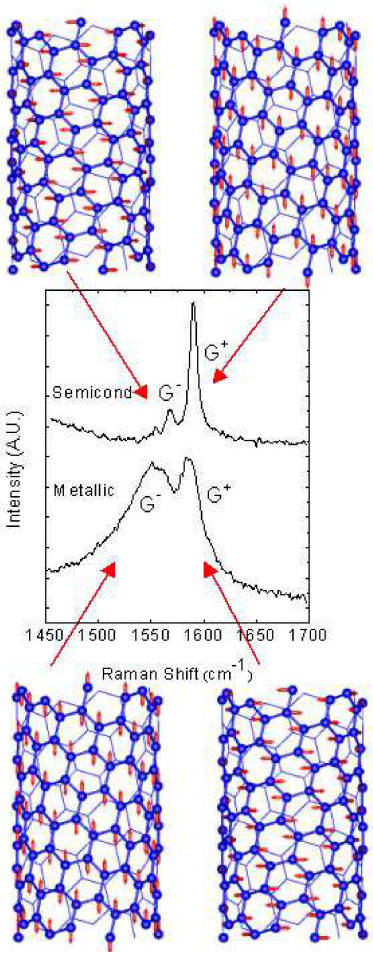

Figure 4.5: Raman spectrum of the carbon nanotube high-energy modes. The atomic displacement patterns are: semiconducting TO (top left), semiconducting LO (top right), metallic LO (bottom left), and metallic TO (bottom right). Figure taken from Ref. [75].

4.2 Experimental Methods

The sample investigated in section 4.4 is an enriched sample produced using size exclusion chromatography by gel filtration (Fraction 7 of Ref. [76]) with the starting nanotube material produced by pulsed laser evaporation (PLV). The semiconducting species are enriched in the (14,1), *etc.* branch; the sample has a narrow diameter distribution centered at 1.1nm. The tubes are suspended in aqueous solution with sodium cholate and a residual amount of sodium dodecyl sulfate as surfactants. The sample on silicon was prepared by depositing a single drop on a Si/SiO_2 wafer with a 300nm oxide thickness and letting it dry in air.

The laser spot illuminates ensembles of nanotubes in both the solution-based and the substrate supported samples. The spectra reflect the average Raman response of many different nanotubes. We verified the homogeneity of the deposited sample by taking multiple spectra at various positions.

The four samples used in section 4.5 are as follows. Sample 1 contains HiPCO

tubes in aqueous solution with SDBS as the surfactant without any enrichment and a broad diameter distribution. Sample 2 is an enriched HiPCO sample produced using gel chromatography[76] with SDS as the surfactant. Its photoluminescence excitation map shows (12,1), (11,3), (10,5), (11,1), and (10,2) tubes. Sample 3 is enriched in a similar fashion and also has HiPCO tubes with SDS as the surfactant, but features a narrower chirality distribution, mainly (12,1) and (11,3) tubes. Sample 4 is not enriched and contains HiPCO tubes from a different batch than sample 1. The samples were deposited onto Si/SiO_2 substrates with a 300nm oxide thickness by simply casting a drop and letting it dry in air.

To prepare the energy transfer complexes studied in section 4.6, the hydrophobic dyes are introduced into the micelles and onto the tubes via micelle swelling as described in Ref.[29]. Consequently, there are no free dye molecules in the solution. We investigate three energy transfer complexes containing anthracene, pyrene, and α-quarterthiophene(a4T), formed with PLV single-walled carbon nanotubes.

For section 4.4, spectra were acquired with Dilor XY and XploRA spectrometers at wavelengths of 488, 633, 638, and 647nm. Spectra in solution and on substrates were recorded in micro-Raman backscattering configurations with 10x magnification objectives. The Dilor spectrometer uses a triple-grating subtractive monochromator and the XploRA features an edge filter to block Rayleigh-scattered light. Frequencies were calibrated using a Neon lamp.

Electrochemical measurements were performed using a 1:2.4 weight ratio mixture of $LiCl_4$ in poly(ethylene oxide) (PEO, molecular weight 400) as the electrolyte. The chemicals were mixed as-received from Aldrich in air. The nanotube sample was deposited on a mica slide covered with a 100nm Au layer and was used as the working electrode. An Ag/AgCl reference electrode (World Precision Instruments) and a silver wire acting as a counter electrode complete the electrochemical cell. We applied a gate voltage using a homemade voltage source that also monitored the current between the working and counter electrodes. This current did not exceed 2μA at gate voltages within a range of ±1.4V. Use of the polymer electrolyte is necessary because aqueous electrolytes are only stable within a 1.3V range. Outside this limited range, bubbles form in the electrolyte, rendering further measurements impossible.

In section 4.5, Raman spectra were recorded on a Horiba XploRA spectrometer with a 532nm laser and a notch filter. Spectra were calibrated using a neon lamp. Electrochemical Raman spectra were acquired from samples deposited from a solution onto a 100nm gold layer on a mica slide. An electrochemical potential was applied between the sample (working electrode) and a Ag/AgCl reference electrode using a homemade voltage source. The potential was swept from -0.9V to 1.2V. The electrolyte was a 1:2.4 weight ratio mixture of lithium perchlorate ($LiClO_4$) and poly(ethylene oxide) (PEO, molecular weight 400) and the electrochemical cell was completed with a silver wire acting as the counter electrode. There was no current flow between working and counter electrode in the potential range used in this work.

In section 4.6, Raman spectra were acquired on a Horiba XploRA spectrometer with 638nm laser excitation. For the electrochemical Raman measurements, the samples were dropcast from solution onto a gold-coated wafer to form the working

electrode. Trimethylpropylammonium bis(trifluoromethanesulfonyl)imide was used as the electrolyte. The electrochemical cell was completed by a Ag/AgCl reference electrode and a Ag wire counter electrode. Gate voltages between -1.1V and +1.1V were applied in steps of 0.1V using a homemade voltage source.

4.3 Author Contributions

The following works have been published in Refs. [77–79]. For these publications, I performed all measurements, analyzed the data, and wrote the manuscripts. Frank Hennrich, Manfred Kappes, Ralph Krupke, and Friederike Ernst provided samples. Kenichi Ataka and Joachim Heberle provided equipment and expertise for electrochemical measurements. The studies were conceived by Ralph Krupke and Stephanie Reich and designed by Sebastian Heeg, Stephanie Reich, Ralph Krupke and myself. All authors discussed the results and the manuscripts.

4.4 Fermi Energy Shift in Deposited Metallic Nanotubes

4.4.1 Introduction

The high-energy modes around 1600cm^{-1} (also called G modes) are a prominent feature of single-walled carbon nanotube (SWNT) Raman spectra. They comprise out-of-phase in-plane vibrations tangential (TO) and parallel (LO) to the nanotube axis. The exact frequency of the LO and TO vibrations depends sensitively on the metallic or semiconducting character of the tubes[76,80–82]. In semiconducting tubes, the TO mode is located at lower frequencies than the LO mode because of the nanotube curvature which softens the bonds along the circumference[75]. In metallic tubes the LO phonon is broadened and downshifted by the interaction of the phonon with low-energy electron-hole pairs that results in a Kohn anomaly[83–85]. The appearance of a broad peak at 1550cm^{-1} is generally taken as indicative of the presence of metallic tubes. Recent studies claimed the absence of such an LO peak in armchair metallic tubes[86,87], despite earlier reports to the contrary[88,89]. The study by Haroz et al.[86] stresses the advantage of ensemble measurements in solution over measurements on individual tubes on a substrate. It was argued that ensemble studies are less sensitive to variations on the single-tube level and changes of the local environment. The argument implicitly assumes that the Raman spectra of tubes in solution remains unchanged upon deposition. This is particularly important since nanotube chirality enrichment and selection is done on tubes in solution, whereas nanotube devices such as field effect transistors are constructed on substrates.

In this paper, we show that the Raman line shape of nanotubes in solution and after deposition on a substrate differs strongly in metallic tubes. We observe an upshift and narrowing of the metallic LO peak in solution compared to on silicon, while the HEM of semiconducting tubes remain unchanged. The drastic

changes are caused by Fermi energy shifts, lifting the Kohn anomaly. The shift amounts to 23cm^{-1} and leads to hole doping as we demonstrate by combined electrochemical Raman measurements.

4.4.2 Results and Discussion

Figure 4.6a shows HEM Raman spectra of ensembles of nanotubes in solution (blue trace) and after deposition on a silicon substrate (black trace) acquired with 647nm excitation. The spectrum in solution shows a higher-frequency peak at 1589cm^{-1} and a shoulder at 1577cm^{-1} with a full width at half maximum of 29cm^{-1}. One is tempted to assign the spectrum to semiconducting tubes with the typical dominating peak around 1590cm^{-1}. The spectrum measured under the same conditions on silicon, in contrast, is dominated by a broad and asymmetric low-frequency component at 1554cm^{-1} with a full width at half maximum of 42cm^{-1} (see Figure S3 in supporting information for a fit). This peak is clearly due to metallic LO vibrations.

A possible explanation for the change from semiconducting to metallic lineshapes upon deposition is a change in the optical transition energies. However, the RBM spectra in the two experiments are almost identical (see inset of Fig. 4.6a), verifying constant resonance conditions. Due to the narrow resonance windows of RBMs even tiny changes in the optical transition energies result in drastic changes of the relative RBM intensities in ensemble measurements[74]. The RBM data also allow identifying the tubes as the metallic (15,0), (14,2), (13,4), and (12,6) chiralities (2n+m=30 branch)[20,74].

For blue excitation the comparison between the two Raman spectra is qualitatively different. Here, the signal arises from semiconducting tubes and there are negligible differences between the spectra in solution and on silicon, as seen in Fig. 4.6b. We also examined the HEM spectra of a HiPCO sample (not shown) and observed similar downshifts and narrowing of the metallic LO peak upon deposition. The effects were of smaller magnitude and more difficult to detect. Furthermore, the 2D Raman line of the enriched sample shifts by 10cm^{-1} to smaller energies when depositing tubes on Si, in analogy to the HEM behavior.

The changes in the HEM spectra of metallic tubes in Fig. 4.6a are due to shifts in the Fermi energy upon deposition. The Fermi energy affects the metallic LO peak in three ways as summarized in Fig. 4.7. The metallic LO frequency is lower than in semiconducting tubes because of the Kohn anomaly at $\mathbf{q} = 0$ (Γ point)[50,90]. In a quasi-static picture the LO displacement leads to the opening of a periodic gap in a nanotube[91]. This band gap reduces the time-averaged total electronic energy, Fig. 4.7a. Less energy is required to excite the LO mode, resulting in a phonon softening. The Kohn anomaly was described more rigorously in DFT calculations[75,84] and in calculations of the phonon self-energy due to the electron-phonon interaction[83,92]. Second, the width of the metallic LO peak is affected by the Fermi energy. Under intrinsic conditions the LO phonon can decay into a low-energy zero-wavevector electron-hole pair in the two bands crossing at the Fermi energy[93], as shown as a green dashed arrow in Fig. 4.7b. This relaxation channel vanishes with a shift in Fermi energy. Thirdly, the metallic

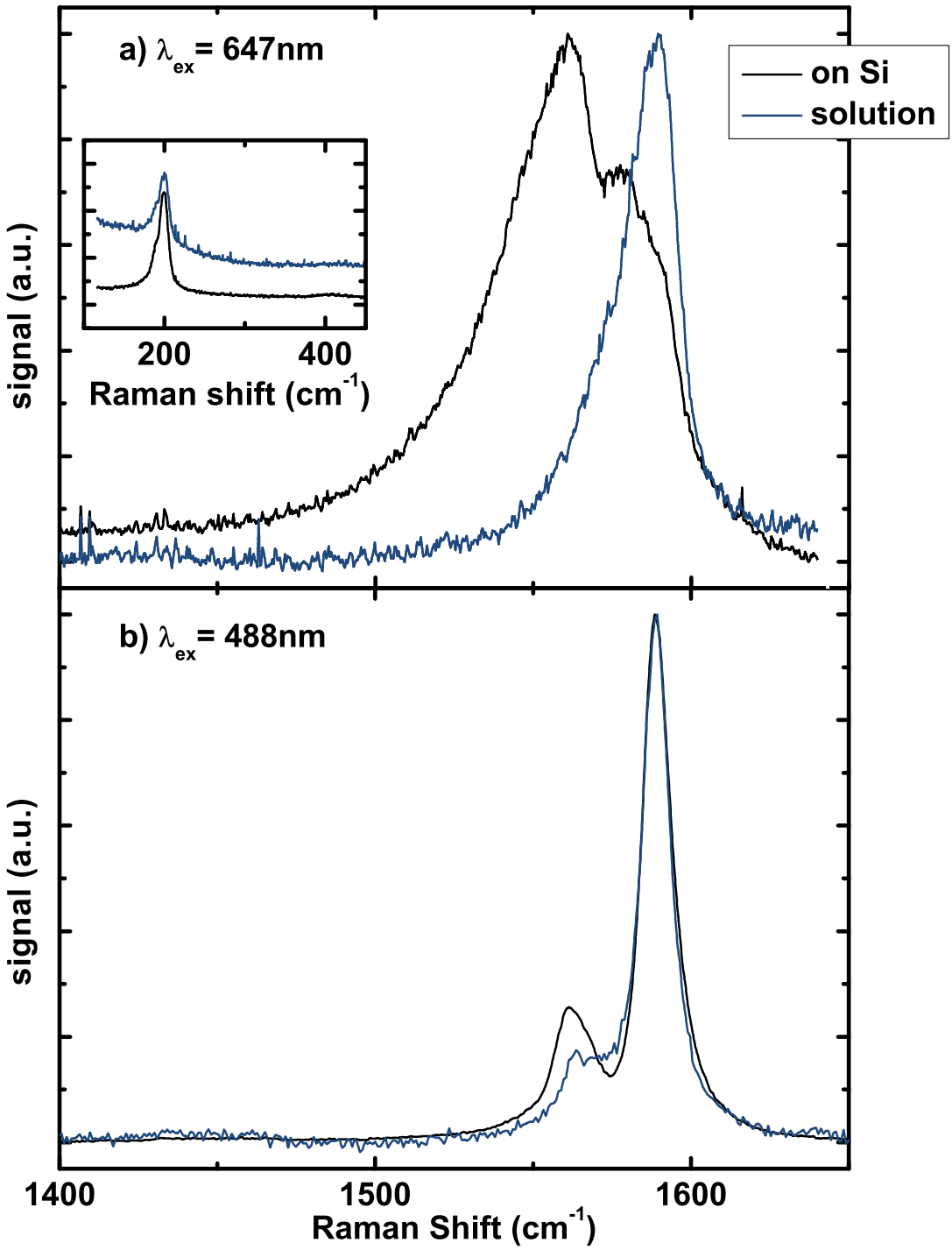

Figure 4.6: HEM Raman spectra recorded on ensembles of nanotubes in solution (blue trace) and on silicon (black trace) at wavelengths (a) 647 and (b) 488nm. The spectra at 647nm exhibit drastic differences as discussed in the text, while the spectra at 488nm are largely unchanged. The inset shows the RBM spectra at 647nm, which are very similar in solution and on silicon.

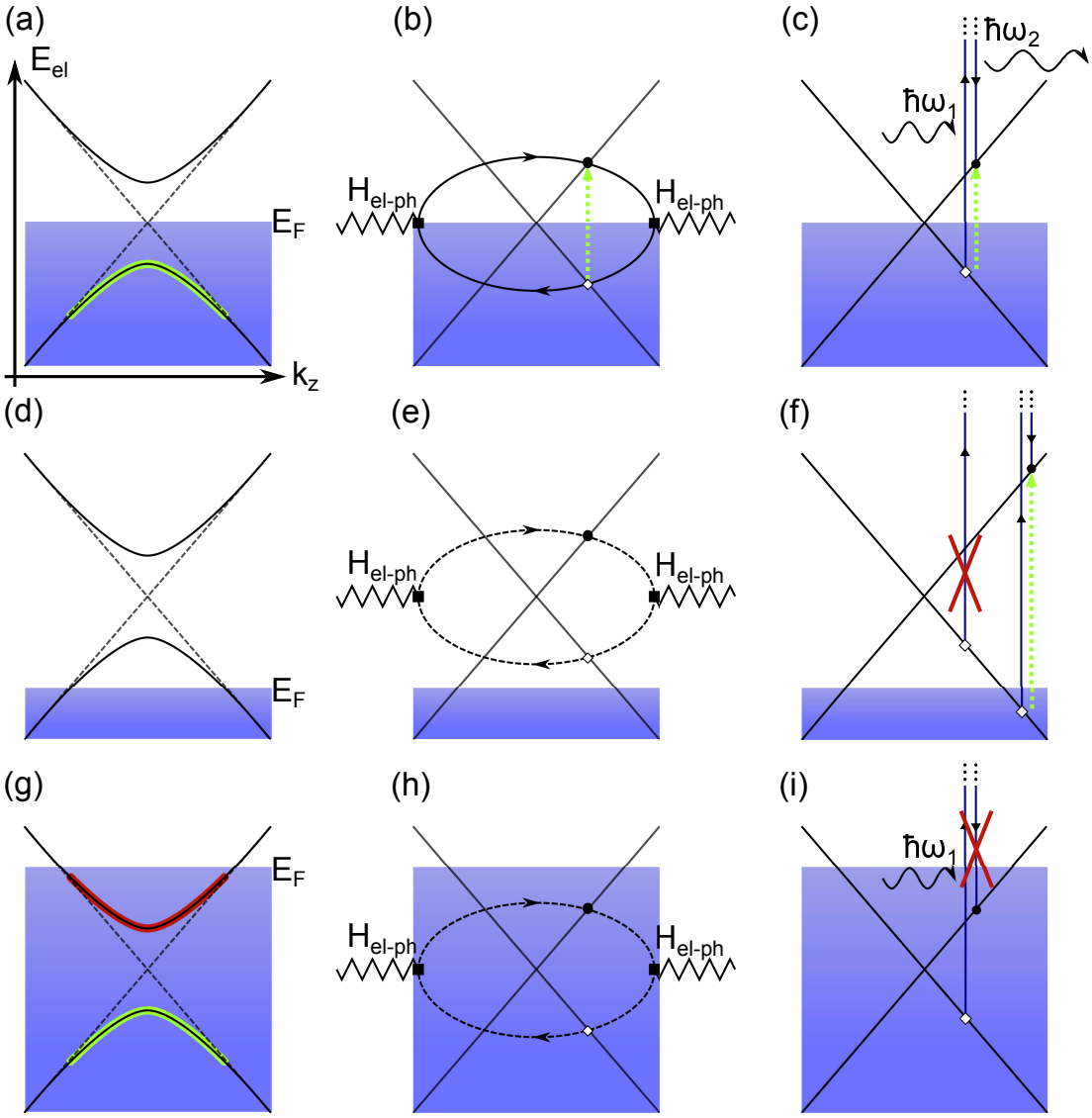

Figure 4.7: Effects of the Fermi energy on the HEM lineshape of metallic SWNTs at intrinsic Fermi energy (top row) and Fermi energies below (middle row) and above (bottom row) the band gap. The effects of a dynamic band gap (solid black lines, intrinsic band structure shown as gray dashed lines) on the energy of the electronic system is shown in (a), (d), and (g). Occupied states that are moved to lower (higher) energies are highlighted in green (red). (b), (e), and (h) show the Feynman diagrams for the phonon self-energy due to the electron phonon interaction. This self-energy includes the resonant decay of the phonon into a zero-wavevector electron-hole pair at intrinsic Fermi energies (green dashed line). At non-intrinsic Fermi energies the decay channel is blocked. The electronic Raman process that competes with the LO pathway and leads to the asymmetric lineshape is shown in (c), (f), and (i). The Raman processes are also blocked at non-intrinsic Fermi energies.

LO peak at intrinsic Fermi energy exhibits an asymmetric lineshape and is fitted with Fano profiles. This is due to quantum interference between the discrete LO phonon and the continuous electronic Raman scattering process[94], the latter process is shown in Fig. 4.7c[52,53]. All three mechanisms depend sensitively on the position of the Fermi energy. They are blocked or not in effect when the Fermi energy is not at its intrinsic value (see second and third row in Fig. 4.7).

We assign the lower-frequency peaks of Fig. 4.6a in solution and on silicon to metallic LO phonons. The LO in solution is higher frequency, narrower, and more symmetric because the Fermi energy is shifted from its intrinsic value. The downshifted, broad, and asymmetric metallic LO peak on silicon is characteristic of metallic tubes with intrinsic Fermi energies. Quantitatively, the metallic LO shift has a magnitude of 23cm^{-1} and the full width at half maximum changes by 13cm^{-1}.

To confirm our interpretation and quantify the position of the Fermi energy we performed *in-situ* electrochemical Raman measurements[89,95,96]. HEM Raman spectra recorded with gate voltages ranging from -1.4 to 0V are shown in

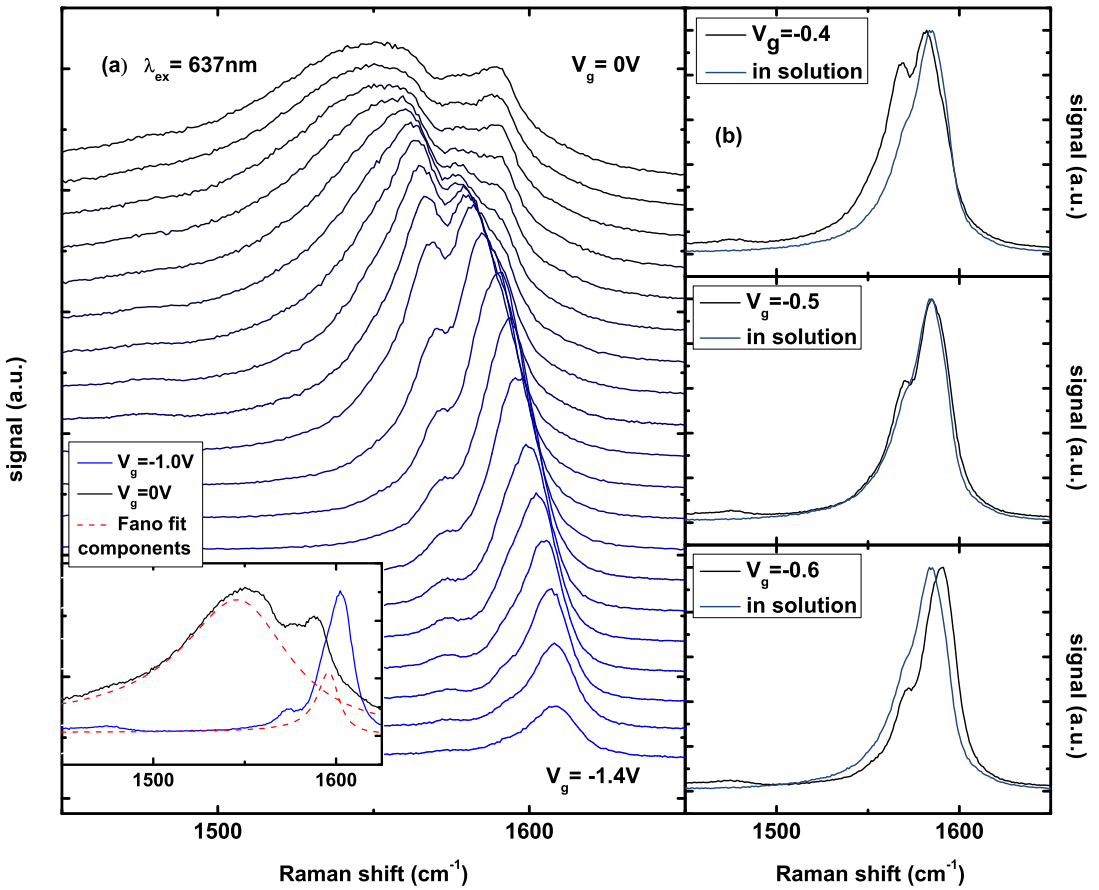

Figure 4.8: HEM Raman spectra acquired at 638nm under application of electrochemical gating. A gate voltage sweep from -1.4V to 0V is shown in (a). The inset shows two examples of the Fano fit component for gate voltages of 0V and -1.0V. The spectra acquired at gate voltages of -0.4, -0.5, and -0.6V are each compared to the spectrum in solution in (b). The lineshape matches at a gate voltage of -0.5V.

Fig. 4.8a. Negative gate voltages correspond to negative Fermi energy shifts, that is hole doping. Spectra acquired at positive gate voltages (electron doping) show similar behavior. The most obvious development in Fig. 4.8a is an upshift and a narrowing of the lowest-frequency metallic LO peak with increasing $|V_g|$. There is excellent agreement between the lineshape of the electrochemical spectrum at -0.5V and the spectrum recorded in solution, see Fig. 4.8b. We reproduce the spectrum in solution by deliberately shifting the Fermi energy, confirming our interpretation.

We now use the broadening of the metallic LO peak with gate voltage to calibrate the position of the Fermi energy. Figure 4.9a compares the experimentally observed peak width as a function of gate voltage with the theoretical dependence of the peak width on Fermi energy. The broadening decreases to half of its maximum value at Fermi energies of plus and minus half the phonon energy, that is ±0.1eV[83,97]. Experimentally the broadening is reduced to half of its maximum at -0.25 and +0.5V, see Fig. 4.9a. The rate of change of the Fermi energy with the gate voltage, or gating efficiency, is 0.2eV (the phonon energy) per 0.75V (voltage difference between crossing points) or 0.27eV/V, comparable to 0.4 - 0.7eV/V reported earlier[98,99]. The spectrum in solution, middle panel in Fig. 4.9b, corresponds to a Fermi energy shift $|\Delta E_F| = (0.16 \pm 0.03)$eV.

Next we determine the direction of the shift in Fermi energy by examining the 2D mode under electrochemical gating. Figure 4.9b shows the spectral development under negative (upper panel) and positive (lower panel) gate voltages. For negative gate voltages, the peak exhibits an upshift, whereas it exhibits a downshift by a smaller absolute magnitude for positive gate voltages. This asymmetry of the 2D mode with the sign of the Fermi energy shift is due to changes in the resonance conditions; it allows us to determine the direction of the Fermi energy shift. As the 2D peak in solution is higher in frequency than on a substrate, the Fermi energy in solution is below its intrinsic value, corresponding to hole doping. The position of the Fermi energy in solution is therefore $\Delta E_F = -(0.16 \pm 0.03)$eV below the band crossing point. The spectrum recorded on silicon exhibits a metallic LO peak. Nevertheless following the same arguments as for tubes in solution electrochemical measurements reveal $\Delta E_F = -(0.07 \pm 0.02)$eV.

We now discuss possible explanations for the positions of the Fermi level. Strano et al.[100] investigated the effects of changing the pH value of a SWNT solution on the HEM lineshape. They found that metallic tubes protonate at pH around 5, which leads to a withdrawal of electrons. They observed an upshift of the metallic LO peak after protonation. Strano et al.[100] also demonstrated that the surfactant shifts the pH value at which tubes protonate to more neutral values. A slightly acidic pH in our solution would thus explain the Fermi energy shift we observe in our sample.

After deposition, the Fermi energy continues to be below the intrinsic value. P-type behavior was observed in nanotube and graphene field-effect transistors on Si under ambient conditions in many studies[101–104], and attributed to ambient oxygen. This agrees with our results. Gaur and Shim[105] found a narrowing and upshift of the LO peak in metallic nanotubes under ambient conditions compared to after argon annealing. They ascribed the behavior to non-intrinsic positions

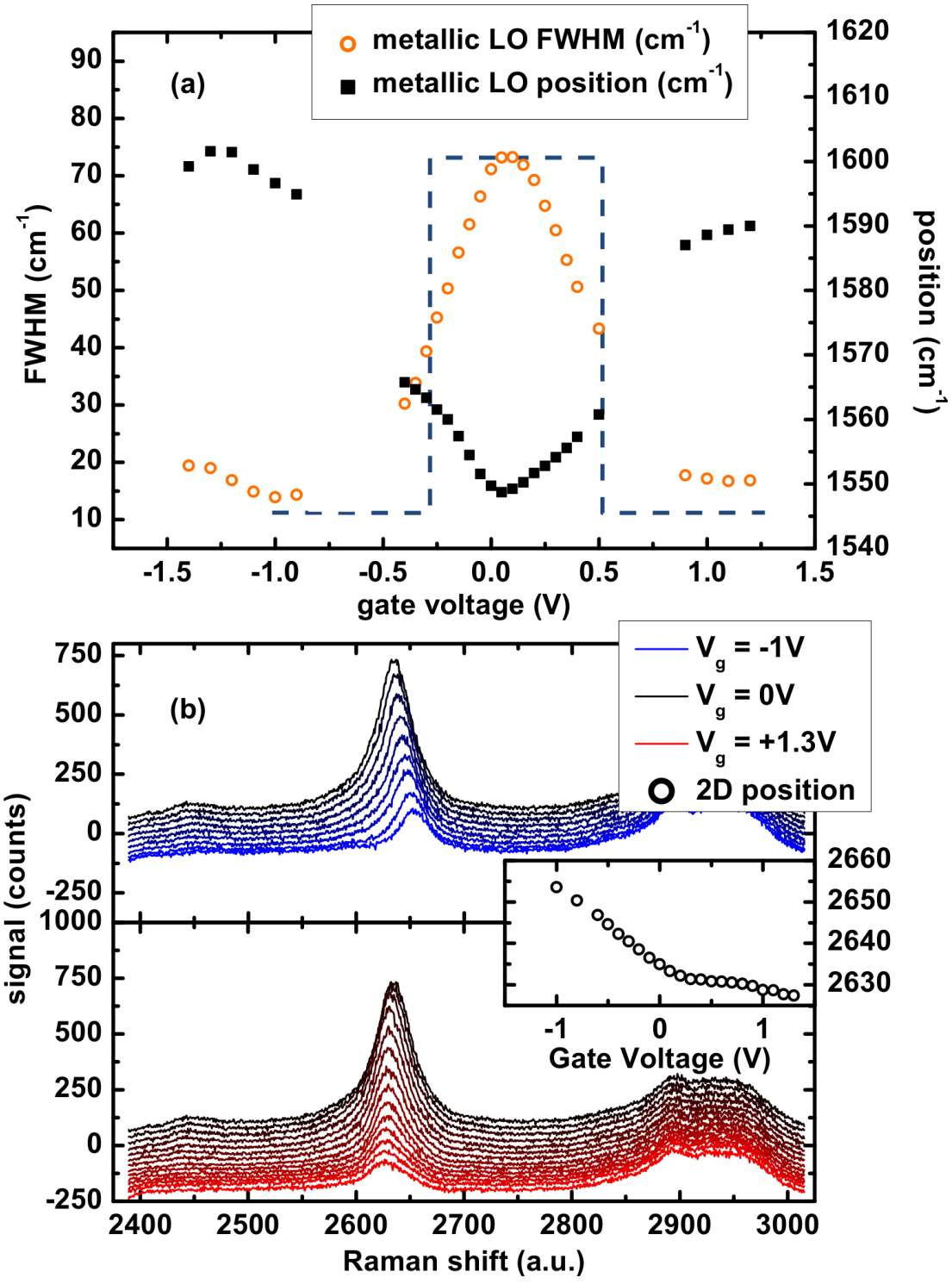

Figure 4.9: (a) Linewidth (left axis) and peak position (right axis) of the metallic LO peak as a function of gate voltage together with the theoretical prediction for the phonon linewidth at 0K without electronic broadening. The intersections at half of the maximum broadening occur at Fermi energy shifts of $\pm\hbar\omega_{ph}/2$. (b) 2D Raman spectra acquired at negative (top panel) and positive (bottom panel) gate voltages. The spectra at negative voltages exhibit a progressive upshift, while the spectra at positive voltages exhibit a downshift of smaller magnitude. The 2D peak position as a function of gate voltage is plotted in the inset.

of the Fermi energy under ambient conditions due to oxygen adsorption - in agreement with us - but failed to determine the sign and magnitude of the energy shift.

4.5 Raman Spectra of Metallic Carbon Nanotubes in Solution and on Substrates

4.5.1 Introduction

Carbon nanotubes have generated enormous research interest in the past years for their potential in a wide range of applications. Examples include integration in transistors[106] and gas sensors[15] as well as biomedical applications[107]. Raman spectroscopy is a well-established non-destructive technique for characterizing carbon nanotube samples. It yields information such as nanotube diameter, chirality[20], semiconducting or metallic character[21], defect concentration[22] and more.

The longitudinal optical (LO) phonon mode exhibits particularly interesting behavior. In this mode, which appears around 1600cm^{-1} as part of the G mode, the atoms oscillate out of phase in the direction of the nanotube axis. The metallic LO Raman peak is downshifted and broadened compared to the same peak in semiconducting tubes. These observations stem from an interaction between the LO phonon and electronic excitations between the linear bands crossing at the intrinsic Fermi energy in metallic tubes. The downshift and broadening are explained in terms of a Kohn anomaly[75] and an additional phonon relaxation channel[93], respectively. Both the downshift and the broadening depend critically on the Fermi energy, which determines whether the electronic excitations between the linear bands are possible. The two mechanisms are in effect when the Fermi energy is close to its intrinsic value and lifted when the Fermi energy is shifted by a value of more than half the phonon energy (100meV)[85,97].

In a previous study, we investigated the behavior of the metallic LO mode in a highly enriched sample in solution and after deposition on a Si/SiO_2 substrate[77]. We observed an upshift and narrowing of the metallic LO peak in solution compared to on the substrate. This behavior was explained in terms of a Fermi energy shift to 160meV below the intrinsic value in solution, which turns off the Kohn anomaly and the additional relaxation mechanism.

In this study, we extend our previous work and characterize four different carbon nanotube samples with varying degrees of enrichment. We find that the upshift and narrowing of the metallic LO peak in solution is not an isolated incident, but a general behavior that occurs in all the samples investigated in this study. We quantify the Fermi energy shift in one of the samples by using *in-situ* electrochemical Raman measurements. The results have implications for all spectroscopic studies that are performed on nanotube samples in solution.

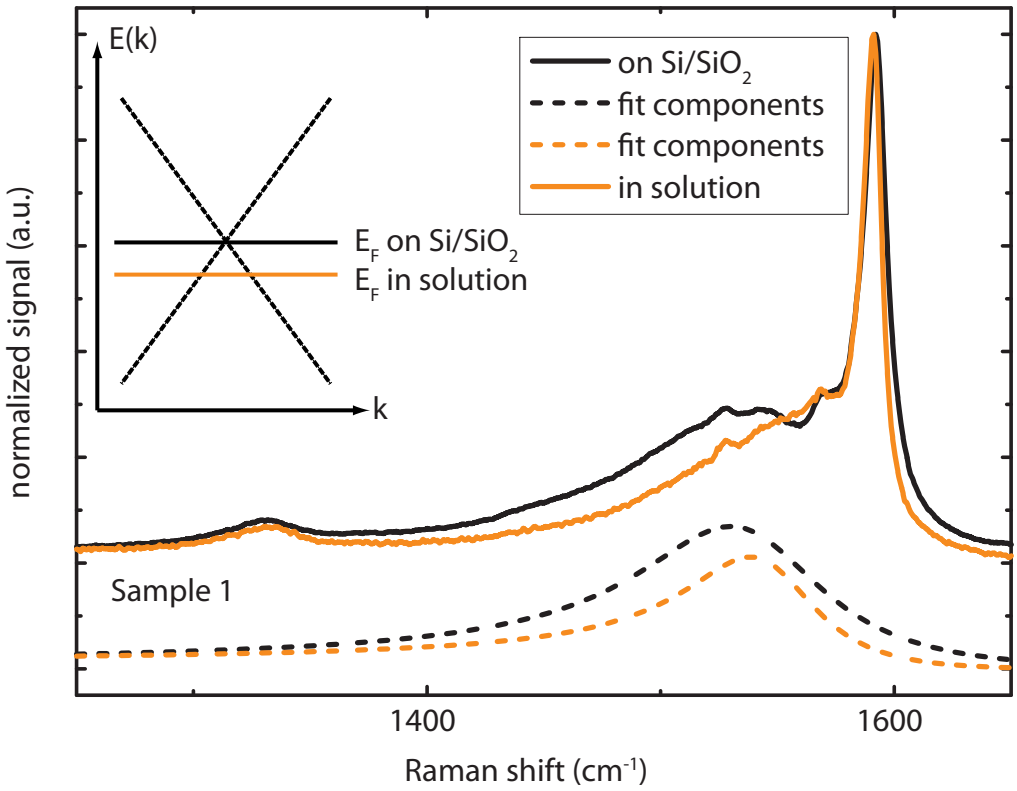

Figure 4.10: G mode Raman spectra of sample 1 in solution (orange solid line) and on a Si/SiO_2 substrate (black solid line). The dashed lines below show the metallic LO fit component, which is upshifted and narrower in solution. The inset schematically depicts the position of the Fermi energy in solution and on Si/SiO_2.

4.5.2 Results and Discussion

Figure 4.10 shows normalized Raman spectra measured on sample 1 using an excitation wavelength of 532nm in solution (orange solid line) and after deposition on a Si/SiO_2 substrate (black solid line). Metallic tubes are excited at this laser wavelength and give rise to the broad peak at about $1550cm^{-1}$. There is a noticeable difference between the spectra in solution and on the substrate, with a weaker signal at lower Raman shifts in solution. To gain quantitative information about this observation, we fit the experimental data using a Lorentzian peak for the D mode, a Fano lineshape[108] for the lowest frequency G peak, and two Lorentzian peaks for the semiconducting contributions. The resulting metallic LO peaks are shown as dashed orange and black lines below the experimental spectra in Fig. 4.10. The metallic LO peak is upshifted by $8cm^{-1}$ from $1538cm^{-1}$ to $1546cm^{-1}$ and narrowed by $14cm^{-1}$ from $49cm^{-1}$ to $35cm^{-1}$ in solution compared to the substrate.

We explain our observations with a shift of the Fermi energy away from its intrinsic value in solution, in agreement with our previous study[77]. Due to this Fermi energy shift, the Kohn anomaly is lifted and the additional phonon

relaxation channel is blocked, resulting in the narrower and upshifted metallic LO peak. The position of the Fermi energy is schematically depicted in the inset of Fig. 4.10.

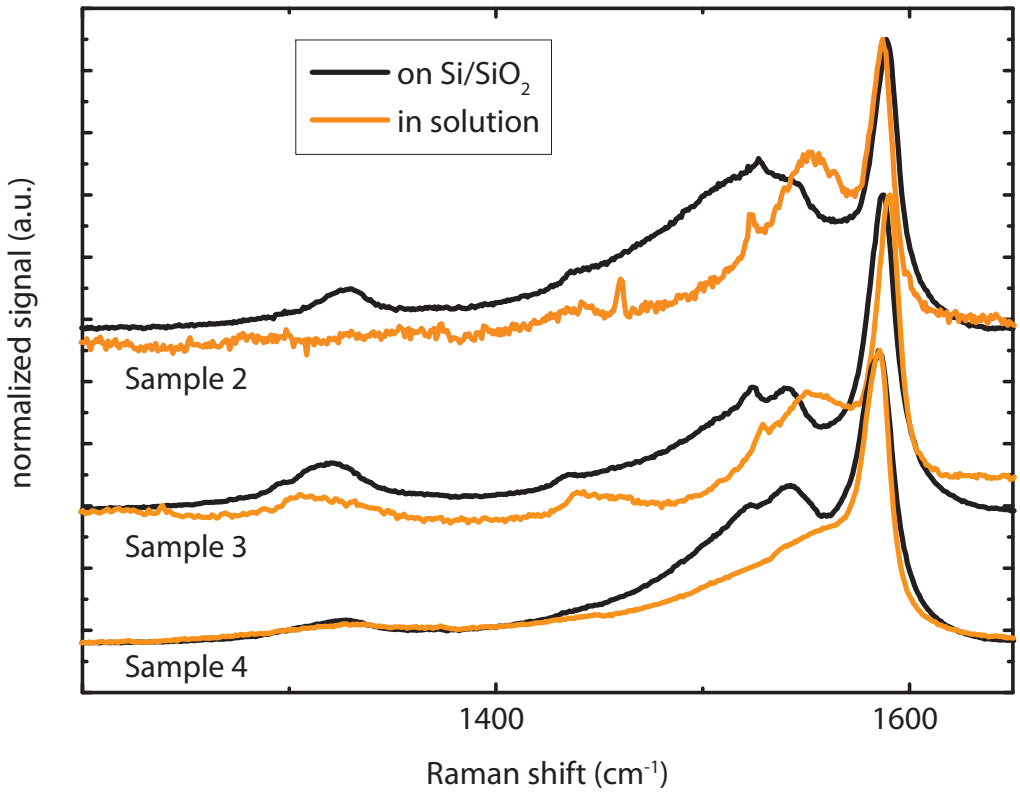

Figure 4.11: G mode Raman spectra of metallic tubes excited with 532nm in three other samples, all of which exhibit an upshifted and narrower metallic LO peak in solution.

The observation of a non-intrinsic position of the Fermi energy in a second sample is an indication that this might be a general behavior. This idea is reinforced by studying three further samples, for which Raman spectra are shown in Fig.4.11. The samples show varying behavior with respect to, for instance, the relative intensities of metallic and semiconducting signals. Compared to our earlier study[77], there is a larger residual contribution of semiconducting signal at the laser wavelength where the metallic signal is strongest in these samples. Furthermore, the absolute positions and widths of the metallic LO peaks in solution and on Si/SiO_2 also differ. However, all three samples have in common an upshifted and narrower metallic LO peak in solution compared to on Si/SiO_2, indicating that a non-intrinsic position of the Fermi energy, i.e. a charging of the nanotubes, is a general occurrence in solution.

We also fitted the spectra of samples 2-4 and extracted the metallic LO parameters. Figure 4.12 shows the metallic LO peak position (open circles) and

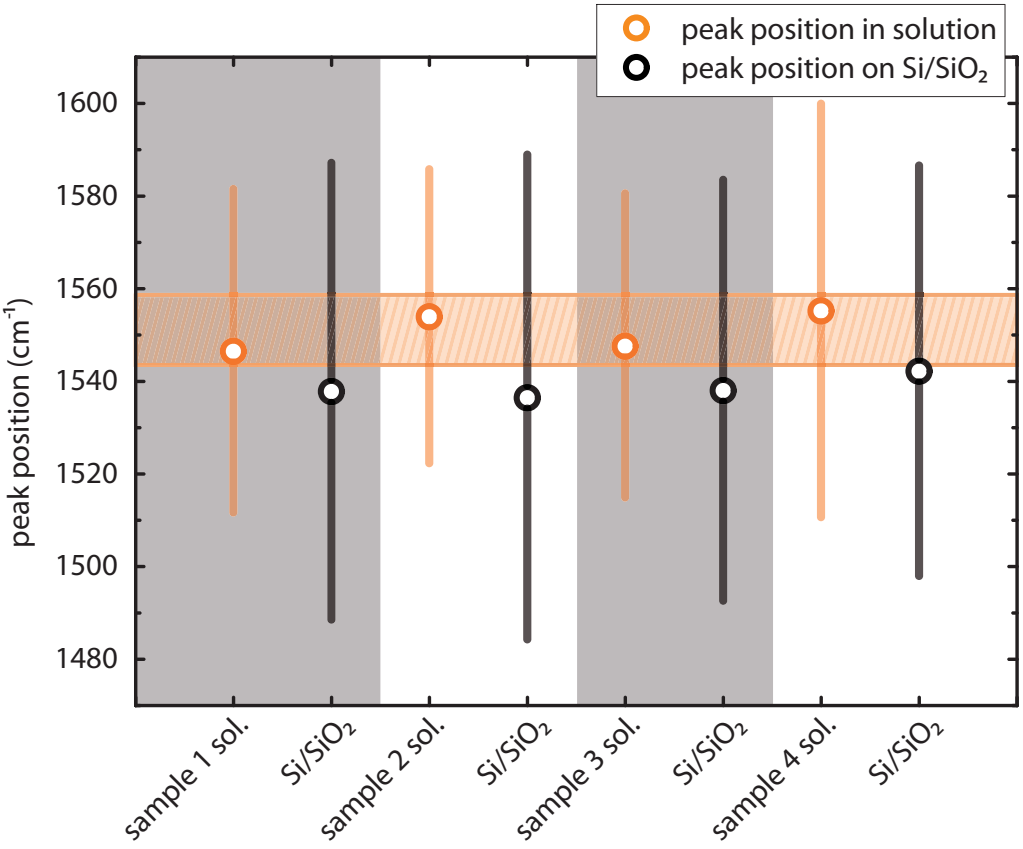

Figure 4.12: The peak position (open circles) and width (vertical lines) as extracted from the fits of the metallic LO component in all four samples in solution (orange) and on Si/SiO_2 (black). The peak is systematically shifted to higher Raman shifts and narrowed in solution relative to the behavior on the substrate.

peak width (vertical lines). The fact that the peak is upshifted in solution for all samples is also apparent in this plot: all the orange circles, corresponding to the spectra in solution, are above the black ones, which correspond to the spectra on Si/SiO_2. Additionally, the peak is narrower in solution for samples 1-3, while the peak width is unchanged for sample 4.

Having confirmed that Fermi energy shifts in solution are a common occurrence, we quantify the observed Fermi energy shift by performing *in-situ* electrochemical Raman measurements on sample 3. These measurements allow us to deliberately change the Fermi energy and observe the Raman response[89,95,109]. Figure 4.13 shows G mode spectra taken at gate voltages between 0 and -0.9V. Measurements at positive gate voltages show very similar behavior. However, the behavior of the 2D peak is asymmetric with gate voltage[110] and the behavior of the 2D mode in solution corresponds to negative gate voltages (data not shown). With increasing gate voltage, the metallic LO peak observed originally at about $1550cm^{-1}$ increases in frequency, decreases in width, and loses intensity. In the same gate voltage range the semiconducting LO peak at about $1590cm^{-1}$ retains its position and width and only decreases in intensity. These observations are in agreement with previous experiments[89,95,109] and the mechanisms outlined in the

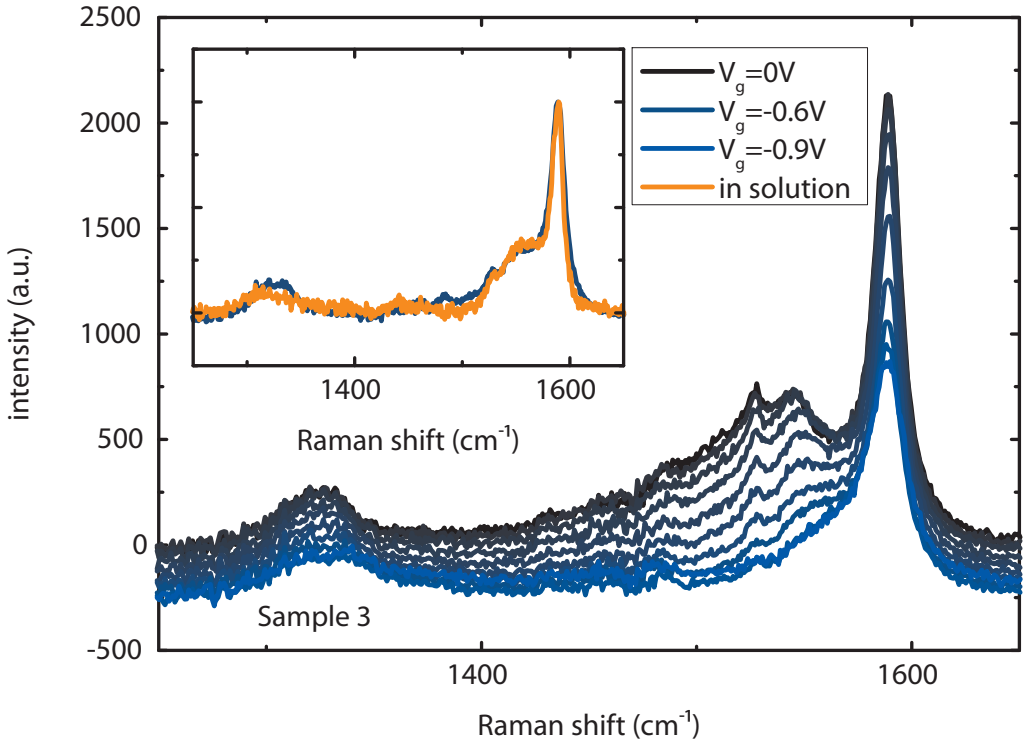

Figure 4.13: Electrochemical Raman spectra of sample 3 acquired at gate voltages between 0V and -0.9V. With increasing gate voltage, the metallic LO peak upshifts, narrows, and decreases in intensity. The inset shows a comparison between the spectrum in solution and the electrochemical Raman spectrum at -0.6V. The lineshapes match.

introduction, i.e. the Kohn anomaly and the additional phonon relaxation channel, both of which only exist in metallic tubes and are switched of at non-intrinsic Fermi energies. The spectrum in solution is reproduced at a gate voltage of -0.6V (see inset of Fig. 4.13), again confirming Fermi energy shifts as the explanation for our observations.

By fitting the electrochemical Raman spectra and plotting the metallic LO peak parameters as a function of gate voltage as seen in Fig. 4.14, we can compare our experimental data to the theoretical predictions. In particular, the metallic LO peak width is predicted to decrease to half of its maximum value at a Fermi energy shift of half the phonon energy, i.e. 100meV[97]. By observing at which gate voltage the peak width decreases to half and relating this to a Fermi energy shift of 100meV, we calibrate gate voltage to Fermi energy. We calculate that the gate voltage of -0.6V where the electrochemical spectrum matches the one in solution corresponds to a Fermi energy shift of -(200±30)meV. This is comparable with our previous result of -160meV[77]. Consequently, several 100meV appears to be a typical Fermi energy shift in nanotube solutions.

The observation of Fermi energy shifts or non-intrinsic charge densities in every one of the samples included in this study has implications for all spectroscopic methods probing nanotubes in solution. For Raman measurements, where

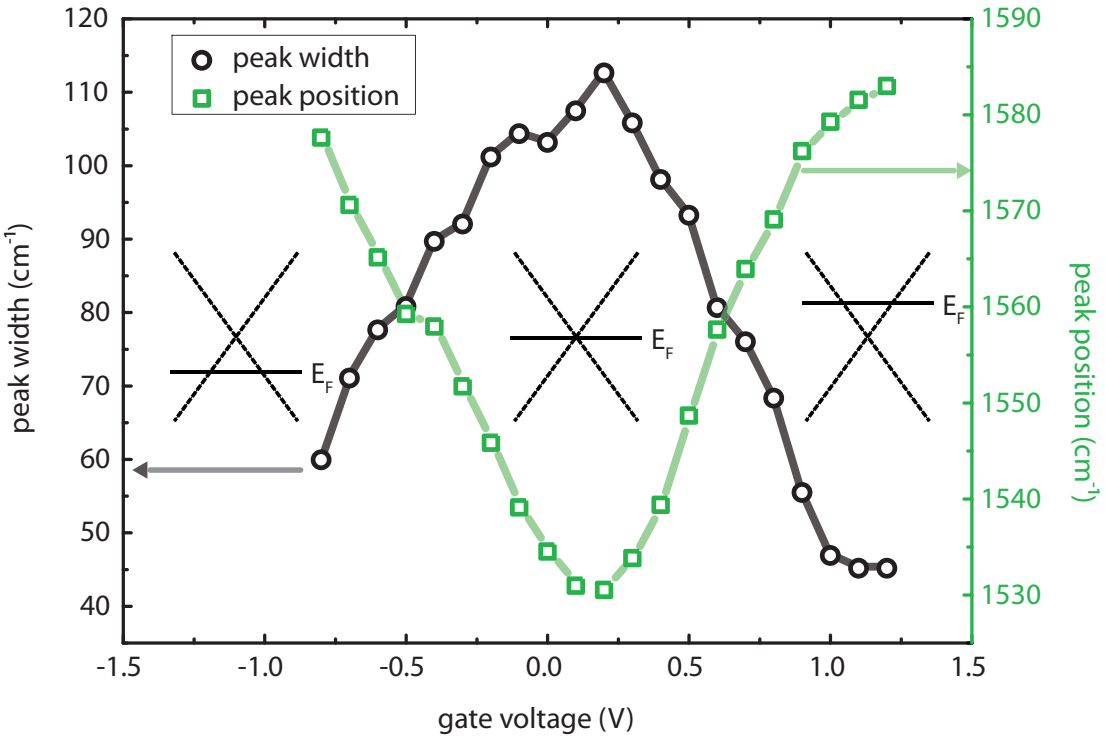

Figure 4.14: Peak position (black symbols, left axis) and full width at half maximum (green symbols, right axis) of the metallic LO peak as a function of gate voltage.

resonance profiles are commonly acquired in solution[111], the intensity is dependent on the Fermi energy. Furthermore, the Raman intensity decreases faster for metallic than for semiconducting chiralities[112]. It is therefore possible that the abundance of metallic tubes assessed by simply examining the G mode lineshape could be underestimated[77]. It has also been shown that the photoluminescence intensity decreases and the E_{33} electronic transition energy redshifts when the Fermi energy is shifted away from its intrinsic value[113]. Time-resolved spectroscopic experiments that are performed in solution[114] should also take into account the possibility of non-intrinsic Fermi energies. We plan additional further experiments to investigate the behavior of the metallic LO peak in solution, including measurements on tubes with anionic and cationic surfactants to see if the solutions Fermi energy shifts in different directions, as well as measurements on tubes in anorganic solvents.

4.6 Electrochemical Raman Spectroscopy of Carbon Nanotube Energy Transfer Complexes

4.6.1 Introduction

Single-walled carbon nanotubes have attracted enormous research interest because of their varied optical properties[115], excellent electronic transport characteristics[116], and potential biomedical applications[107]. Semiconducting nanotubes emit light at near-infrared wavelengths, in the biomedically relevant transparency window of tissue[117].

Nanotubes have low intrinsic absorption strengths and different chiralities require different excitation energies, which hinders imaging application. Carbon nanotube energy transfer complexes have recently been developed[28–33] to overcome these shortcomings. In these complexes, a dye featuring a higher intrinsic absorption strength is brought into proximity of the nanotube. After optical excitation of the dye, the excitation is transferred into the nanotube, and the nanotube emits light in the near infrared. The energy transfer efficiency reaches values that are very close to unity, meaning that almost every excitation created in the dye is transferred into the nanotube[28,30,32].

Spectroelectrochemical Raman measurements of carbon nanotubes have been used to investigate the electron-phonon coupling and the charge states of nanotubes in solution and on substrates. The metallic LO component of the G-mode lineshape is very sensitive to the Fermi energy, which can be changed by applying a gate voltage. The metallic LO peak exhibits a Kohn anomaly, which leads to a downshift of the peak compared to semiconducting tubes[51,75,83,84,91,95,97]. Furthermore, in metallic tubes there is an additional phonon relaxation channel consisting of electronic excitations between the linear bands crossing at the Fermi energy[93]. This additional phonon relaxation channel leads to a broader Raman peak. Both the Kohn anomaly and the phonon relaxation channel are only in effect at intrinsic Fermi energies and are lifted when the Fermi energy is shifted by half the phonon energy in either direction.

In this paper we conduct in-situ spectro-electrochemical Raman measurements on carbon nanotube energy transfer complexes formed using three different dye molecules and compare their behavior to that of a reference sample. We find that the energy transfer complexes exhibit different electrochemical charging characteristics such as a lower gating efficiency and shifted voltage position of the charge neutrality point. We also investigate the Fermi energy of complexes in solution and find that charge transfer between the constituents cannot explain the photoluminescence quenching observed previously for some of these complexes.

4.6.2 Results and Discussion

Figure 4.15 shows G-mode Raman spectra of the anthracene-carbon nanotube energy transfer complex acquired while sweeping the gate voltage from 0V to

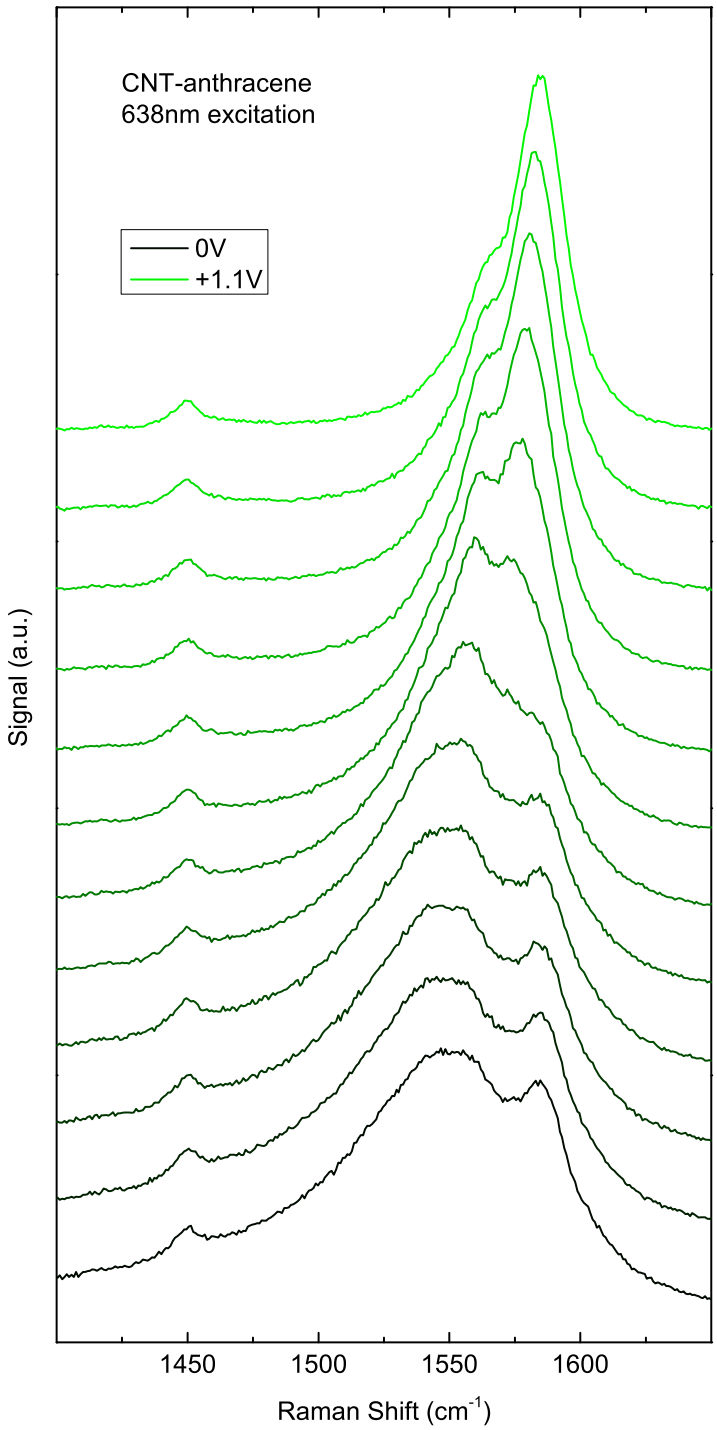

Figure 4.15: Electrochemical Raman spectra of the anthracene-carbon nanotube energy transfer complex acquired at gate voltages from 0V to +1.1V with 638nm laser excitation.

+1.1V. Spectra were also acquired at negative gate voltages. With increasing gate voltage, the metallic LO peak initially located at 1552cm^{-1} upshifts and narrows in accordance with established results on the Kohn anomaly and the additional phonon relaxation channel, which are lifted and blocked at non-intrinsic Fermi energies[93,95]. At the same time, the integrated peak intensity decreases. At larger gate voltages the semiconducting LO peak initially located at 1588cm^{-1} additionally up-shifts to higher frequencies.

We fitted the electrochemical Raman spectra with three peaks for the G-mode region and track the peak position and width (full width at half maximum) of the lowest-frequency fit component, which corresponds to the metallic LO peak. The same type of measurement and analysis was performed for the pyrene-carbon nanotube and a4T-carbon nanotube energy transfer complexes and the reference sample. Figure 4.16 shows the peak position and width as a function of gate voltage for all four samples.

Comparing the behavior of the three energy transfer complexes and the reference sample, we can make several observations: Firstly, the gate voltage at which the metallic LO peak exhibits the maximum width and minimum peak position is different for the different samples. This can be attributed to doping of the nanotubes by the dye molecules, which has to be countered by a certain gate voltage to achieve charge neutrality. The corresponding voltages are +0.1V for anthracene and -0.1V for pyrene and a4T. However, the spectrum of the reference sample also does not exhibit maximum broadening and minimum peak position at 0V, but instead at +0.1V.

Secondly, the rate of change of the width and position of the metallic LO peak, i.e. the gate efficiency, is slightly smaller for the anthracene and pyrene samples than the a4T and the reference samples. This means that is harder to induce a given charge density in the nanotubes in these samples, presumably due to the presence of the dye molecules in immediate proximity to the nanotubes. To quantify the gate efficiency, we observe the difference in gate voltage between the two points where the peak width reaches half its maximum value (e.g. +0.6V − (−0.4V) = 1V for anthracene). From theory we know that this corresponds to a change in the Fermi energy equal to the phonon energy, 200meV[83,84,97]. We thus arrive at a gating efficiency of 0.20eV/V for anthracene. The gate efficiency is 0.20eV/V for pyrene and 0.25eV/V for a4T and the reference sample.

Thirdly, the most pronounced difference is in the minimum width and and maximum peak position of the metallic LO peak obtained at high gate voltages. Here the values for the reference sample indicate significantly stronger doping than for the energy transfer complexes, leading to a lower peak width and higher peak frequency. This observation can be hypothesized to be due to the presence of the dye molecules between the electric double layer and the nanotube, which reduces the maximum capacitance of the nanotube-electrolyte interface. This leads to lower maximum charge densities. The maximum doping in the reference sample is greater than in all three energy transfer complexes, while the behavior among the energy transfer complexes is fairly similar. Specifically, the peak width and position at -1.1V are 16cm^{-1} and 1594cm^{-1}, respectively, compared to 32cm^{-1} and 1579cm^{-1} for anthracene. A comparison of the spectra at -1.1V is shown in

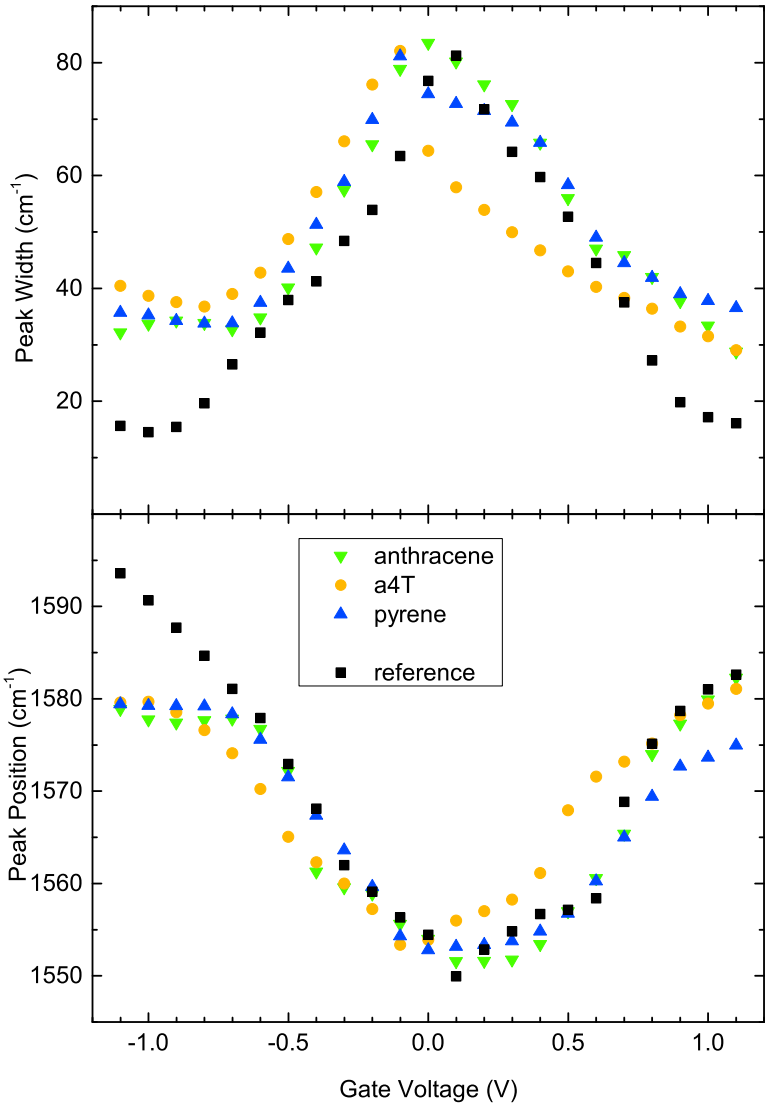

Figure 4.16: Peak width (full width at half maximum) and peak position of the metallic LO peak extracted from the fitted electrochemical Raman spectra as a function of gate voltage.

Fig. 4.17b.

It is interesting to note that the maximum peak width of 80cm^{-1} and the minimum peak position of 1550cm^{-1} of the metallic LO peak obtained at the charge neutrality point is very similar in all the samples, see Fig. 4.17a. This proves that the dye molecules do not introduce significant Fermi energy inhomogeneity in the tubes, as could have arisen from uneven coverage of the tubes. Fermi energy inhomogeneity would have manifested itself as a lower maximum peak width and higher minimum peak position because at a single gate voltage, not all the tubes would have been at charge neutrality.

Photoluminescence measurements on the carbon nanotube energy transfer complexes are typically carried out in solution. We therefore also compare Raman spectra of our samples acquired in solution to the electrochemical Raman spectra in order to assess the charge state of the nanotubes in solution, and in particular

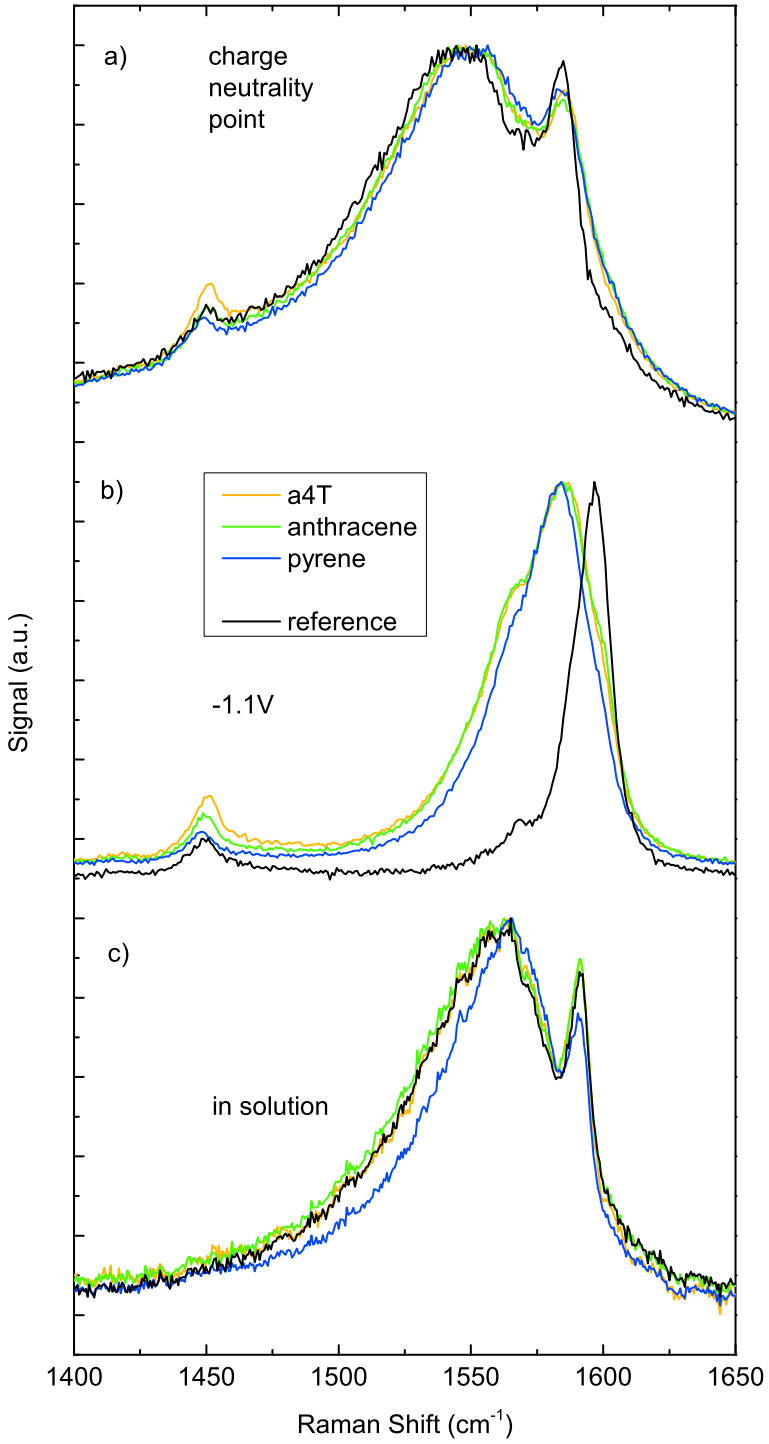

Figure 4.17: a) Spectra at charge neutrality showing a similar lineshape in all the samples. b) Spectra at -1.1V showing much larger doping strength for the reference sample than for the energy transfer complexes. c) Spectra in solution, from which the Fermi energy shifts were determined.

if the tubes are charged enough to quench their luminescence.

The G-mode Raman spectra in solution, shown in Fig. 4.17c, match the electrochemical Raman spectra taken at gate voltages of -0.3V for anthracene, -0.4V for pyrene and a4T, and -0.2V for the reference sample. We take the voltage difference between these values and the respective voltages of the charge neutrality point and convert them to Fermi energy shifts using the gate efficiencies determined earlier in this paper. This calculation gives Fermi energy shifts of 80meV for anthracene and pyrene and 75meV for a4T and the reference sample. These values are for the metallic tubes that contribute to the metallic LO peak.

Our measurements in this paper probe several metallic chiralities that contribute to the metallic LO peak in the spectrum together. By contrast the measurements in Ref.[29] probe various single semiconducting chiralities. It was found that a4T enhances the photoluminescence for all chiralities, by up to 100% for (11,1) tubes. Anthracene quenches the photoluminescence of all chiralties by around 20%, except for the (11,1) chirality, which gives about 90% enhancement. Pyrene quenches the photoluminescence for all chiralities, by 30% on average. We do not focus on the Raman signal of semiconducting tubes in this work because their G-mode peak position and width is affected much less by changing the Fermi energy than the G-mode of metallic tubes.

In our measurements we found the spectra in solution to correspond to electrochemical potentials at most 0.4V below the charge neutrality point. Assuming a charging efficiency of 1eV/V for semiconducting tubes inside the band gap, these values would not be sufficient to shift the Fermi energy into the valence band, at which point quenching was observed in the absorption in Ref.[118].

Regardless of whether the Fermi energy shifts would be strong enough to quench the absorption or luminescence, since the Fermi energy shifts are very similar to the reference sample for all three energy transfer complexes, charge transfer cannot be the explanation for the photoluminescence quenching and enhancement observed in Ref.[29]. The photoluminescence quenching can be attributed to a reduced radiative life time in the energy transfer complexes. The precise mechanism of the radiative life time reduction was not determined. A possible candidate is the extrinsic local modulation of the Fermi energy through the adsorbed dye molecules leading to increased scattering. This local modulation of the Fermi energy is not accessible in our experiments, which probe the average Fermi energy in an ensemble of nanotubes.

4.7 Conclusion

In summary, we have conclusively demonstrated two Fermi energy shifts in metallic nanotubes: Away from the intrinsic value in solution and back towards its intrinsic value after deposition on silicon. The shifts manifest themselves in a changing HEM lineshape of metallic tubes, with an upshift and narrowing of the metallic LO peak in solution. Electrochemistry allowed us to quantitatively determine the sign and magnitude of the observed Fermi energy shifts in solution (-0.16eV) and on silicon(-0.07eV). Our results have implications for the application

of Raman spectroscopy to estimate the fraction of metallic and semiconducting tubes in bulk nanotube samples because Fermi energy shifts might lead to the underestimation of the fraction of metallic tubes. Spectra are preferably acquired on silicon where the Fermi energy is closer to its intrinsic value and the metallic LO exhibits the characteristic downshift, broadening, and asymmetry. This is particularly recommendable for volume samples intended for electronic applications where the dominance of either semiconducting of metallic species is critical[119,120]. By investigating four additional samples, we have provided conclusive evidence that the discussed Fermi energy shifts are common occur

We furthermore performed electrochemical Raman measurements on the carbon nanotube energy transfer complexes. We found that the presence of the dyes influences the charging behavior of the nanotubes, as manifested in different positions of the charge neutrality point and reduced maximum doping strength. Furthermore, we examined the Raman spectra of the same complexes in solution and found that the Fermi energy has very similar values in all samples. This rules out charge transfer as the explanation for the different photoluminescence enhancement/quenching behavior of the different samples.

5 | Conclusion

I conclude this thesis by summarizing my findings and giving an outlook. I established a new method to determine the Fermi energy in doped graphene. The method relies on measurement of the optical reflectivity in the visible range and comparison to calculated spectra obtained by modeling the refractive index of doped graphene. The model for the refractive index of doped graphene employs the fact that for a given Fermi energy, the electronic transitions leading to the optical absorption of graphene are blocked up to energies of twice that Fermi energy, and the fact that the absorption is proportional to the imaginary part of the refractive index. I calculate the real part of the refractive index by Kramers-Kronig transform. This method allows me to determine the Fermi energy in my samples of potassium-doped graphene, where I find values of 1.3 eV for a graphene sample on Si/SiO_2 and 1.2 eV for a sample on hBN. These values are in agreement with results from ARPES.

I also presented a comprehensive Raman spectroscopy study on potassium-doped graphene. I monitored the time evolution during exposure to potassium vapor and observed the appearance of an additional Raman peak at lower frequencies than the G line that is observable while the G line is still present in the spectrum. After longer doping times, the G line disappears and the broad, asymmetric peak at about 1560 cm^{-1} for green excitation remains.

I demonstrated that the peak position, width, and asymmetry depend on laser energy, with the position increasing monotonously with increasing laser energy. The width and asymmetry exhibit maxima at laser energies of twice the Fermi energy. Additional measurements on multilayer graphene showed that the peak is remarkably independent of layer number, in contrast to the behavior of the Raman spectrum of pristine graphene of different layer number.

I furthermore employed polarization-resolved Raman spectroscopy with linear and circular polarized incoming light to investigate the symmetry of the peak in potassium-doped graphene. I find that it has mixed A_{1g} and E_{2g} symmetry.

The main finding from my Raman study on potassium-doped graphene is that the asymmetric peak observed around 1560 cm^{-1} is not the G line at very strong doping. I summarize the three pieces of evidence:

- The peak disperses with laser energy, which rules out single-resonant processes that lead to the G mode.
- The peak has A_{1g} and E_{2g} symmetry contributions as opposed to the pure E_{2g} symmetry of the G peak.

- It is impossible (in my measurements and those in Ref. [6]) to observe a transition between the G peak and the lower frequency Fano peak. Howard et al. attribute this to spatially inhomogeneous doping, but the observation is equally consistent with two peaks coexisting in a uniformly doped material. The Fano peak appears at lower doping strengths than those were the G mode disappears completely.

This means that the Raman behavior of potassium doped-graphene is different from any related material: pristine graphene, less strongly doped graphene, and bulk KC_8. The Raman peak I observe clearly stems from a resonant process and involves non-Γ point phonons. Invoking non-resonant Raman scattering only, there is no explanation for the observed dispersion with laser energy. Furthermore, the phonon in question is obviously affected by very strong electron-phonon coupling, similar to that described in the explanation of the 1510 cm^{-1} peak in KC_8, which results in the observed peak width.

As the theoretical calculations in Ref. [9] predict different superconductivity transition temperatures for lithium and calcium intercalated graphene, it would be interesting to also study these intercalants by Raman spectroscopy. Ultimately it would desirable to know to what extend the differences between the superconducting properties of the bulk and monolayer samples of the different intercalation compounds are mirrored in the differences between the bulk and monolayer Raman spectra. I have already shown that the latter are quite strong for potassium intercalation. Apart from the above-mentioned phonon Raman scattering, it has been shown in Ref. [59] that in CaC_6 below the superconducting transition temperature, there is a cutoff in the background arising from electronic Raman scattering. The position of this cutoff in CaC_6 is at about 24 cm^{-1} and is very similar to other measurements of the energy gap.

Low-temperature Raman measurements could thus also be used more directly to investigate superconductivity in intercalated monolayer graphene. Measurements of the position of the cut-off in the electronic Raman scattering background in monolayer and bulk intercalation compounds and for different intercalants would allow the determination of the energy gap and the critical temperature without the need for electronic transport or SQUID measurements. The necessary observation of a spectral region very close to the Rayleigh-scattered light should be possible using a triple-monochromator system (as used in Ref. [59]). The introduction of a sealed ampoule containing monolayer intercalated graphene into a cryostat may be more challenging.

In the set of electrochemical Raman studies on single-walled carbon nanotubes, I made a number of observations that contribute to a better understanding of the Raman response of carbon nanotube samples in different environments. Firstly, I showed that the Fermi energy is shifted away from its intrinsic value in solution and shifts towards the intrinsic value when the tubes are deposited on an Si/SiO_2 substrate. These Fermi energy shifts influence the LO phonon Raman peak of metallic nanotubes, which is upshifted and narrowed in solution compared to on Si/SiO_2.

I also showed that it is possible to reproduce the differences between the spectra in solution and on the substrate by deliberately changing the Fermi energy

by applying an electrochemical gate voltage. Furthermore, by monitoring the width of the metallic LO peak as a function of gate voltage, I calibrated the gate voltage to the Fermi energy and can thus determine the Fermi energy in solution (−0.16 eV) and on silicon(−0.07 eV).

These results have an application in the use of Raman spectroscopy to quantify the fraction of metallic tubes in an unknown sample, because the lineshape of metallic nanotubes with a shifted Fermi energy can resemble that of semiconducting tubes. This can be avoided by measuring spectra on silicon, where the Fermi energy is closer to the intrinsic value, and by generally noting the possibility of a Fermi energy difference between nanotubes in solution and on a substrate. I carried out the measurements described above for four samples in total and observed qualitatively similar behavior in all of them, which leads me to conclude that the Fermi energy of nanotubes in solution is commonly shifted away from its intrinsic value.

Lastly, I presented an investigation into the electrochemical Raman response of carbon nanotube energy transfer complexes formed with three different dye molecules. The dye molecules that are in proximity to the nanotubes change the charging behavior of the tubes: I observe a voltage position of the charge neutrality point and smaller maximum doping level as compared to a reference sample. These results indicate that charge transfer alone is not responsible for the differences in photoluminescence enhancement or quenching which has previously been observed in these samples.

Acknowledgments

This thesis would have been impossible without the support of a lot of people:

Thanks to Prof. Reich for the opportunity to work in her group and her invaluable ideas and helpful suggestions. Thank you to Julio, with whom the graphene experiments in this thesis were performed, especially for his expertise concerning vacuum tech and graphite intercalation compounds, and to Sebastian for providing graphene samples. The experiments with the tunable lasers would have been impossible without the help of Patryk, Sören, and Georgy. Thanks guys!

I am grateful to Astrid Gotthard at Fraunhofer Institut for giving us access to her setup for UV Raman measurements and conducting measurements with us.

Thank you to the rest of AG Reich for the nice working environment and fun chats, especially Mareen and Antonio and former members Izabella, Kika, and André.

Thank you to my parents and to Minna for their continued support, encouragement and confidence in me.

Bibliography

[1] S. Pisana, M. Lazzeri, C. Casiraghi, K. S. Novoselov, A. K. Geim, A. C. Ferrari, and F. Mauri. Breakdown of the adiabatic Born-Oppenheimer approximation in graphene. *Nature Materials*, 6(3):198–201, March 2007.

[2] A. Das, S. Pisana, B. Chakraborty, S. Piscanec, S. K. Saha, U. V. Waghmare, K. S. Novoselov, H. R. Krishnamurthy, A. K. Geim, A. C. Ferrari, and A. K. Sood. Monitoring dopants by Raman scattering in an electrochemically top-gated graphene transistor. *Nature Nanotechnology*, 3(4):210–215, April 2008.

[3] M. Kalbac, A. Reina-Cecco, H. Farhat, J. Kong, L. Kavan, and M. S. Dresselhaus. The influence of strong electron and hole doping on the Raman intensity of chemical vapor-deposition graphene. *ACS Nano*, 4(10):6055–6063, October 2010.

[4] C.-F. Chen, C.-H. Park, B. W. Boudouris, J. Horng, B. Geng, C. Girit, A. Zettl, M. F. Crommie, R. A. Segalman, S. G. Louie, and F. Wang. Controlling inelastic light scattering quantum pathways in graphene. *Nature*, 471(7340):617–620, March 2011.

[5] A. M. Rao, P. C. Eklund, S. Bandow, A. Thess, and R. E. Smalley. Evidence for charge transfer in doped carbon nanotube bundles from Raman scattering. *Nature*, 388(6639):257–259, July 1997.

[6] C. A. Howard, M. P. M. Dean, and F. Withers. Phonons in potassium-doped graphene: The effects of electron-phonon interactions, dimensionality, and adatom ordering. *Phys. Rev. B*, 84:241404, December 2011.

[7] R. Parret, M. Paillet, J.-R. Huntzinger, D. Nakabayashi, T. Michel, A. Tiberj, J.-L. Sauvajol, and A. A. Zahab. In situ Raman probing of graphene over a broad doping range upon rubidium vapor exposure. *ACS Nano*, 7(1):165–173, January 2013.

[8] T. E. Weller, M. Ellerby, S. S. Saxena, R. P. Smith, and N. T. Skipper. Superconductivity in the intercalated graphite compounds C_6Yb and C_6Ca. *Nature Physics*, 1(1):39–41, October 2005.

[9] G. Profeta, M. Calandra, and F. Mauri. Phonon-mediated superconductivity in graphene by lithium deposition. *Nature Physics*, 8(2):131–134, February 2012.

[10] K. S. Novoselov, A. K. Geim, S. V. Morozov, D. Jiang, Y. Zhang, S. V. Dubonos, I. V. Grigorieva, and A. A. Firsov. Electric field effect in atomically thin carbon films. *Science*, 306(5696):666–669, October 2004.

[11] C. Lee, X. Wei, J. W. Kysar, and J. Hone. Measurement of the elastic properties and intrinsic strength of monolayer graphene. *Science*, 321(5887):385–388, July 2008.

[12] K. Bolotin, K. Sikes, Z. Jiang, M. Klima, G. Fudenberg, J. Hone, P. Kim, and H. Stormer. Ultrahigh electron mobility in suspended graphene. *Solid State Communications*, 146(9-10):351–355, June 2008.

[13] C. R. Dean, A. F. Young, I. Meric, C. Lee, L. Wang, S. Sorgenfrei, K. Watanabe, T. Taniguchi, P. Kim, K. L. Shepard, and J. Hone. Boron nitride substrates for high-quality graphene electronics. *Nature Nanotechnology*, 5(10):722–726, October 2010.

[14] L. Wang, I. Meric, P. Y. Huang, Q. Gao, Y. Gao, H. Tran, T. Taniguchi, K. Watanabe, L. M. Campos, D. A. Muller, J. Guo, P. Kim, J. Hone, K. L. Shepard, and C. R. Dean. One-dimensional electrical contact to a two-dimensional material. *Science*, 342(6158):614–617, November 2013.

[15] J. Chen, M. Badioli, P. Alonso-Gonzalez, S. Thongrattanasiri, F. Huth, J. Osmond, M. Spasenovic, A. Centeno, A. Pesquera, P. Godignon, A. Zurutuza Elorza, N. Camara, F. J. G. de Abajo, R. Hillenbrand, and F. H. L. Koppens. Optical nano-imaging of gate-tunable graphene plasmons. *Nature*, 487(7405):77–81, July 2012.

[16] A. C. Ferrari, J. C. Meyer, V. Scardaci, C. Casiraghi, M. Lazzeri, F. Mauri, S. Piscanec, D. Jiang, K. S. Novoselov, S. Roth, and A. K. Geim. Raman spectrum of graphene and graphene layers. *Phys. Rev. Lett.*, 97(18):187401, October 2006.

[17] O. Frank, G. Tsoukleri, J. Parthenios, K. Papagelis, I. Riaz, R. Jalil, K. S. Novoselov, and C. Galiotis. Compression behavior of single-layer graphenes. *ACS Nano*, 4(6):3131–3138, June 2010.

[18] O. Frank, M. Mohr, J. Maultzsch, C. Thomsen, I. Riaz, R. Jalil, K. S. Novoselov, G. Tsoukleri, J. Parthenios, K. Papagelis, L. Kavan, and C. Galiotis. Raman 2D-band splitting in graphene: Theory and experiment. *ACS Nano*, 5(3):2231–2239, March 2011.

[19] S. Iijima and T. Ichihashi. Single-shell carbon nanotubes of 1 nm diameter. *Nature*, 363(6430):603–605, June 1993.

[20] H. Telg, J. Maultzsch, S. Reich, F. Hennrich, and C. Thomsen. Chirality distribution and transition energies of carbon nanotubes. *Physical Review Letters*, 93 (17):177401, October 2004.

[21] M. Fouquet, H. Telg, J. Maultzsch, Y. Wu, B. Chandra, J. Hone, T. F. Heinz, and C. Thomsen. Longitudinal optical phonons in metallic and semiconducting carbon nanotubes. *Physical Review Letters*, 102(7):075501, February 2009.

[22] M. S. Dresselhaus, A. Jorio, A. G. Souza Filho, and R. Saito. Defect characterization in graphene and carbon nanotubes using Raman spectroscopy. *Phil. Trans. R. Soc. A*, 368(1932):5355–77, December 2010.

[23] D. K. Efetov and P. Kim. Controlling electron-phonon interactions in graphene at ultrahigh carrier densities. *Phys. Rev. Lett.*, 105:256805, December 2010.

[24] M. S. Dresselhaus and G. Dresselhaus. Intercalation compounds of graphite. *Advances in Physics*, 51(1):1–186, January 2002.

[25] J. C. Chacon-Torres, L. Wirtz, and T. Pichler. Manifestation of charged and strained graphene layers in the Raman response of graphite intercalation compounds. *ACS Nano*, 7(10):9249–9259, October 2013.

[26] A. Grueneis, C. Attaccalite, A. Rubio, D. V. Vyalikh, S. L. Molodtsov, J. Fink, R. Follath, W. Eberhardt, B. Buechner, and T. Pichler. Angle-resolved photoemission study of the graphite intercalation compound KC_8: A key to graphene. *Phys. Rev. B*, 80(7):075431, August 2009.

[27] A. V. Fedorov, N. I. Verbitskiy, D. Haberer, C. Struzzi, L. Petaccia, D. Usachov, O. Y. Vilkov, D. V. Vyalikh, J. Fink, M. Knupfer, B. Buechner, and A. Grueneis. Observation of a universal donor-dependent vibrational mode in graphene. *Nature Communications*, 5:3257, February 2014.

[28] F. Ernst, T. Heek, A. Setaro, R. Haag, and S. Reich. Energy transfer in nanotube-perylene complexes. *Adv. Funct. Mater.*, 22(18):3921–3926, September 2012.

[29] F. Ernst, S. Heeg, T. Heek, A. Setaro, R. Haag, and S. Reich. Selective interaction between nanotubes and perylene-based surfactant. *physica status solidi (RRL) Rapid Research Letters*, 7(8):546–549, 2013.

[30] F. Ernst, T. Heek, A. Setaro, R. Haag, and S. Reich. Excitation characteristics of different energy transfer in nanotube-perylene complexes. *Appl. Phys. Lett.*, 102 (23):233105, 2013.

[31] C. Roquelet, J.-S. Lauret, V. Alain-Rizzo, C. Voisin, R. Fleurier, M. Delarue, D. Garrot, A. Loiseau, P. Roussignol, J. A. Delaire, and E. Deleporte. Pi -stacking functionalization of carbon nanotubes through micelle swelling. *ChemPhysChem*, 11(8):1667–1672, 2010.

[32] C. Roquelet, D. Garrot, J. S. Lauret, C. Voisin, V. Alain-Rizzo, P. Roussignol, J. A. Delaire, and E. Deleporte. Quantum efficiency of energy transfer in noncovalent carbon nanotube/porphyrin compounds. *Appl. Phys. Lett.*, 97(14):141918, 2010.

[33] F. Vialla, C. Roquelet, B. Langlois, G. Delport, S. M. Santos, E. Deleporte, P. Roussignol, C. Delalande, C. Voisin, and J.-S. Lauret. Chirality dependence of the absorption cross section of carbon nanotubes. *Phys. Rev. Lett.*, 111(13): 137402, September 2013.

[34] A. K. Geim and K. S. Novoselov. The rise of graphene. *Nature Materials*, 6(3): 183–191, March 2007.

[35] A. H. Castro Neto, F. Guinea, N. M. R. Peres, K. S. Novoselov, and A. K. Geim. The electronic properties of graphene. *Rev. Mod. Phys.*, 81(1):109–162, January 2009.

[36] Y. Zhang, Y.-W. Tan, H. L. Stormer, and P. Kim. Experimental observation of the quantum Hall effect and Berry's phase in graphene. *Nature*, 438(7065): 201–204, November 2005.

[37] K. S. Novoselov, Z. Jiang, Y. Zhang, S. V. Morozov, H. L. Stormer, U. Zeitler, J. C. Maan, G. S. Boebinger, P. Kim, and A. K. Geim. Room-temperature quantum Hall effect in graphene. *Science*, 315(5817):1379, March 2007.

[38] A. Woessner, M. B. Lundeberg, Y. Gao, A. Principi, P. Alonso-Gonzalez, M. Carrega, K. Watanabe, T. Taniguchi, G. Vignale, M. Polini, J. Hone, R. Hillenbrand, and F. H. L. Koppens. Highly confined low-loss plasmons in graphene-boron nitride heterostructures. *Nature Materials*, 14(4):421–425, April 2015.

[39] K. S. Novoselov, D. Jiang, F. Schedin, T. J. Booth, V. V. Khotkevich, S. V. Morozov, and A. K. Geim. Two-dimensional atomic crystals. *Proceedings of the National Academy of Sciences of the United States of America*, 102(30):10451–10453, July 2005.

[40] K. S. Novoselov, A. K. Geim, S. V. Morozov, D. Jiang, M. I. Katsnelson, I. V. Grigorieva, S. V. Dubonos, and A. A. Firsov. Two-dimensional gas of massless Dirac fermions in graphene. *Nature*, 438(7065):197–200, November 2005.

[41] K. F. Mak, M. Y. Sfeir, Y. Wu, C. H. Lui, J. A. Misewich, and T. F. Heinz. Measurement of the optical conductivity of graphene. *Phys. Rev. Lett.*, 101:196405, Nov 2008.

[42] R. R. Nair, P. Blake, A. N. Grigorenko, K. S. Novoselov, T. J. Booth, T. Stauber, N. M. R. Peres, and A. K. Geim. Fine structure constant defines visual transparency of graphene. *Science*, 320(5881):1308–1308, June 2008.

[43] J. W. Weber, V. E. Calado, and M. C. M. van de Sanden. Optical constants of graphene measured by spectroscopic ellipsometry. *Appl. Phys. Lett.*, 97(9):091904, August 2010.

[44] Z. H. Ni, H. M. Wang, J. Kasim, H. M. Fan, T. Yu, Y. H. Wu, Y. P. Feng, and Z. X. Shen. Graphene thickness determination using reflection and contrast spectroscopy. *Nano Lett.*, 7(9):2758–2763, September 2007.

[45] C. Thomsen and S. Reich. Raman scattering in carbon nanotubes. In M. Cardona and R. Merlin, editors, *Light Scattering in Solids IX: Novel Materials and Techniques*, volume 108 of *Topics in Applied Physics*, pages 115–235. Springer-Verlag, Berlin Heidelberg New York, 2007.

[46] A. C. Ferrari and D. M. Basko. Raman spectroscopy as a versatile tool for studying

the properties of graphene. *Nature Nanotechnology*, 8(4):235–246, April 2013.

[47] J. Maultzsch, S. Reich, C. Thomsen, H. Requardt, and P. Ordejon. Phonon dispersion in graphite. *Phys. Rev. Lett.*, 92(7):075501, February 2004.

[48] C. Thomsen and S. Reich. Double resonant Raman scattering in graphite. *Phys. Rev. Lett.*, 85(24):5214–5217, December 2000.

[49] D. M. Basko. Theory of resonant multiphonon Raman scattering in graphene. *Phys. Rev. B*, 78(12):125418, September 2008.

[50] W. Kohn. Image of the Fermi surface in the vibration spectrum of a metal. *Phys. Rev. Lett.*, 2(9):393–394, May 1959.

[51] M. Lazzeri, S. Piscanec, F. Mauri, A. C. Ferrari, and J. Robertson. Phonon linewidths and electron-phonon coupling in graphite and nanotubes. *Phys. Rev. B*, 73(15):155426, April 2006.

[52] F. Cerdeira, T. A. Fjeldly, and M. Cardona. Effect of free carriers on zone-center vibrational modes in heavily doped p-type Si. II. Optical modes. *Phys. Rev. B*, 8 (10):4734–4745, November 1973.

[53] U. Fano. Effects of configuration interaction on intensities and phase shifts. *Physical Review*, 124(6):1866–1878, December 1961.

[54] P. C. Eklund, G. Dresselhaus, M. S. Dresselhaus, and J. E. Fischer. Raman scattering from in-plane lattice modes in low-stage graphite-alkali-metal compounds. *Phys. Rev. B*, 16(8):3330–3333, October 1977.

[55] R. J. Nemanich, S. A. Solin, and D. Gűerard. Raman scattering from intercalated donor compounds of graphite. *Phys. Rev. B*, 16(6):2965–2972, September 1977.

[56] S. A. Solin and N. Caswell. Raman scattering from alkali graphite intercalation compounds. *J. Raman Spectrosc.*, 10(1):129–135, January 1981.

[57] P. C. Eklund and K. R. Subbaswamy. Analysis of Breit-Wigner line shapes in the Raman spectra of graphite intercalation compounds. *Phys. Rev. B*, 20(12): 5157–5161, December 1979.

[58] J. Hlinka, I. Gregora, J. Pokorny, C. Herold, N. Emery, J. F. Mareche, and P. Lagrange. Lattice dynamics of CaC_6 by Raman spectroscopy. *Phys. Rev. B*, 76(14): 144512, October 2007.

[59] A. Mialitsin, J. S. Kim, R. K. Kremer, and G. Blumberg. Raman scattering from the CaC_6 superconductor in the presence of disorder. *Phys. Rev. B*, 79(6):064503, February 2009.

[60] M. P. M. Dean, C. A. Howard, S. S. Saxena, and M. Ellerby. Nonadiabatic

phonons within the doped graphene layers of XC_6 compounds. *Phys. Rev. B*, 81 (4):045405, January 2010.

[61] J. C. Chacon-Torres, L. Wirtz, and T. Pichler. Raman spectroscopy of graphite intercalation compounds: Charge transfer, strain, and electron-phonon coupling in graphene layers. *Phys. Status Solidi B*, 251(12):2337–2355, December 2014.

[62] J. C. Chacon-Torres, A. Y. Ganin, M. J. Rosseinsky, and T. Pichler. Raman response of stage-1 graphite intercalation compounds revisited. *Phys. Rev. B*, 86 (7):075406, August 2012.

[63] A. M. Saitta, M. Lazzeri, M. Calandra, and F. Mauri. Giant nonadiabatic effects in layer metals: Raman spectra of intercalated graphite explained. *Phys. Rev. Lett.*, 100(22):226401, June 2008.

[64] B. Hatting. Raman scattering in single-walled carbon nanotubes in solution and on substrates. Master's thesis, Freie Universität Berlin, 2011.

[65] M. Lazzeri, C. Attaccalite, L. Wirtz, and F. Mauri. Impact of the electron-electron correlation on phonon dispersion: Failure of LDA and GGA DFT functionals in graphene and graphite. *Phys. Rev. B*, 78(8):081406, August 2008.

[66] W. Zhao, P. H. Tan, J. Liu, and A. C. Ferrari. Intercalation of few-layer graphite flakes with $FeCl_3$: Raman determination of Fermi level, layer by layer decoupling, and stability. *J. Am. Chem. Soc.*, 133(15):5941–5946, April 2011.

[67] D. Tristant, Y. Wang, I. Gerber, M. Monthioux, A. Penicaud, and P. Puech. Optical signatures of bulk and solutions of KC_8 and KC_{24}. *Journal of Applied Physics*, 118(4):044304, July 2015.

[68] A. Grueneis, C. Attaccalite, A. Rubio, D. V. Vyalikh, S. L. Molodtsov, J. Fink, R. Follath, W. Eberhardt, B. Buechner, and T. Pichler. Electronic structure and electron-phonon coupling of doped graphene layers in KC_8. *Phys. Rev. B*, 79(20): 205106, May 2009.

[69] S. Iijima. Helical microtubules of graphitic carbon. *Nature*, 354(6348):56–58, November 1991.

[70] S. Reich, C. Thomsen, and J. Maultzsch. *Carbon Nanotubes: Basic Concepts and Physical Properties*. Wiley-VCH, 2004.

[71] J. C. Charlier, X. Blase, and S. Roche. Electronic and transport properties of nanotubes. *Reviews of Modern Physics*, 79(2):677–732, April 2007.

[72] R. Saito, M. Fujita, G. Dresselhaus, and M. S. Dresselhaus. Electronic-structure of graphene tubules based on C_{60}. *Phys. Rev. B*, 46(3):1804–1811, July 1992.

[73] T. Ando. The electronic properties of graphene and carbon nanotubes. *NPG Asia*

Materials, 1:17–21, October 2009.

[74] J. Maultzsch, H. Telg, S. Reich, and C. Thomsen. Radial breathing mode of single-walled carbon nanotubes: Optical transition energies and chiral-index assignment. *Phys. Rev. B*, 72(20):205438, November 2005.

[75] S. Piscanec, M. Lazzeri, J. Robertson, A. C. Ferrari, and F. Mauri. Optical phonons in carbon nanotubes: Kohn anomalies, Peierls distortions, and dynamic effects. *Phys. Rev. B*, 75(3):035427, January 2007.

[76] C. Blum, N. Stuerzl, F. Hennrich, S. Lebedkin, S. Heeg, H. Dumlich, S. Reich, and M. M. Kappes. Selective bundling of zigzag single-walled carbon nanotubes. *ACS Nano*, 5(4):2847–2854, April 2011.

[77] B. Hatting, S. Heeg, K. Ataka, J. Heberle, F. Hennrich, M. M. Kappes, R. Krupke, and S. Reich. Fermi energy shift in deposited metallic nanotubes: A Raman scattering study. *Phys. Rev. B*, 87(16):165442, April 2013.

[78] B. Hatting, S. Heeg, and S. Reich. Raman spectra of metallic carbon nanotubes in solution and on substrates. *Phys. Status Solidi B*, 250(12):2639–2642, December 2013.

[79] B. Hatting, F. Ernst, and S. Reich. Electrochemical Raman spectroscopy of carbon nanotube energy transfer complexes. *Phys. Status Solidi B*, 251(12):2491–2494, December 2014.

[80] D. Chattopadhyay, I. Galeska, and F. Papadimitrakopoulos. A route for bulk separation of semiconducting from metallic single-wall carbon nanotubes. *J. Am. Chem. Soc.*, 125(11):3370–3375, February 2003.

[81] Y. Maeda, S.-i. Kimura, M. Kanda, Y. Hirashima, T. Hasegawa, T. Wakahara, Y. Lian, T. Nakahodo, T. Tsuchiya, T. Akasaka, J. Lu, X. Zhang, Y. Yu, S. Nagase, S. Kazaoui, N. Minami, T. Shimizu, H. Tokumoto, and R. Saito. Large-scale separation of metallic and semiconducting single-walled carbon nanotubes. *J. Am. Chem. Soc.*, 127(29):10287–10290, July 2005.

[82] H. Li, B. Zhou, Y. Lin, L. Gu, W. Wang, K. A. S. Fernando, S. Kumar, L. F. Allard, and Y.-P. Sun. Selective interactions of porphyrins with semiconducting single-walled carbon nanotubes. *J. Am. Chem. Soc.*, 126(4):1014–1015, January 2004.

[83] K. Ishikawa and T. Ando. Optical phonon interacting with electrons in carbon nanotubes. *Journal of the Physical Society of Japan*, 75(8):084713, August 2006.

[84] N. Caudal, A. M. Saitta, M. Lazzeri, and F. Mauri. Kohn anomalies and nonadiabaticity in doped carbon nanotubes. *Phys. Rev. B*, 75(11):115423, March 2007.

[85] J. C. Tsang, M. Freitag, V. Perebeinos, J. Liu, and P. Avouris. Doping and

phonon renormalization in carbon nanotubes. *Nature Nanotechnology*, 2(11):725–730, November 2007.

[86] E. H. Haroz, J. G. Duque, W. D. Rice, C. G. Densmore, J. Kono, and S. K. Doorn. Resonant Raman spectroscopy of armchair carbon nanotubes: Absence of broad G(-) feature. *Phys. Rev. B*, 84(12):121403, September 2011.

[87] M. Paillet, T. Michel, A. Zahab, D. Nakabayashi, V. Jourdain, R. Parret, J. Meyer, and J. L. Sauvajol. Probing the structure of single-walled carbon nanotubes by resonant Raman scattering. *Phys. Status Solidi B*, 247(11-12):2762–2767, December 2010.

[88] K. I. Sasaki, R. Saito, G. Dresselhaus, M. S. Dresselhaus, H. Farhat, and J. Kong. Curvature-induced optical phonon frequency shift in metallic carbon nanotubes. *Phys. Rev. B*, 77(24):245441, June 2008.

[89] J. S. Park, K. Sasaki, R. Saito, W. Izumida, M. Kalbac, H. Farhat, G. Dresselhaus, and M. S. Dresselhaus. Fermi energy dependence of the G-band resonance Raman spectra of single-wall carbon nanotubes. *Phys. Rev. B*, 80(8):081402, August 2009.

[90] S. Piscanec, M. Lazzeri, F. Mauri, A. C. Ferrari, and J. Robertson. Kohn anomalies and electron-phonon interactions in graphite. *Phys. Rev. Lett.*, 93(18):185503, October 2004.

[91] O. Dubay, G. Kresse, and H. Kuzmany. Phonon softening in metallic nanotubes by a Peierls-like mechanism. *Phys. Rev. Lett.*, 88(23):235506, June 2002.

[92] T. Ando. Anomaly of optical phonon in monolayer graphene. *Journal of the Physical Society of Japan*, 75(12):124701, November 2006.

[93] Y. Wu, J. Maultzsch, E. Knoesel, B. Chandra, M. Y. Huang, M. Y. Sfeir, L. E. Brus, J. Hone, and T. F. Heinz. Variable electron-phonon coupling in isolated metallic carbon nanotubes observed by Raman scattering. *Phys. Rev. Lett.*, 99 (2):027402, July 2007.

[94] M. V. Klein. Electronic Raman scattering. In M. Cardona, editor, *Light Scattering in Solids I: Introductory Concepts*, volume 8 of *Topics in Applied Physics*, page 147. Springer-Verlag, Berlin Heidelberg New York, 1983.

[95] K. T. Nguyen, A. Gaur, and M. Shim. Fano lineshape and phonon softening in single isolated metallic carbon nanotubes. *Phys. Rev. Lett.*, 98(14):145504, April 2007.

[96] M. Kalbac, L. Kavan, L. Dunsch, and M. S. Dresselhaus. Development of the tangential mode in the Raman spectra of swcnt bundles during electrochemical charging. *Nano Lett.*, 8(4):1257–1264, March 2008.

[97] T. Ando. Optical phonon tuned by Fermi level in carbon nanotubes. *Journal of*

the Physical Society of Japan, 77(1):014707, December 2008.

[98] S. B. Cronin, R. Barnett, M. Tinkham, S. G. Chou, O. Rabin, M. S. Dresselhaus, A. K. Swan, M. S. Unlu, and B. B. Goldberg. Electrochemical gating of individual single-wall carbon nanotubes observed by electron transport measurements and resonant Raman spectroscopy. *Appl. Phys. Lett.*, 84(12):2052–2054, March 2004.

[99] P. M. Rafailov, J. Maultzsch, C. Thomsen, and H. Kataura. Electrochemical switching of the Peierls-like transition in metallic single-walled carbon nanotubes. *Phys. Rev. B*, 72(4):045411, July 2005.

[100] M. S. Strano, C. B. Huffman, V. C. Moore, M. J. O'Connell, E. H. Haroz, J. Hubbard, M. Miller, K. Rialon, C. Kittrell, S. Ramesh, R. H. Hauge, and R. E. Smalley. Reversible, band-gap-selective protonation of single-walled carbon nanotubes in solution. *J. Phys. Chem. B*, 107(29):6979–6985, June 2003.

[101] V. Derycke, R. Martel, J. Appenzeller, and P. Avouris. Controlling doping and carrier injection in carbon nanotube transistors. *Appl. Phys. Lett.*, 80(15):2773–2775, April 2002.

[102] S.-H. Hur, M.-H. Yoon, A. Gaur, M. Shim, A. Facchetti, T. J. Marks, and J. A. Rogers. Organic nanodielectrics for low voltage carbon nanotube thin film transistors and complementary logic gates. *J. Am. Chem. Soc.*, 127(40):13808–13809, September 2005.

[103] C. M. Aguirre, P. L. Levesque, M. Paillet, F. Lapointe, B. C. St-Antoine, P. Desjardins, and R. Martel. The role of the oxygen/water redox couple in suppressing electron conduction in field-effect transistors. *Advanced Materials*, 21(30):3087, August 2009.

[104] P. L. Levesque, S. S. Sabri, C. M. Aguirre, J. Guillemette, M. Siaj, P. Desjardins, T. Szkopek, and R. Martel. Probing charge transfer at surfaces using graphene transistors. *Nano Lett.*, 11(1):132–137, December 2010.

[105] A. Gaur and M. Shim. Substrate-enhanced O_2 adsorption and complexity in the Raman G-band spectra of individual metallic carbon nanotubes. *Phys. Rev. B*, 78(12):125422, September 2008.

[106] A. D. Franklin, M. Luisier, S.-J. Han, G. Tulevski, C. M. Breslin, L. Gignac, M. S. Lundstrom, and W. Haensch. Sub-10 nm carbon nanotube transistor. *Nano Lett.*, 12(2):758–762, January 2012.

[107] A. L. Antaris, J. T. Robinson, O. K. Yaghi, G. Hong, S. Diao, R. Luong, and H. Dai. Ultra-low doses of chirality sorted (6,5) carbon nanotubes for simultaneous tumor imaging and photothermal therapy. *ACS Nano*, 7(4):3644–3652, March 2013.

[108] E. H. Hasdeo, A. R. T. Nugraha, K. Sato, M. S. Dresselhaus, and R. Saito. Ori-

gin of electronic Raman scattering and the Fano resonance in metallic carbon nanotubes. *Phys. Rev. B*, (88):115107, September 2013.

[109] H. Farhat, H. Son, G. G. Samsonidze, S. Reich, M. S. Dresselhaus, and J. Kong. Phonon softening in individual metallic carbon nanotubes due to the Kohn anomaly. *Phys. Rev. Lett.*, 99(14):145506, October 2007.

[110] P. M. Rafailov, J. Maultzsch, C. Thomsen, U. Dettlaff-Weglikowska, and S. Roth. Kohn anomaly and electron-phonon interaction at the K-derived point of the Brillouin zone of metallic nanotubes. *Nano Lett.*, 9(9):3343–3348, September 2009.

[111] J. G. Duque, H. Chen, A. K. Swan, A. P. Shreve, S. Kilina, S. Tretiak, X. Tu, M. Zheng, and S. K. Doorn. Violation of the Condon approximation in semiconducting carbon nanotubes. *ACS Nano*, 5(6):5233–5241, May 2011.

[112] F. Dragin, A. Penicaud, M. Iurlo, M. Marcaccio, F. Paolucci, E. Anglaret, and R. Martel. Raman doping profiles of polyelectrolyte swnts in solution. *ACS Nano*, 5(12):9892–9897, November 2011.

[113] M. Steiner, M. Freitag, V. Perebeinos, A. Naumov, J. P. Small, A. A. Bol, and P. Avouris. Gate-variable light absorption and emission in a semiconducting carbon nanotube. *Nano Lett.*, 9(10):3477–3481, July 2009.

[114] T. Koyama, Y. Miyata, H. Kishida, H. Shinohara, and A. Nakamura. Photophysics in single-walled carbon nanotubes with (6,4) chirality at high excitation densities: Bimolecular auger recombination and phase-space filling of excitons. *J. Phys. Chem. C*, 117(4):1974–1981, January 2013.

[115] K. Liu, J. Deslippe, F. Xiao, R. B. Capaz, X. Hong, S. Aloni, A. Zettl, W. Wang, X. Bai, S. G. Louie, E. Wang, and F. Wang. An atlas of carbon nanotube optical transitions. *Nature Nanotechnology*, 7(5):325–329, May 2012.

[116] H. Park, A. Afzali, S. J. Han, G. S. Tulevski, A. D. Franklin, J. Tersoff, J. B. Hannon, and W. Haensch. High-density integration of carbon nanotubes via chemical self-assembly. *Nature Nanotechnology*, 7(12):787–791, December 2012.

[117] N. W. S. Kam, M. O'Connell, J. A. Wisdom, and H. Dai. Carbon nanotubes as multifunctional biological transporters and near-infrared agents for selective cancer cell destruction. *Proceedings of the National Academy of Sciences of the United States of America*, 102(33):11600–11605, August 2005.

[118] D. Paolucci, M. M. Franco, M. Iurlo, M. Marcaccio, M. Prato, F. Zerbetto, A. Pénicaud, and F. Paolucci. Singling out the electrochemistry of individual single-walled carbon nanotubes in solution. *J. Am. Chem. Soc.*, 130(23):7393–7399, May 2008.

[119] P. G. Collins, M. S. Arnold, and P. Avouris. Engineering carbon nanotubes and

nanotube circuits using electrical breakdown. *Science*, 292(5517):706–709, April 2001.

[120] R. Krupke, F. Hennrich, H. von Lohneysen, and M. M. Kappes. Separation of metallic from semiconducting single-walled carbon nanotubes. *Science*, 301(5631): 344–347, July 2003.

Erklärung

Hiermit erkläre ich, dass ich die vorliegende Arbeit selbstständig verfasst und keine anderen als die angegebenen Quellen und Hilfsmittel benutzt habe. Die Arbeit ist nicht schon einmal in einem früheren Promotionsverfahren angenommen oder als ungenügend beurteilt worden.

List of Publications

B. Hatting, F. Ernst, and S. Reich. Electrochemical Raman spectroscopy of carbon nanotube energy transfer complexes. *Phys. Status Solidi B*, 251(12):2491–2494, December 2014.

B. Hatting, S. Heeg, K. Ataka, J. Heberle, F. Hennrich, M. M. Kappes, R. Krupke, and S. Reich. Fermi energy shift in deposited metallic nanotubes: A Raman scattering study. *Phys. Rev. B*, 87(16):165442, April 2013.

B. Hatting, S. Heeg, and S. Reich. Raman spectra of metallic carbon nanotubes in solution and on substrates. *Phys. Status Solidi B*, 250(12):2639–2642, December 2013.